Imperial College London
Department of Mechanical Engineering

Radiographic Imaging of Subsea Pipelines

by

Misty Isanna Haith

A thesis submitted to Imperial College London for the degree of
Engineering Doctorate

Department of Mechanical Engineering
Imperial College London
London SW7 2AZ

September 2016

Declaration

I herewith certify that all material in this dissertation which is not my own work has been properly acknowledged.

Misty Isanna Haith

Copyright Statement

Abstract

Subsea pipelines are increasingly being used both around offshore drilling facilities and for long distance oil and gas transport. Accidents can have devastating environmental and economic impact, amplifying the need for accurate, reliable detection and characterisation of pipeline defects. Inspection of these pipelines for corrosion and other defects is crucial for safe operation. Radiography holds a significant advantage over many other inspection methods in that it does not require surface preparation or insulation removal.

Subsea pipeline radiography is a relatively new technique, and underwater conditions are not covered by radiographic standards. Water can have a significant impact on a radiographic image and access is very difficult, meaning standardised above-water methods may not be applicable. This is particularly the case for defect characterisation; standard methods often call for calibration objects to be included in the setup, which can be a very complex operation in subsea conditions. There is also a lack of experimental data for research, due to the difficulty and high costs associated with subsea radiography. Simulation is one of the key ways of assessing inspection problems, however radiographic simulation models have not been validated for subsea inspections.

This thesis addresses the two problems of accurate subsea simulation and alternative defect characterisation methods. Firstly the accuracy of a radiographic simulation model applied to subsea pipeline inspections is investigated. Experimental measurements of a sample in a water tank are used to adjust the simulation, with the aim of matching image quality parameters - such as signal-to-noise ratio and contrast. The simulation has been partially matched to experiment, with some differences found in contrast-to-noise ratio. Possible causes of the differences are analysed, with the most likely cause found to be detector backscatter and additional scatter from out-of-setup objects within the experimental exposure bay.

The simulation model is then used to provide data for development and testing of a defect characterisation method. The method relies on knowledge of the setup geometry and use of multiple images, and does not require calibration objects to be included in the setup. It is specifically aimed at use in situations where access is difficult such as in subsea pipeline inspections. The method is tested on simulated and experimental flat bottomed hole defects and simulated corrosion patch defects. Results demonstrate a good, consistent ability to calculate lateral and axial defect dimensions. Defect thickness calculations are more difficult and as such errors are more significant. However, errors in thickness are due to overestimation, meaning the calculation could be used to place a maximum limit on potential defect size rather than as an actual estimate of the thickness.

Acknowledgements

Firstly I would like to thank my academic supervisors Mike Lowe and Peter Huthwaite for their guidance and support throughout my project. Thanks also to my industrial supervisors Tom Knox and Ian Bradley, as well as Robin Jones, for their help and advice.

I would like to acknowledge the support of BP, the UK Research Centre in Non-Destructive Testing (RCNDE), the Engineering and Physical Sciences Research Council (EPSRC) and the Royal Commission for the Exhibition of 1851. I also extend thanks to the Federal Institute of Materials Testing (BAM), Berlin, for their collaboration and for hosting me during a research placement. I am grateful to the NDT group at Imperial College London for the friendly and open atmosphere, making it a great place to work for the last four years. Thanks to Glenn Jones for his help and for being there when I needed someone to talk radiography to!

Finally, thanks to my family for their continued understanding and support. In particular I am grateful to my mother, who never doubted that I would get this far, and to my partner, who is always there to offer help when I need it.

Contents

List of Figures

1 Introduction

1.1 Industrial Context

Non-Destructive Evaluation (NDE) is the area of engineering concerned with inspection of industrial components, determining their structural integrity without causing damage. There are many different inspection techniques ranging from ultrasonics and radiography to eddy current methods and dye penetrant testing [1]. NDE is invaluable throughout industry in preventing failure of in-service components and improving quality control during manufacturing.

Subsea pipelines are increasingly being used both around offshore drilling facilities and for long distance oil and gas transport. Inspection of these pipelines for potential corrosion and other damage is crucial for safe operation. Accidents can have devastating environmental and economic impact, amplifying the need for accurate, reliable detection and characterisation of pipeline defects. For many pipelines internal inspection techniques can be used. Internal methods include ultrasonics, magnetic flux leakage and eddy current inspection [2]. However in some cases internal inspection is not possible, for example due to lack of access, and external inspection methods must be used.

External inspection of subsea pipelines presents unique challenges. Access is difficult, particularly in deep water areas which require remotely operated inspections and pressure resistant equipment. In addition, some subsea pipelines have thick insulation or concrete coating, which means methods requiring surface or near surface contact, eg ultrasonics and eddy current testing, are not well suited as they would require insulation removal. Radiography holds a significant advantage over many other inspection methods in that it does not require surface preparation or insulation removal. Development of modern digital detectors has further improved the prospect of radiography, as digital images can be viewed almost in real time with no

need to retrieve and scan computed radiography imaging plates or develop film. This makes radiography one of the most suitable methods for subsea pipeline inspection.

This thesis addresses the two problems of accurate subsea simulation and alternative defect characterisation methods. Firstly the accuracy of a radiographic simulation model applied to subsea pipeline inspections is investigated. Subsea pipeline radiography is a relatively new technique. Standards for radiographic imaging of pipeline corrosion [3, 4] do not currently cover underwater conditions. As water is highly scattering it can have a significant impact on radiographic image quality: thus it is vital to investigate inspection configurations with water. Subsea radiography is extremely costly, and extensive experimental data for research is difficult to obtain. Simulations are significantly more affordable and accessible than subsea experimental data, and are able to model a wide range of underwater radiographic setups. However, simulation models have not been validated as accurate for underwater imaging, and before conclusions can be drawn from simulation results they must be shown to be comparable to experimental results. Hence a major aim of the project was to investigate the ability to accurately simulate underwater radiography.

The simulation model is then used to provide data for development and testing of a defect characterisation method. Traditional methods of radiographic defect sizing rely on using additional objects of known size placed in the setup. For example, to estimate defect depth a step wedge must be included in the exposure, placed on the pipe as close as possible to the region of interest [4]. The step wedge is used in the resulting image to calibrate the relation of intensity to material thickness, allowing for defect depth to be calculated from its change in grey level. In a subsea environment, where the inspection is being controlled with a remotely operated vehicle, inclusion of objects such as a step wedge would add an additional layer of complexity to an already difficult inspection. Factors such as the positioning of the step wedge can impact the accuracy of the resulting defect characterisation, which could affect the reliability of the method. Therefore it is advantageous to develop methods of defect characterisation for double wall pipeline radiography that do not require additional objects in the setup.

1.2 Project Organisation

This project was run within the UK Research Centre for Non-Destructive Evaluation (RCNDE) as a collaboration between Imperial College London and BP. BP provided the industrial context, details of implementation and relevant radiographic data for the project. I was primarily based at Imperial College London for the project, but maintained regular contact with my supervisors in BP, who contributed to steering the project and provided feedback from an industrial viewpoint.

In 2014, the third year of the project, I was awarded an industrial fellowship from the Royal Commission for the Exhibition of 1851 [5]. The 1851 industrial fellowship is a scheme to support doctorate level research with strong industrial motivations and the potential for significant contribution to UK industry. It provides additional funding for the project in the third and fourth years. This funding significantly boosted the project by allowing a three month research placement and collaboration with the Federal Institute of Materials Testing (BAM) in Berlin [6]. BAM is an international authority on radiography, responsible for many of the official standards of practice. The collaboration extended the scope of the project by providing an experimental element and the possibility of using a simulation model developed by BAM to investigate subsea pipeline imaging. The collaboration resulted in two joint conference papers at the 2015 Quantitative Review of Progress in Non-Destructive Evaluation (QNDE) conference [7, 8], and a journal paper in NDT&E International[9].

1.3 Thesis Structure

The thesis begins in Chapter 2 with an introduction to radiographic theory. Photon interactions in matter, radiographic equipment, standards of pipeline corrosion imaging and methods of image analysis are described. Chapter 3 moves on to detail the initial project work; development of a radiographic simulation model. The aim of the model development was to provide a simple, fast alternative to commercially available models, as well as to act as a learning tool in radiographic simulation. The simulation method is described, and results are given and validated through comparison with two commercially available models.

Chapter 4 describes my investigation of the accuracy of radiographic simulation models for subsea imaging, in collaboration with BAM. Experimental measurements of a sample in a water tank are used to adjust the simulation, with the aim of matching image quality parameters - such as signal-to-noise ratio and contrast. The simulation has been partially matched to experiment, with some differences found in contrast-to-noise ratio. Possible causes of the differences are analysed, with the most likely cause found to be detector backscatter and additional scatter from out-of-setup objects within the experimental exposure bay. Chapter 4 was originally written as a journal paper and has been published in NDT&E International [9]. In addition, I have presented the work at the QNDE 2015, BINDT 2015 and WCNDT 2016 conferences, and published a conference proceedings paper [7].

Chapter 5 describes the development and testing of the pipeline defect characterisation method. The method relies on knowledge of the setup geometry and use of multiple images, and does not require calibration objects to be included in the setup. It is specifically aimed at use in situations where access is difficult such as in subsea pipeline inspections. The method is tested on simulated and experimental flat bottomed hole defects and simulated corrosion patch defects. Results demonstrate a good, consistent ability to calculate lateral and axial defect dimensions. Calculations of defect thickness are more difficult and as such errors are more significant. However, errors in thickness are due to overestimation, meaning the calculation could be used to place a maximum limit on potential defect size rather than as an actual estimate of the thickness. In this chapter, 'defect thickness' is used to refer to the maximum wall loss caused by the defect. Again this chapter was originally written as a journal paper and has been published in NDT&E International [10]. I have also presented this set of work at QNDE 2016.

Finally Chapter 6 presents the conclusions of the work. In addition possible applications are discussed, along with future work required to further the project achievements.

2 Radiographic Theory

2.1 Photon Interactions in Matter

Radiographic images are formed through the propagation of high energy radiation (x-rays or gamma rays) through an object to the detector. When photons travel through a material they have a probability of interacting with atoms in the material; they may be absorbed by the photoelectric effect, scattered through Compton or Rayleigh scattering or undergo pair production [1, 11]. Those photons remaining will reach the detector and have a chance of detection to form the image.

The probability of a photon interacting in a material is dependent on the photon's energy but also highly dependent on the density and atomic structure of the material. The attenuation coefficient of a material is directly proportional to the probability of photon interaction; Figure 2.1 shows the mass attenuation of water, iron and lead for a range of photon energies. Mass attenuation is attenuation normalised by the material density; it allows multiple materials to be compared without the disparity in magnitudes caused by density. It is this disparity that forms the image. Photons will be less attenuated if travelling through a low density, rather than high density, material. Consequently, more radiation will be detected from low density regions of an object.

The intensity of direct, unscattered radiation reaching the detector, I, can be calculated from the material attenuation using the Beer-Lambert Law:

$$I(E) = I_0(E)e^{-\mu(E)x} \tag{2.1}$$

where E is the energy of the photons, I_0 is the initial radiation intensity, μ is the attenuation of the material and x is the distance travelled through the material.

This equation does not take into account photons which are detected af-

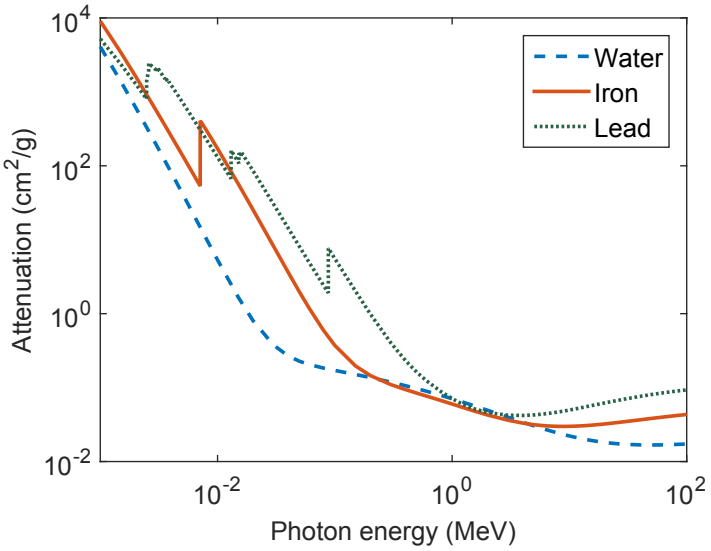

Figure 2.1: Mass attenuation, μ/ρ, for photons travelling through water, iron and lead where μ is the total attenuation coefficient and ρ is the material density. Sharp peaks occur when the photon energy is just high enough for the photons to interact with an additional electron shell. The attenuation data was obtained from the XCOM online database [12].

ter being scattered; for thin or low density materials, this is often sufficient. However, for thicker or denser materials, such as the steel pipes and water being examined in this project, scattered photons can have a significant impact on the results through lowering the contrast. It is difficult to analytically calculate the impact of scattering; photon interactions in matter are stochastic and are generally dealt with through probabilistic Monte Carlo simulation. Deterministic scattering models have been developed [13, 14, 15] but tend to be limited in application, for example only calculating first-order scattering.

The attenuation coefficient of a material can be split into separate components giving the attenuation coefficient for each type of interaction, which is directly proportional to its probability. The relative probability of each interaction varies with material type and photon energy. For example Rayleigh scattering is more probable at low photon energies, and is never a very strong effect relative to other interactions. Rayleigh scattering occurs when the electromagnetic field of a photon interacts with bound atomic

electrons. The electromagnetic field causes the electrons to oscillate at the same frequency. This acts as an electric dipole, and emits radiation of the same frequency as the original exciting photon. Hence, in Rayleigh scattering the scattered photon has the same energy but a new direction relative to the incoming photon.

The important interactions for most of the energy range of interest in industrial radiography are photoelectric absorption and Compton scattering, with pair production becoming significant at higher energies [12]. In photoelectric absorption the photon is completely absorbed by an atomic electron. The electron is excited and emitted from the atom, which becomes ionised. The free electron then travels through the material, losing its kinetic energy through interactions within the material. If the electron is near the surface of the material it may escape, otherwise it will be reabsorbed into the material. The loss of an electron leaves the atom with a vacancy in one of its energy levels; this vacancy will be filled by a nearby free electron or a bound electron in a higher energy level. The process of filling the vacancy can cause x-ray fluorescence, in which a photon is emitted from the atom, or the Auger effect, in which a bound electron is emitted. The emitted photon or electron will go on to interact with other nearby atoms, often causing the release of additional electrons from nearby atoms. Hence, in general photoelectric absorption results in absorption of the x-ray photon and emission of multiple fast electrons.

Compton scattering is where the photon interacts with a bound electron, transferring a portion of energy to the electron. In addition to losing energy, the photon's direction is changed. The electron, known as a recoil electron, becomes free and will leave the atom at an angle relative to the scattered photon such that momentum is conserved. In Compton scattering the photon generally loses a fairly small proportion of its energy, meaning it may go on to reach the detector or to have additional interactions.

For high energy photons, over 1.022 MeV, pair production becomes possible. This is where the photon annihilates to create an electron-positron pair. The electron and positron will be dissipated through interactions in the material, with the electron quickly absorbed and the positron combining with a nearby electron to produce two photons with 0.51 MeV energy.

Both the photoelectric effect and Compton scattering can result in production of high energy electrons in the material. These high energy electrons

will be deflected by atomic nuclei, and emit Bremsstrahlung. Bremsstrahlung is radiation produced by deceleration of the electrons when interacting with other charged particles. The energy of the Bremsstrahlung depends on the extent of electron deceleration and forms a continuous spectrum, with the majority at low energies. Bremsstrahlung photons may go on to interact with other atoms or to reach the detector, and will therefore contribute to the amount and distribution of scatter detected.

The total attenuation coefficient and its components for different interactions in two materials, water and iron, are plotted in Figures 2.2 and 2.3 respectively.

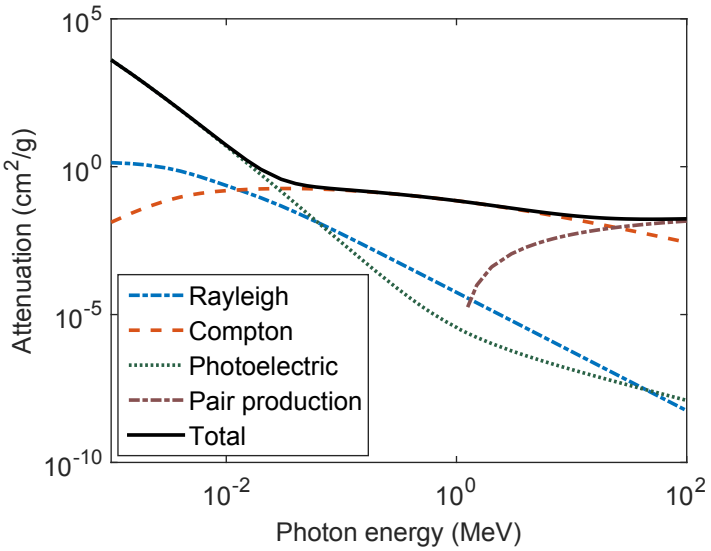

Figure 2.2: Total attenuation and its components for photons travelling through water. Total attenuation is a combination of atomic scattering and absorption effects whose relative probabilities change with photon energy. Data is from the XCOM online database [12].

Comparing the dominance of interactions in water, Fig 2.2, and iron, Fig 2.3, it can be seen why water is considered a highly scattering medium. In water photoelectric absorption is much weaker than in iron. Compton scattering in water is proportionately higher and becomes the most probable interaction at a lower energy (around 30 keV) compared to iron in which it is most probable from around 100 keV. Compton scattering degrades image quality by changing the direction of photons which will, if detected, reduce

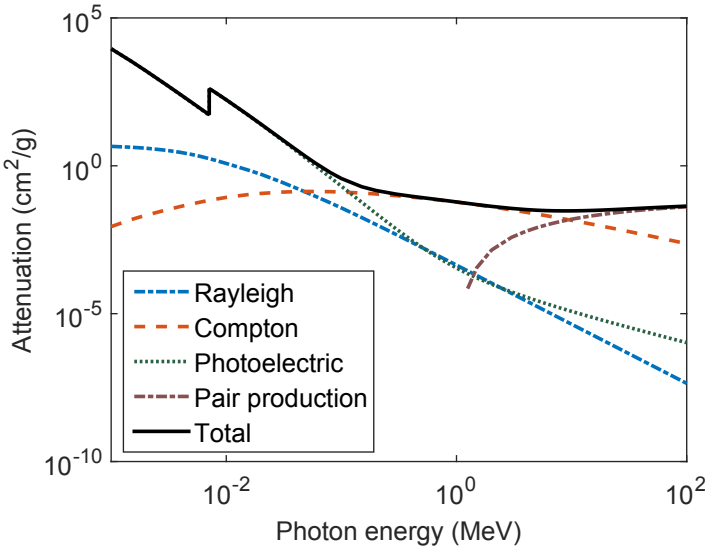

Figure 2.3: Total attenuation and its components for photons travelling through iron. Data is from the XCOM online database [12].

contrast in the image.

This demonstrates the potentially large negative impact that water, for example surrounding a subsea pipeline, can have on a radiographic image. Its density is high enough that the number of interactions is non-negligible while its probability of Compton scattering is relatively higher than other materials. Being able to accurately simulate the impact of water would be very useful as it would help determine detection limits and defect characterisation accuracy in real inspections.

2.2 Radiographic Equipment

2.2.1 Sources

Radiography may be performed using either x-rays or gamma rays. Both x-rays and gamma rays are high energy electromagnetic radiation; the main difference between them is in their method of production. Gamma rays are produced by radioactive decay of an unstable atomic nucleus, producing high energy photons at a few discrete energies. In addition beta or alpha particles may be released. Examples of radioactive isotopes commonly used in industrial radiography are Iridium-192 and Cobalt-60. Ir-192 releases

gamma rays at 0.31, 0.47, and 0.60 MeV while Co-60 releases energies of 1.17 and 1.33 MeV [16]. At these energies the gamma rays can penetrate thick materials in a short exposure time, making them well suited for in-situ radiography.

An example of the decay scheme of Co-60 is shown in Figure 2.4. The nucleus decays via beta decay, in which a neutron is transformed into a proton and a beta particle (electron) is released. In the case of Co-60 the beta particle emitted may be low or high energy, with the Nickel-60 daughter nucleus produced in a high or low energy state. The daughter nucleus will then release one or two gamma ray photons while transitioning to a lower, stable, energy level.

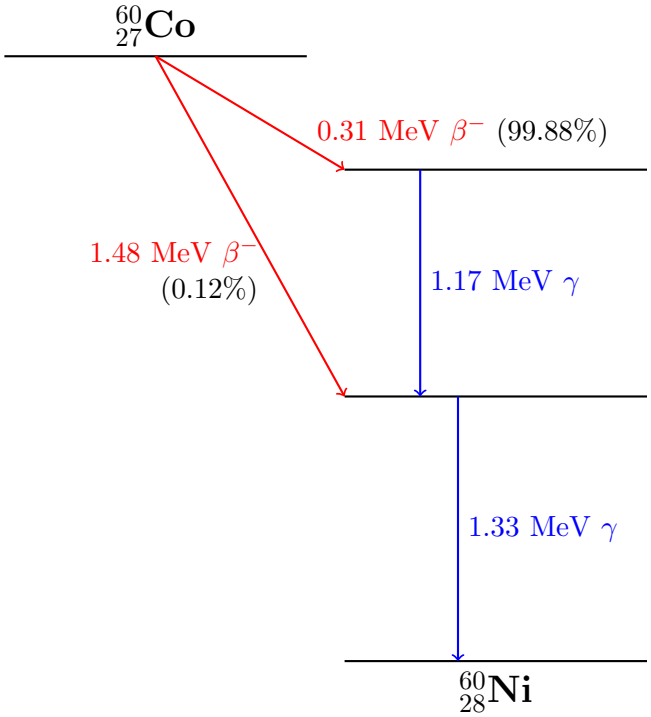

Figure 2.4: Decay scheme for Cobalt-60. The nucleus decays to Ni-60 through beta decay, releasing a beta particle with energy of either 0.31 MeV with 99.88% probability or 1.48 MeV with 0.12% probability. The Ni-60 nucleus is produced in an unstable, high energy level, and releases gamma ray photons in transitioning to a stable energy level.

Gamma ray sources cannot be turned off and are continuously releas-

ing photons; hence for safe usage the radioactive material is kept inside a shielded container. The amount of shielding required is dependent on the energy of the gamma rays, with higher energies needing more shielding. To release radiation the container must be opened; the source is also wound out of the container from a distance, once the operator is in a shielded location. Gamma ray sources are relatively small and portable, with most of their weight due to the shielding material. A typical isotope size is 1.5 mm x 1.5 mm, while the shielding material required for an Ir-192 source is about 20 kg and about 230 kg for a Co-60 source [16]. The isotope material in sources needs replacing regularly as its activity decreases over time.

X-ray sources are generally larger and less portable than gamma ray sources, and also require cooling. They often need larger exclusion zones than gamma rays, although this is dependent on source energies. In addition, x-ray sources require a power supply, which might not be readily available for an in-situ inspection. These are the main reasons for use of gamma rays instead of x-rays. The benefits of x-rays are that the generator can be turned off when not in use, so there are fewer health and safety issues, and the tube parameters, such as maximum voltage and current, can be adjusted to give an output suited to a particular inspection.

The method of x-ray production differs significantly from gamma rays. X-rays are generated when fast travelling electrons strike a target material. An example of an x-ray tube is shown in Figure 2.5. When a voltage is applied across the tube, electrons are accelerated from the filament on the cathode towards a target on the anode. The target is made of a dense, heat resistant material such as tungsten. When the electrons strike the target most of the energy is released as heat, hence a cooling mechanism must be used to prevent the target from melting. This may be a water cooling system or a method such as rotation of the target so no single point is exposed to heat continuously. About 1% of the electrons' energy is converted into high energy x-ray photons through the inverse photoelectric effect. X-rays are produced at all angles inside the tube; most will be absorbed in the tube walls, with a small window of thinner material allowing output in a particular direction.

Unlike gamma rays, which are produced at a few discrete energies, x-rays form a spectrum of energies. The maximum energy produced by an x-ray tube is determined by the voltage applied across the tube; for example a

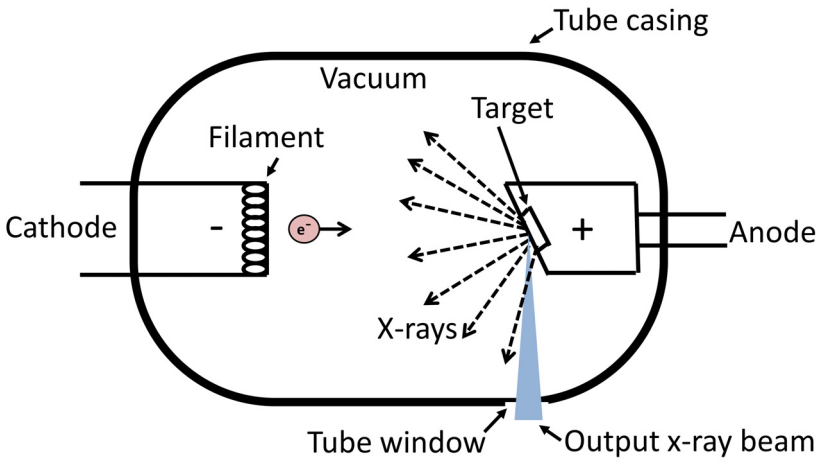

Figure 2.5: Example of an x-ray tube. Electrons are accelerated from the cathode to the anode in the vacuum tube. On striking the target most of the electrons' energy is dissipated as heat; about 1% is converted into x-rays. X-rays will leave the tube through the window, giving a relatively small aperture of useful x-rays.

voltage of 400 kV will release x-rays up to an energy of 400 keV. An example of an x-ray spectrum is shown in Figure 2.6. Most of the spectrum is made up of Bremsstrahlung, radiation produced though the inverse photoelectric effect. Bremsstrahlung mainly consists of low energy photons, with decreasing proportions of higher energies. However the lowest energies are easily absorbed and are filtered out by the tube window material. The sharp peaks at a few particular energies are produced by characteristic radiation from the target material. This occurs when a fast electron knocks a bound electron out of an atom in the target. An electron in a higher energy level will transition to the lower energy state, releasing a photon with energy equal to the difference between the two energy levels. Hence characteristic radiation is produced at a few discrete energies, with different energies produced by different material targets.

For inspections of thick components, which require high energies, alternative methods of x-ray generation may be used. The same principle of creating x-rays through bombardment of a target with fast electrons is used, however electrons can be accelerated to much greater speeds with the use of particle accelerators. In a betatron, electrons are accelerated in a circular path using the magnetic field generated in a coil. Electrons can reach much

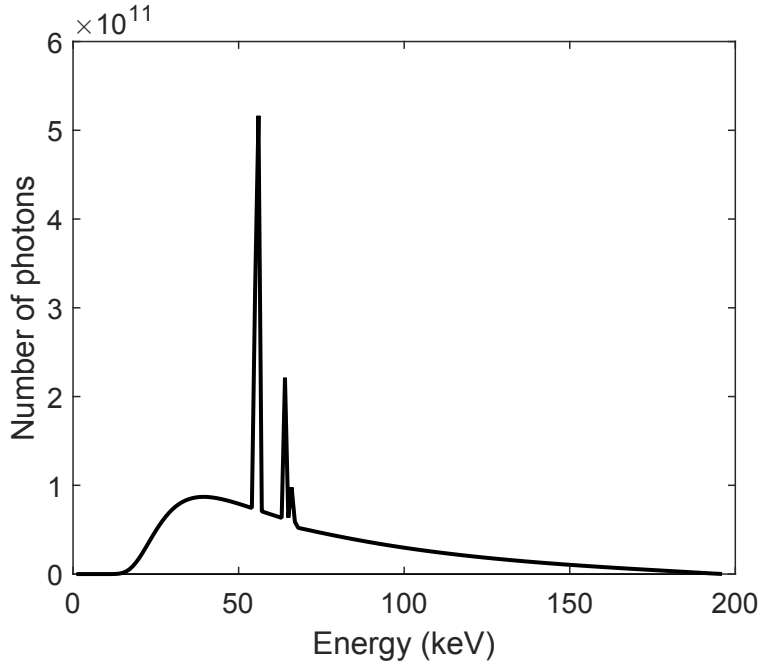

Figure 2.6: Example of an x-ray spectrum using a tungsten target and 4 mm thick aluminium tube window. Tube parameters for this simulated example were a voltage of 200 kV and a current of 1 mA.

greater speeds in this manner as they can repeat the circular path many times before being released towards the target. The maximum energy of x-rays produced by a betatron is limited by the magnetic field used. Typical betatron energies are from 2.5 to 9 MeV [17]. The number of photons output by a betatron is relatively low as it produces x-rays in short pulses rather than continuously. For higher output a linear accelerator (linac) may be used. A linac accelerates electrons along a tube using a high frequency electromagnetic wave [18]. X-ray energies in a similar range to betatrons are produced, the advantage being the much greater total output. Most linacs are very large, with for example an 8 MeV linac weighing 1200 kg [18], however portable versions are available. Betatrons are also relatively portable, with a 7.5 MeV betatron weighing about 150 kg [17], and are also cheaper than linacs. These traits make the betatron potentially useful for subsea pipeline imaging; the energy is high enough to penetrate large, insulated pipes, while it is sufficiently portable for a subsea setup to be feasible.

2.2.2 Detectors

Three different types of detector are used within industrial radiography; film, Computed Radiography (CR) and Digital Detector Arrays (DDAs). In recent years there has been a gradual move from film based systems to DDAs and CR systems. This has led to significant research comparing the different detector systems and identifying the strengths and weaknesses of each. The detector type used in subsea imaging will generally be a DDA, as this allows data to be transferred without physical retrieval of the detector. However, it is important to understand the uses and limitations of DDAs compared to film and CR systems.

Film is still commonly used due to its low initial cost and easy availability, although CR and DDA systems are becoming more prevalent. Radiographic film typically consists of an emulsion containing silver halide crystals, for example silver bromide [19]. When photons strike the film they can cause ionisation of the halide atoms; electrons will then be captured by Ag^+ ions. A latent image is formed from these changes in structure. When the film is developed the chemical reaction with the developer forms metallic silver [19], creating an image visible to the eye.

CR uses phosphor based imaging plates which, similarly to film, store a latent image when exposed to x-ray or gamma ray photons. In this case, the latent image is made up of electrons which have been excited from the valence band to the conduction band through absorption of a photon [20]. The latent image is read out by scanning the imaging plate with a laser; the energy from the laser releases the electrons from the conduction band. The electrons move back to the valence band, releasing visible photons which are detected by a photo-multiplier tube. Hence the image is read into a digital format. The process of scanning removes much of the latent image from the plate; to fully wipe the plate it is exposed to bright light after scanning [20]. The plates can be reused multiple times, and like film are flexible so they can be bent around a curved object.

DDAs, also called flat panel detectors, cannot be bent, and convert absorbed x-ray and gamma ray photons into a digital image, without any additional steps for reading the image as required by film and CR. DDAs may be direct or indirect; a direct detector converts absorbed photons directly into electron-hole pairs, while an indirect detector converts x-ray photons

into lower energy photons, in the visible light range, and from visible light into a current. Indirect detectors are more commonly used and consist of an x-ray scintillator, photodiode and thin film transistor, usually amorphous silicon [21, 22]. For more detail, technical aspects of digital detectors are reviewed by Lanca et al. (2009) [23, 24].

A major benefit of digital methods is the ease of data storage and transfer compared to film. Film also requires a dark room and various hazardous developing chemicals making it a difficult method to use in some situations such as offshore. Different detectors require different exposure parameters. Therefore in moving from film to CR or DDAs it must be ensured that operators are fully informed of the differences between the usage of each system; Shetty et al. (2011) [25] discuss artefacts found in medical CR images and identify that many are due to operator error.

As digital detectors began to enter NDE there was some concern over their lower image quality and limited uses compared to film [26]. The technology was primarily developed for medical applications where the suitable energy range is frequently lower than that required for industrial applications, with DDAs limited to fairly low energies (< 250 keV) [27]. Most digital systems also suffer from lower spatial resolution than NDT film, although new systems developed for dental radiology have improved resolutions. However, NDE specific research has found that contrast sensitivity of DDAs is greater than film if calibration algorithms are used [27]. It has also been found that DDAs can distinguish wall thickness changes of up to 1/1000 of the material thickness, in comparison to 1/100 for film systems [28]. By using DDAs with careful calibration as well as image integration techniques, where images are averaged to reduce noise, Kersting et al. (2010) [29] were able to obtain a signal-to-noise ratio at least twice as good as film, as well as an increase in probability of detection of weld seam defects. More recent work comparing image quality of CR with film for high energy LINAC x-rays [30] found similar performance for both systems, with CR having a greater dynamic range. For imaging components with greatly varying thicknesses this greater dynamic range means only one CR exposure may be needed, while film requires several exposures of different times to obtain the same information. The authors also comment on the usefulness of digital contrast enhancement tools commonly used with CR images, allowing more information to be obtained from the images.

As digital methods have become more prevalent, research has moved to the relative merits of CR versus DDA systems. Papers comparing the two [31, 32, 33] conclude that CR has a wider range of uses, being suitable for both stationary and mobile inspection and for use under difficult weather conditions. DDAs on the other hand require a stabilised temperature and humidity, and so are more suitable for stationary, in-house inspections [27]. With DDAs, a range of calibration techniques are available, as well as possible quality compensation methods, where one parameter is improved at the expense of others [34]. DDAs may also be able to obtain a better signal-to-noise ratio (SNR) than CR; image noise in CR is mostly determined by the imaging plate's structural noise, with a linear dependence on grey level. Calibration of DDAs is able to nearly eliminate structural noise, leading to a square-root dependence of SNR on grey level [35]. This ability to calibrate and reduce noise is a significant benefit to using DDAs subsea, in addition to the ease of data transfer which makes the use of a DDA essential in deep waters.

2.3 Pipeline Corrosion Imaging

Techniques of pipeline corrosion mapping with radiography have been investigated and standardised [3, 4] for use above water. Accepted inspection methods are the tangential and double wall techniques. The method currently used for practical subsea imaging is Double Wall Single Image (DWSI). An illustration of the system, which uses a digital detector combined with a 7.5 MeV betatron source, is shown in Figure 2.7. It is manipulated by a separate remotely operated vehicle (ROV), which can move the system axially along the pipe. In addition the source and detector can rotate around the pipe to take images at different angles.

In the DWSI method, shown in Fig 2.8 (a), the source and detector are placed close to each side of the pipe. As the upper wall is very close to the source any features are magnified across the whole detector, meaning that this method effectively just images the lower pipe wall, close to the detector. Corrosion is visible from the intensity change it causes, as more radiation reaches the detector in areas where the wall is thinner. The DWSI method is used in the current hardware as the relatively short source-to-detector distance reduces the highly attenuating and scattering effects of

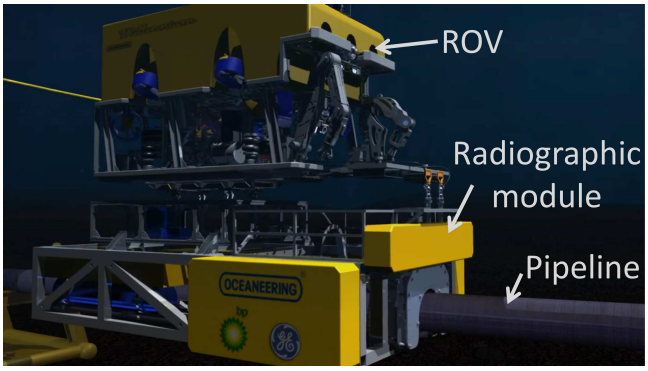

Figure 2.7: [36] Illustration of a subsea pipeline radiography system. The radiographic module contains a betatron source and a digital detector which can be rotated around the pipe. The separate ROV can move the system axially along the pipeline.

the water. A variant of double wall imaging is Double Wall Double Image (DWDI), shown in Fig 2.8 (b), in which the source is set back from the pipe. In this case the upper wall is not magnified to the same extent, and both upper and lower pipe walls can be clearly imaged in a single exposure. In tangential imaging, Fig 2.8 (c), the source is set back as in DWDI but the detector is offset such that the edge of the pipe is visible in the radiograph. Wall thickness at the tangential position can be measured on the resulting radiograph directly, as the inner and outer wall positions are points of major intensity change and therefore identifiable in a profile across the image.

In order to accurately measure wall thickness in a tangential image the image must be dimensionally calibrated. The calibration is required to take into account magnification effects in the setup. There are several different methods of calibration; the magnification can be manually calculated from known setup dimensions, alternatively if the pipe outer diameter is known and the full diameter is visible in the image the magnification can be calculated as the ratio of the known and measured diameters. Accurate knowledge of setup dimensions may be difficult in-service, while for larger pipes the full outer diameter will not be visible in an image. In these cases a comparator must be included in the setup. A comparator is an object of known size such as a ball bearing or cylinder. The comparator must be made of a dense material such that it is clearly visible in a radiograph, and is placed in a tangential position on the outer pipe wall [3]. The image can

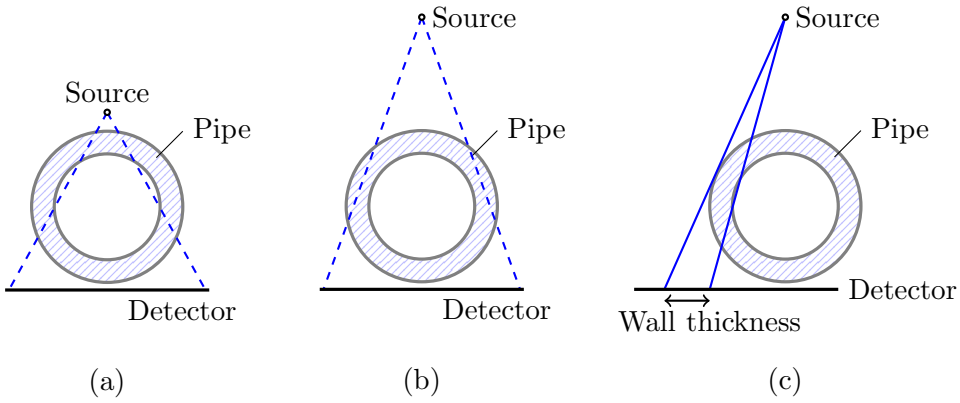

Figure 2.8: Standardised methods of radiographic imaging of pipelines for corrosion mapping. (a): Double Wall Single Image, where the source is placed close to the upper pipe wall (EN 16407: part 2 [4]). In Double Wall Double Image, (b), the source is set further back (EN 16407: part 2 [4]). Tangential Imaging, (c), allows direct measurement of the wall thickness at the tangential position (EN 16407: part 1 [3])

then be calibrated by comparing the actual and measured comparator sizes.

In double wall radiography measurements of wall thickness loss are dependent on intensities. Absolute thickness cannot be measured with this method, instead the difference in thickness between two nearby points is calculated. The difference in thickness between two points can be derived from the Beer-Lambert Law, Equation 2.1, if the incident intensity and attenuation coefficients at the two points are assumed the same [4]:

$$x_2 - x_1 = \frac{1}{\mu} \ln \frac{I(x_1)}{I(x_2)} \tag{2.2}$$

where μ is the effective attenuation coefficient and x_1 and x_2 are the penetrated thicknesses at the two points, with $I(x_1)$ and $I_(x_2)$ the corresponding intensities. The effective attenuation coefficient accounts for the overall attenuation experienced travelling from source to detector and depends on both the materials travelled through and the photon energies. In order to use Equation 2.2 the effective attenuation coefficient needs to be measured; this is done with a step wedge placed in the setup. The step thicknesses must be known, and the step wedge placed as close as possible to the area of interest [4]. If the step wedge is not sufficiently close to the area of interest the result will be inaccurate. This is because the effective attenuation coef-

ficient is likely to be different in other regions of the image, due to different paths travelled from the source to detector.

2.4 Image Analysis

Radiographic images can be analysed and compared using a series of image quality parameters. These include the basic spatial resolution ($SR_b^{detector}$), Signal-to-Noise ratio (SNR) and Contrast-to-Noise ratio (CNR). Image Quality Indicators (IQIs) are used to aid image analysis and measurement of image quality parameters. In general IQIs provide a quick idea of the quality of an image, prior to detailed measurement. There are several different types of IQI; one of the most commonly used is the wire type IQI [37]. A wire IQI consists of a series of wires of decreasing diameter; the smallest diameter wire visible in a radiograph gives an indication of the overall quality of the image. The wires in the IQI must be made of a similar material to the sample, and the range of wire diameters in the IQI used should be decided based on the sample thickness. The correct placement of IQIs in a radiographic setup is detailed in the relevant standards for the inspection type. For example for a DWSI pipe inspection the IQI should be placed on the detector side of the object, while for a DWDI setup the IQI should be on the source side of the object [4]. In both cases the IQI should be in close contact with the object surface and at the centre of the area of interest.

Other types of IQI in use are step/hole and hole-in-plaque types [37]. The step/hole type consists of a step wedge with one or two holes in each step, with hole diameter equal to step thickness. The hole-in-plaque IQI, commonly used in the US, is a uniform thickness plaque with holes of diameter one, two and four times the plaque thickness. In both these IQI types the smallest visible hole indicates the image quality.

Wire IQIs also come in the form of duplex wires, which can be used to measure image unsharpness and hence basic spatial resolution. Duplex wire IQIs are formed of pairs of wires with both decreasing diameters and a decreasing distance between them. For $SR_b^{detector}$ measurement a duplex wire IQI is placed on the detector in an exposure. The inherent image unsharpness is determined from the smallest duplex wire pair which is separable by a profile function with less than 20% modulation depth, in a linearized profile [38]. $SR_b^{detector}$ is related to the inherent image unsharpness, u_i by

the simple equation [3]:

$$SR_b^{detector} = \frac{1}{2}u_i \tag{2.3}$$

An example of $\mathrm{SR}_b^{detector}$ measurement is shown in Figure 2.9.

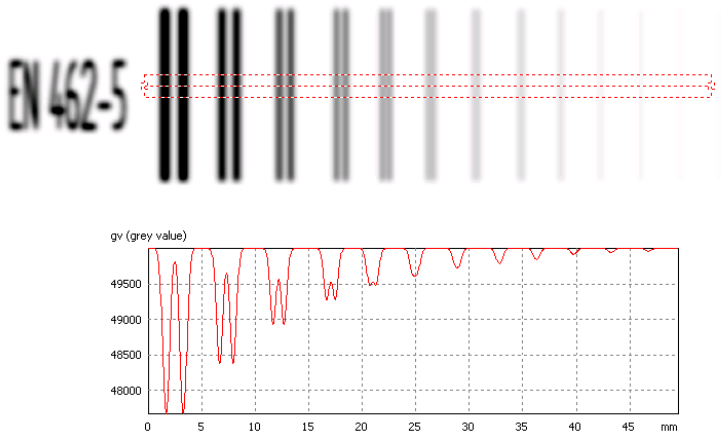

Figure 2.9: Measurement of basic spatial resolution. Top: Section of a simulated radiograph showing a duplex wire IQI. Bottom: Plot of a profile through the duplex IQI image. The basic spatial resolution is found from the first pair of wires for which the peak in between the pair is less than 20% of the dip caused by each wire, in this example the fifth wire pair. This identifies the wire pair as the smallest separable wires.

For a more precise basic spatial resolution calculation, interpolation between neighbouring pairs of wires can be used. This can identify the exact size corresponding to 20% modulation depth in the profile, meaning $\mathrm{SR}_b^{detector}$ does not have to be based on the closest wire to that point. $\mathrm{SR}_b^{detector}$ which has been calculated through interpolation is called $\mathrm{iSR}_b^{detector}$ [3].

Image unsharpness is a measure of the gradual change in intensity across a sharp thickness change in an object. Inherent unsharpness depends on the system and energy in use and is caused by the spreading out of a detected photon into neighbouring detector pixels. This is usually through stray electrons, which cause the neighbouring pixels to detect some signal, resulting in a smearing of a sharp edge across several pixels. Another form of unsharpness which affects the image is called geometric unsharpness. This

type of unsharpness is a blurring due to the finite size of the source. Geometric unsharpness depends on the source to detector distance (SDD) and the object to detector distance (ODD) and can be reduced by increasing the SDD or decreasing the ODD. Total image unsharpness is calculated as a combination of geometric and inherent unsharpness.

Further measurements are required to numerically determine the signal-to-noise and contrast-to-noise ratios. Signal-to-noise ratio is defined as the ratio of the mean value of the grey level to the standard deviation of the grey level in a given region of the image [3]. In practice a rectangular region of interest is taken in an area of the image free from significant intensity changes. For each horizontal line of pixels i, with n pixels per line, the mean grey level ($\overline{GV_i}$) and sample standard deviation (σ_i) are given by [39]:

$$\overline{GV_i} = \frac{1}{n}\sum_{j=1}^{n} GV_{ij} \tag{2.4}$$

$$\sigma_i = \sqrt{\frac{1}{n-1}\sum_{j=1}^{n}(GV_{ij} - \overline{GV_i})^2} \tag{2.5}$$

where GV_{ij} is the grey level at line i and column j in the region of interest. These are calculated for each horizontal line of pixels, where there are M lines. Signal-to-noise ratio is then given by:

$$SNR = \frac{Median\left[\overline{GV_i}\right]_{i=1}^{M}}{Median[\sigma_i]_{i=1}^{M}} \tag{2.6}$$

This is the unnormalised SNR, which has a dependency on the radiographic system used. Normalised SNR, SNR_N, is a more useful measure as it removes this dependency. SNR_N can be calculated from [39]:

$$SNR_N = SNR.\frac{88.6\mu m}{iSR_b} \tag{2.7}$$

where iSR_b is the interpolated basic spatial resolution of the image.

The contrast, C, of an object in a radiograph is given by [40]:

$$C = I - I_{obj} = \Delta I \tag{2.8}$$

where I_{obj} is the intensity measured on the object indication and I the

intensity nearby. The contrast-to-noise ratio can then be calculated from:

$$CNR = \frac{|\Delta I|}{\sigma} \tag{2.9}$$

where σ is the standard deviation measured in an area near the intensity measurements. Another measure is the relative contrast (Cr). Cr is independent of the noise and is instead based on the relative change in grey level, given by:

$$Cr = \frac{|\Delta I|}{I} \tag{2.10}$$

Relative contrast is particularly useful when comparing images with different noise or grey levels in the area of measurement.

2.5 Computed Tomography

Computed Tomography (CT) is a method of obtaining a full 3D representation of an object using x-ray images. In CT multiple radiographic projections are taken at different positions and angles around the object. The data is collected into a sinogram, which is an array representing the data as a function of projection angle and translational distance. The sinogram can then be reconstructed into a 3D representation of the object.

The simplest form of CT is parallel ray, also called pencil beam CT. This is where a single small detector is used to detect a collimated beam of radiation through the object. The detector and source are translated across the object to obtain a series of projections, then rotated by a small angle and translated back. This process is shown in Figure 2.10.

Parallel ray CT has the disadvantage of a long acquisition time. Other methods have been developed to decrease acquisition time by increasing the size of the detectors and using partially collimated or uncollimated sources. Fan beam CT uses a 1D line detector and therefore collects a line of data from each angle, meaning the source/detector system only needs to rotate around the object, not translate across. In both pencil beam and fan beam CT the result is a 2D slice through the object. In order to get a full 3D representation, the process must be repeated at a different position along the object to obtain multiple slices. In cone beam CT a 2D detector is used, so only rotation is required for 3D reconstruction.

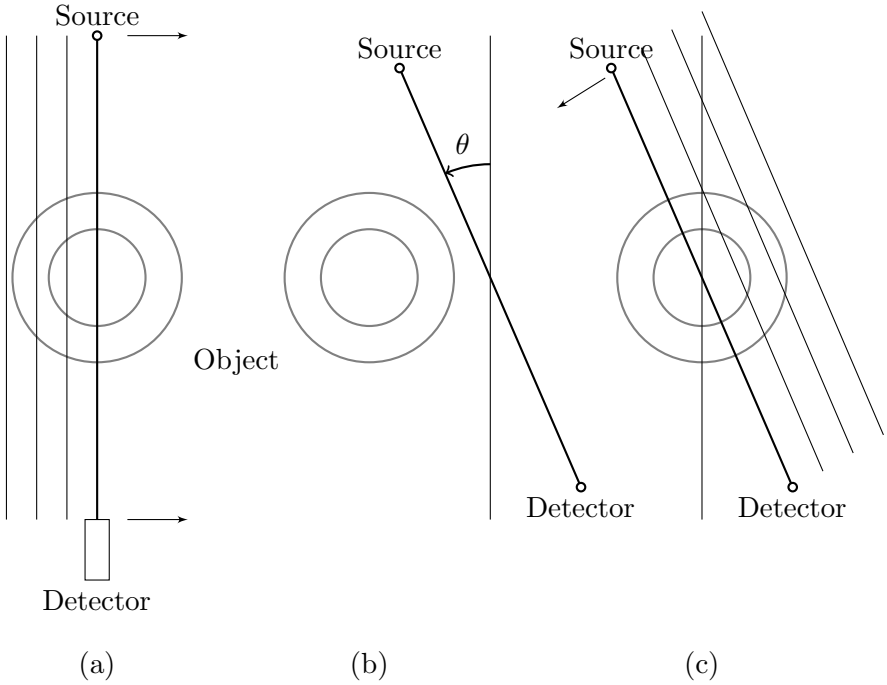

Figure 2.10: Parallel CT involves the source and detector translating across the object, as in (a). They are then rotated, (b), and translated back, (c). This process is repeated to acquire a full set of data. The source is collimated to produce a pencil beam.

Total angular coverage of 360° is not required for parallel CT since projections 180° apart are mirror images of each other, however taking additional projections will reduce the noise in the resulting reconstruction. For a fan-beam set-up, an object can be reconstructed using 180° plus the fan beam angle [41]. Reconstructing from the fan beam data also requires additional filtering due to some regions being sampled more than others, creating artefacts.

Mathematically radiographic data collection is equivalent to a Radon transform, summing up the attenuation across each source-detector line. Reconstruction is an inverse Radon transform, and consists of 'smearing' the data back along the angle at which it was obtained, a process known as back-projection. This is a simple process for parallel CT, where each projection is acquired at the same distance from the source, with a known angle and position. However for fan and cone beams it becomes more complicated and data must either be resorted and interpolated into corresponding par-

allel beam data or back-projected with a weighting to account for diverging beam geometry [41].

The most commonly used fan-beam CT reconstruction method is the Filtered Back-Projection (FBP) technique, described in many papers and in some detail by Kak & Slaney [41]. This method was extended for cone-beam geometry by Feldkamp et al. (1984) [42] into a method known as the Feldkamp or FDK algorithm after the authors. The FDK algorithm has become the standard cone-beam reconstruction method in NDT due to its straightforward approach [43]. The technique of CT results in a full reconstruction of the object, allowing for easy and accurate identification and characterisation of defects. However, it is extremely time consuming in comparison to a single radiographic inspection, needing a large number of projections to obtain a good quality result. Limited view CT is an active research area attempting to develop reconstruction algorithms that can deal with fewer projections and still produce reasonable quality images. Standard CT algorithms such as FDK result in low quality images with many artefacts if used on limited data [44].

Algorithms for limited view reconstruction have been investigated for many years in an effort to reduce scan time and medical dosage. One of the first iterative methods, the algebraic reconstruction technique (ART) was first proposed by Gorden et al. (1970) [45]. This technique was expanded into the simultaneous algebraic reconstruction technique (SART) [46], and the two methods are still popular iterative methods often used as comparisons against new algorithms. Other early methods include Bayesian techniques to incorporate prior information into reconstructions from incomplete data, described by Hanson (1987) [47]. There are a variety of other more recent reconstruction methods. Tang et al. (2009) [48] gives an overview of different statistical image reconstruction (SIR) algorithms. Li et al. (2002) [49] proposes an iterative method to reconstruct sparse objects from a limited number of cone beam projections, able to achieve good reconstructions from as few as 15 projections. However most objects do not satisfy the sparseness condition of relatively few non-zero pixels which is assumed by their algorithm [50].

Sidky et al. (2008) [50] uses simulations to demonstrate the performance of their circular cone-beam reconstruction algorithm, based on total variation (TV) minimization. The algorithm assumes that images have sparse

gradient-magnitude images, and demonstrates reasonable reconstructions with 25 projection views. TV minimization is a commonly used method, often in combination with other algorithms [51, 52, 53]. TV algorithms often cause over-smoothness at the image edges; Liu et al. (2012) [54] present an adaptive-weighted TV minimisation algorithm that compensates for this effect. Similar to the TV method the compressed sensing (CS) reconstruction technique relies on solving a constrained minimization problem; Chen et al. (2008) [55] extend and improve the method, obtaining accurate reconstructions with about 20 view angles. Singh et al. (2008) [56] presents a method of reconstruction and image segmentation based on constrained metric labelling. Constrained metric labelling uses the fact that the object has a set of distinct attenuation values which are known, while a reconstruction typically shows a spread of attenuation values due to blurring and streak artefacts. If the attenuation values in the reconstruction are constrained to be from the subset of known values, then the problem reduces to assigning each voxel to its 'best-fit' value. The study proposes an algorithm that reassigns image voxel values in this manner. Results show greatly reduced streak and blurring artefacts from a limited view of 20 projections, as compared to standard ART. There are many possible artefacts that may be caused by limited view methods, some of these are detailed by Machida et al. (2010) [57], where the relationships between acquisition parameters and potential artefacts are explained.

Although limited view CT methods provide a significant time saving compared to full CT, they still require many more projections than would be feasible for subsea imaging. In addition, the double wall single image setup is not ideal for CT: if the source is placed directly on the insulation then there will be areas of the pipe not covered in the field of view (FOV) for any given exposure. This means that some areas of the object will have a greater total exposure, and therefore intensity discontinuities will be seen in the reconstruction. These artefacts are known as truncated projection artefacts (TPAs) and are described by Yao et al. (2013) [58], where a processing method to reduce these artefacts is detailed. Jian et al. (2007) [59] also covers this type of artefact, from the point of view of CT of large objects, where the object is not entirely covered by the FOV. In this case the author proposes a method of taking additional projections at offset positions to reduce artefacts.

Another imaging method, for which TPAs are a particular problem, is tomosynthesis. Tomosynthesis is a pseudotomographic imaging technique that uses a limited number of projections over a small angular range to reconstruct a quasi-3D image [60]. Tomosynthesis is considered an extreme form of limited view computed tomography. It has been developed in medicine for the particular use of breast cancer detection, with the aim of overcoming some of the limitations of mammography, while keeping the dose minimal. Due to its main area of application, it is usually referred to as digital breast tomosynthesis (DBT). DBT does not result in a fully 3D image; due to the very limited angular range of projections, the spatial resolution in the depth direction is very low compared to the other directions. Many CT reconstruction algorithms can also be used for DBT, such as filtered back-projection (FBP) and the algebraic reconstruction technique (ART). Nielsen et al. (2012) [61] describes a modification to the standard FBP method, to account for the specific acquisition geometry. However, there are many proposed algorithms specifically for DBT. A recent review, Sechopoulos (2013) [62], describes different algorithms and gives a comprehensive review of the research into comparisons between reconstruction methods. These types of reconstruction methods, even if not directly applicable subsea due to time and cost or setup constraints, can give an insight into potential methods of defect characterisation in subsea pipeline radiography.

3 Radiographic Simulation Model

3.1 Introduction

In the initial phase of the project a radiographic simulation model, PRIM (Pipeline-specific Radiographic Inspection Model), was developed. The aim of the development was twofold; to provide a simple, fast alternative to commercially available models and to help with understanding of methods used in the commercial models. With the project focus on subsea pipelines the model could be optimised for pipeline inspection configurations, giving lower versatility but much faster computational times. However, effects such as pair production and electron transport were not included in PRIM, meaning it is not as accurate as commercial models, particularly for higher energies. Hence PRIM can be used to quickly visualise the expected radiograph for an inspection configuration and to adjust simulation parameters for an optimum image, before moving on to simulate the inspection with more accurate commercial models.

Scattering in PRIM is simulated using a Monte Carlo technique, a commonly used method of simulating scatter [63, 64, 65, 66]. Monte Carlo methods are often used where it is difficult to deterministically solve a problem. This is the case for photon scattering, as it is not possible to calculate the exact path of a photon, only the probability of each possible path. In the Monte Carlo algorithm random sampling is used to decide on a photon's interactions, based on the relative probabilities of each interaction. While any given photon will follow a random path, summing the results of many photons will give a realistic distribution based on these underlying probabilities. If run for long enough Monte Carlo methods will accurately simulate both direct and scattered radiation, producing the complete radiograph. However the computing time required would be correspondingly high; therefore many models have applied a method of combining a straight-line analytical model using the Beer-Lambert Law, Equation 2.1, with a Monte Carlo

method used to add scattering effects [64, 67, 68]. This is the technique applied in PRIM.

PRIM is coded in C++, with additional post-processing of the output in Matlab. Inputs to the model are in the form of text files, such that only those needed in a particular setup are read in. Inputs needed include tables of attenuation data for each material in a setup, tabulated source energy data and further material details such as density and atomic number. To model a material the simulation requires attenuation data, so any desired compound or alloy could be simulated if its attenuation data is available or can be calculated. The attenuation data used in PRIM was obtained from the XCOM online database [12]. The source used can be specified as Ir-192, Se-75 or Co-60, the three most commonly used isotopes in industrial radiography. Alternately, simple monoenergetic sources can be specified. The model also incorporates x-ray sources; these are more complicated to model as they consist of a continuous spectrum of energies, while gamma sources have several discrete energies. The method to include x-ray sources involves interpolating between energies to obtain the attenuation at numerous energies along the spectrum. The model does not generate x-ray tube spectra, hence the desired x-ray spectrum must be provided in the form of a text file. Variable setup parameters such as dimensions, exposure conditions and defect type are also set in a text file, giving a very basic user interface and meaning simulations can be run without editing the source code.

As the project is focussed on imaging of pipelines the model assumes a pipe as object. This means the surface of the pipe can be included analytically rather than as a CAD model type object. The simplest pipe is assumed to be a perfect cylindrical tube, however pipe ovality or smooth variations in pipe wall thickness can be included for a more realistic pipe. The pipe can also be insulated, with the insulation assumed to be a cylindrical tube, again with the option of ovality or smooth variation in thickness. The material of each component in the simulation; the pipe, insulation, inside pipe, defect and surroundings, can all be set independently. Simple cylindrical or spherical defect shapes are also modelled analytically. For more complex, non-analytical defect shapes, a voxelisation method is used. The defect domain is bounded by a sphere within which the defect is discretised into volume elements called voxels. Each voxel is set as a particular material, allowing arbitrary shaped defects to be included.

The analytical ray tracing component of the model is described in the next section, followed by the Monte Carlo method of scattering simulation. Results are then compared against two commercially available radiographic simulation models: CIVA [69, 70] and aRTist [71]. CIVA is a model developed by CEA LIST [72] in France. aRTist (analytical RT inspection simulation tool) is developed by the Institute of Materials Testing (BAM) [6] in Berlin.

3.2 Analytical Ray Tracing Model

The analytical part of the model is based on the Beer-Lambert Law (Eqn 2.1) and calculates the proportion of unscattered radiation reaching the detector. The method is to trace straight-line rays from the source to the centre of each detector pixel, identifying the distance travelled through each material along the way. Each section of the ray in a different material is dealt with in turn, adding the product of material attenuation (μ) and distance through the material (x) to a running total. Since objects in the model are included analytically, the path of a ray through each object can be found by calculating the intersection points of the ray and object. Modelling each ray consists of tracing the ray from one intersection point to the next until it reaches the detector. Figure 3.1 shows the path of two example rays from the source to the detector. The method is slightly different if a voxelised defect is included. In this case an algorithm to calculate the path of a straight line through a series of cubic voxels is used. The algorithm used was derived from Siddon's algorithm published in 1985 [73] and using improvements by Jacobs et al [74].

The coding methodology is summarised in the flow chart in Figure 3.2. For each detector pixel the equation of the straight line from source to pixel is derived. This is used to calculate the first intersection point and the distance travelled in the current material to find the first μx. The position along the ray is updated to the intersection point. If the intersection is with the pipe wall or insulation then the material value is updated and the process repeated for the next intersection point. If the intersection is with the bounding sphere of the defect then the voxel algorithm is used to calculate μx through the defect, until the ray exits the bounding sphere and the process of finding the next intersection is repeated. When there are no

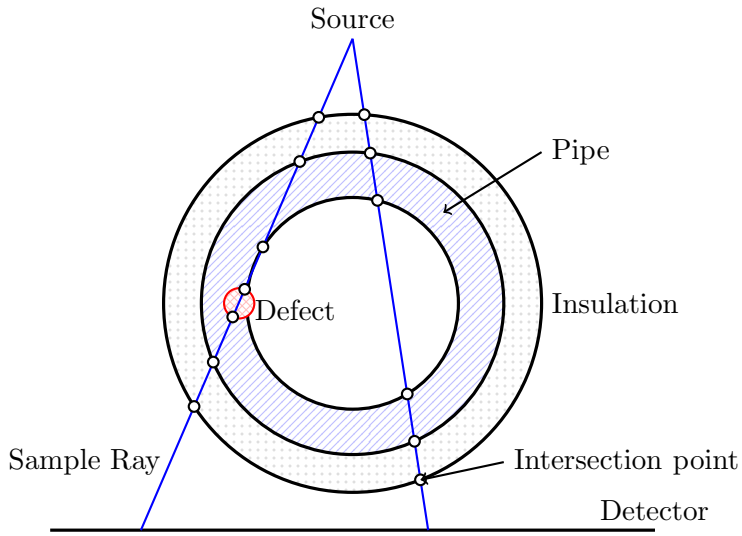

Figure 3.1: Example showing the method of ray path calculation; intersection points are calculated and the ray is traced between points, adding to the total μx along each section. If the ray enters the defect bounding sphere a separate calculation of the path through cubic voxels is used until the ray leaves the sphere. The figure shows a simplified cross-section through the set-up.

intersection points left, then the distance remaining to the detector pixel is used to find the final component of μx. The intensity reaching the pixel can be found using the sum of μx over the ray's entire path. A probability of detection factor is calculated, depending on the detector's material and thickness; this probability can also be set to one for a perfect detector. The intensity reaching the detector is multiplied by the probability of detection factor to calculate the detected intensity. This is a very simplistic detector model and likely overestimates defect detectability. In reality detectors are extremely complex and can be difficult to model accurately.

The intensity reaching the detector is also normalised to account for the pixel area and the spreading out of the beam from the source, resulting in the total intensity reaching the pixel area. This detected intensity is stored in the detector and the algorithm moves to the next pixel. Once all pixels have been simulated the final detector is output in a simple matrix format that can be read into Matlab for examination and processing. The model has the option of running just an analytical calculation, which typically takes less than two seconds, or including a scattering simulation. The scattering

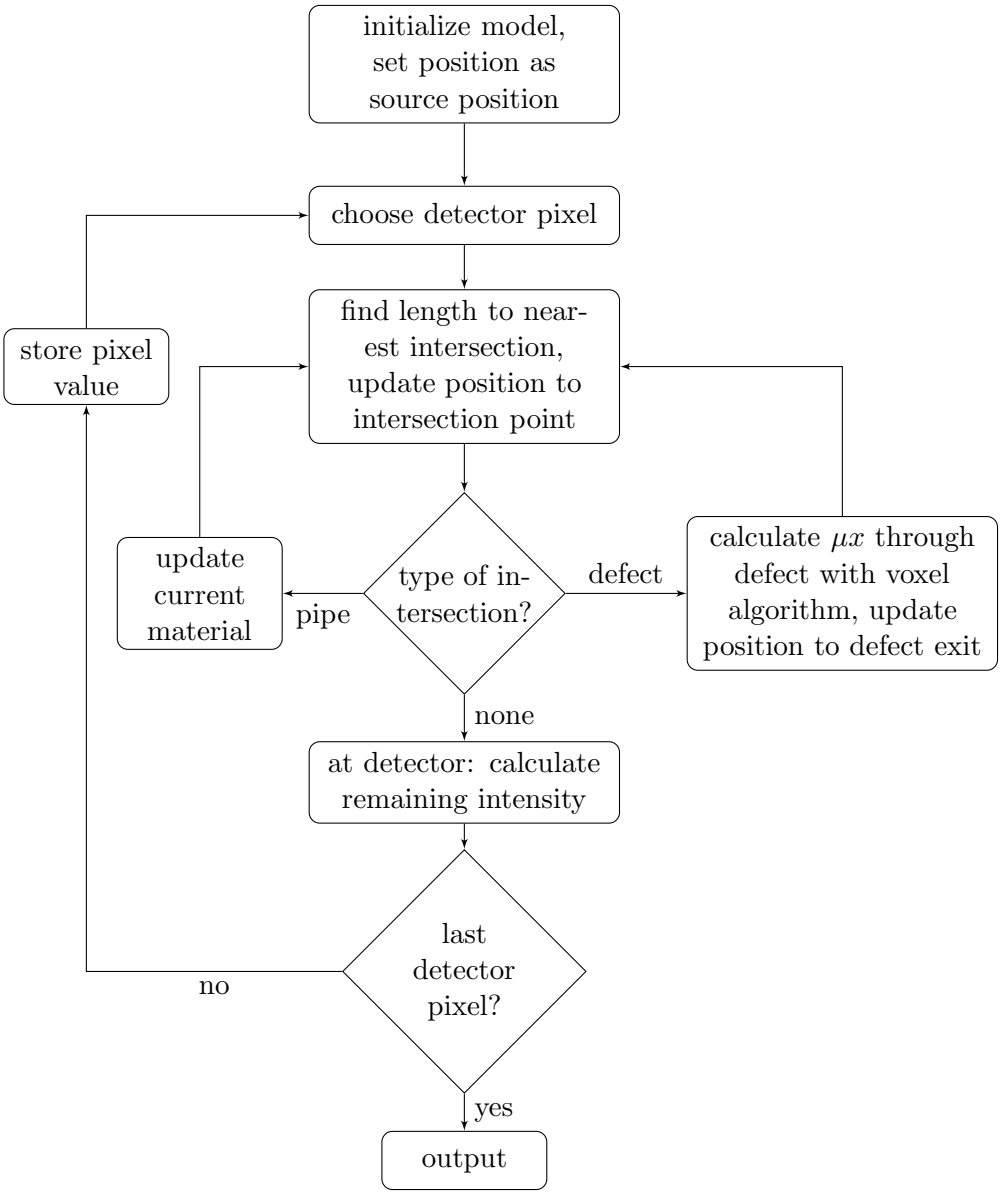

Figure 3.2: Flowchart showing the method of simulating the direct radiation reaching the detector.

simulation is run independently of the analytical calculation, with separate output files. A Matlab program is used for combination of scattering and analytical results to produce the final expected radiograph. The method of simulating scatter using a Monte Carlo technique is described in detail in the next section.

3.3 Monte Carlo Scattering Method

In the scattering Monte Carlo simulation each photon is traced individually. The total number of photons is set by the user before running. The number of photons required depends on the size of the setup and the photon energies; lower energy or thicker materials in the setup will need more photons in order to get a significant number reaching the detector. Estimating the required number of photons is an open issue, and currently no commercial simulation model offers this. The number of simulated photons is generally an extremely small percentage of the experimental number. As an example, a new cobalt source will have an activity of about 20 to 100 curies [75], where one curie is equal to 3.7×10^{10} atomic disintegrations per second. In most cases each cobalt atom decay will release two gamma rays, as seen in Fig 2.4. So for a 60 second exposure, a 20 curie source will release about 9×10^{13} photons. In this case a typical simulation, with 10^8 photons, will be modelling approximately one photon for every million actual photons.

In the model, each photon is initialised with a random direction within the specified source opening angle. If the source is polychromatic the photon energy will also be chosen randomly, based on the relative probabilities of the possible energies. Once initialised, the first step is to calculate the distance the photon will travel before interacting. This distance, s, is given by [76]:

$$s = -\frac{\ln r}{\mu} \tag{3.1}$$

where μ is the total attenuation coefficient of the material the photon is in, and r is a random number uniformly distributed in the interval (0,1). Attenuation is dependent on photon energy, and since the attenuation data is obtained in tabular form it must be interpolated to find attenuation at the particular energy of the photon. The interpolation method used is log-log cubic-spline for energies above the K-shell absorption edge and linear log-log fitting for energies below, this is as used in the XCOM database [12].

Equation 3.1 can be derived by considering the probability density function of the photon's free path [77]. However the equation assumes constant attenuation along the photon's path; it does not take into account crossing material boundaries. One of the benefits of the Monte Carlo method

is its simplicity when dealing with boundaries. Photon transport can be modelled as a Markov process [77], meaning future events can be predicted solely based on the current state, regardless of past events. This means that a photon can be stopped at any point and then restarted without changing the results. Therefore if the photon reaches a material boundary before it interacts, it is stopped at the boundary and restarted with a new value of s, generated with the updated material attenuation and a new random number. Boundaries are calculated by finding the intersection points of a straight line in the direction of the photon with each of the setup objects. If a voxelised defect is used and the photon is inside it then each voxel is treated as if it were a new material, with a new s calculated every time the photon crosses to a new voxel.

Once the photon reaches an interaction point the type of interaction is chosen. To do this the interval (0,1) is split into subintervals with lengths proportional to the relative probabilities of each interaction type. A random number is used to choose a subinterval and thus an event type. The interaction is resolved and, if it has not been absorbed, the photon's energy and direction are updated. A new s is then calculated and the process repeated. Simulation of the photon will complete when it is either absorbed, reaches the detector or leaves the specified limits of the simulation domain. The overall algorithm structure is illustrated in the flowchart in Figure 3.3.

The interaction types included in PRIM are the photoelectric effect, Compton scattering and Rayleigh scattering. The simplest of these to model is the photoelectric effect, in which the photon is completely absorbed. In reality, photoelectric absorption of a photon will result in the release of one or more electrons and characteristic x-ray photons. However, these secondary effects are not modelled in PRIM, so if the photoelectric effect occurs the simulation of that photon is completed and the algorithm moves on to simulate the next photon. If Compton scattering occurs then the photon energy loss and scattering angle must be calculated; the photon direction and energy are then updated and the photon is moved on until another interaction occurs. Rayleigh scattering also requires calculation of the scattering angle, although there is no energy loss; after scattering the photon's direction is updated before continuing to another interaction.

The scattering angle can be split into the azimuthal and polar scattering angles. For both Rayleigh and Compton scattering the azimuthal angle, ϕ,

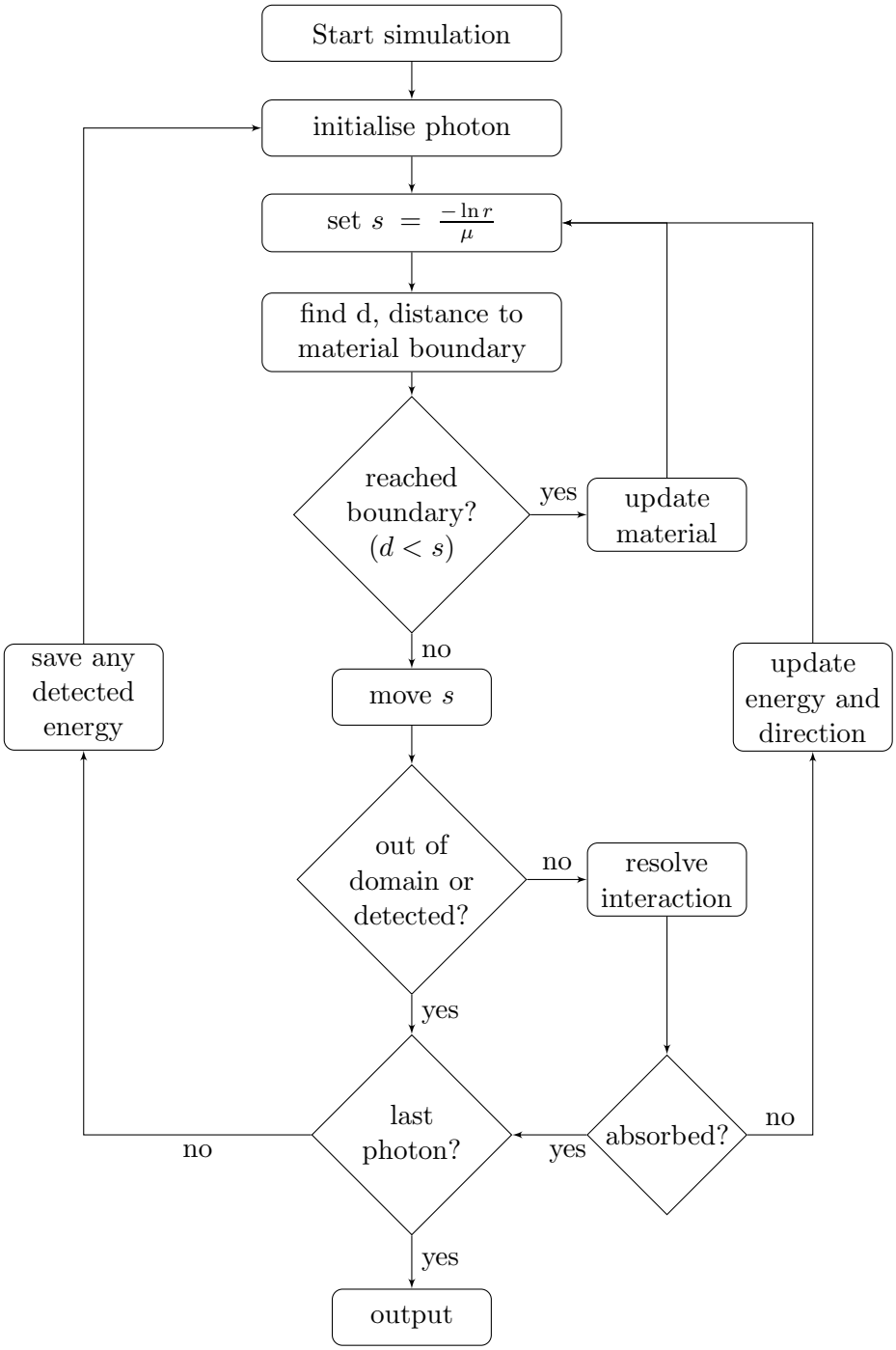

Figure 3.3: Flowchart showing the method of simulating the scattered radiation.

follows a uniform distribution in the interval (0,2π) and is easily selected using a random number. The polar angle, θ, follows a more complex probability distribution [78, 79]. In PRIM, scattering is simplified by assuming no electron binding effects. Jaenisch et al (2006) [80] compares a scattering simulation with and without electron binding. The intensity of scattered radiation due to Rayleigh scattering is found to increase if binding effects are included; this is mainly due to Rayleigh scattering having increased forward directivity. Conversely Compton scattering has reduced forward directivity when electron binding effects are considered, with results showing a decrease in scatter. However, the differences were only examined at a source energy of 100 keV. At higher energies, photon energy is large compared to electron binding energy and hence binding effects can be neglected for Compton scattering [81]. Similarly for Rayleigh scattering; at higher energies the probability of Rayleigh scattering is very small compared to Compton, and thus binding effects will have negligible impact.

The accept-reject method of sampling is used to decide the scattering angle θ. This method is well described by Hirayama et al (2005) among others [77, 82]. The details of the algorithm used follow that described in Fulea et al (2009) [79]. For Rayleigh scattering this involves sampling the differential Thomson cross section:

$$\frac{d\sigma_T(\theta)}{d\Omega} = \frac{r_e^2[1+\cos^2\theta]}{2} \tag{3.2}$$

where σ_T is the Thomson scattering cross section and r_e is the electron radius. The scattering angle θ can be found with:

$$\theta = \cos^{-1}(1-u) \tag{3.3}$$

where $u = 2r$ and r is a random number in the (0,1) interval. A weighting variable which represents the main θ dependency, $w = [1+\cos^2\theta]$, is used: if $w > 2r$, where r is another random number, then θ is accepted. If not, the process is repeated with new random numbers until a value of θ is accepted.

For Compton scattering the probability distribution of the scattering angle is given by the Klein-Nishina equation [79]:

$$\frac{d\sigma_{KN}(E,\theta)}{d\Omega} = \frac{r_e^2}{2}\frac{E}{E_0}\left[1+\left(\frac{E}{E_0}\right)^2 - \frac{E}{E_0}\sin^2\theta\right] \tag{3.4}$$

where E_0 is the initial photon energy, r_e is the electron radius, θ the scattering angle and E the energy of the photon after scattering, given by:

$$E = \frac{E_0}{1 + \frac{E_0}{m_0 c^2}[1 - \cos\theta]} \tag{3.5}$$

where $m_0 c^2 = 512$ keV is the electron rest mass.

The method of sampling is similar to that for Rayleigh scattering; in this case the weighting variable used is:

$$w = \left[1 + \left(\frac{E}{E_0}\right)^2 - \frac{E}{E_0}\sin^2\theta\right] \tag{3.6}$$

θ is again generated using Equation 3.3, with the value of u given by:

$$u = \frac{m_0 c^2}{E_0}\left[\left(1 + 2\frac{E_0}{m_0 c^2}\right)^r - 1\right] \tag{3.7}$$

where r is a new random number. The value of θ is accepted if $w > 2r$, if not the process is repeated. This method of selecting θ is summarised in the flowchart in Figure 3.4.

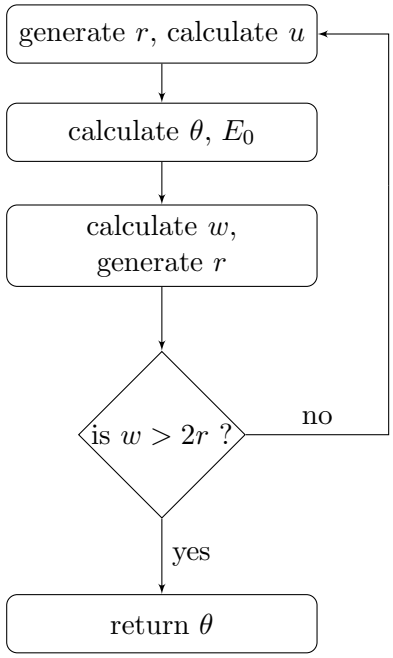

Figure 3.4: Flowchart showing the accept-reject method of sampling used for Compton and Rayleigh scattering angle calculation.

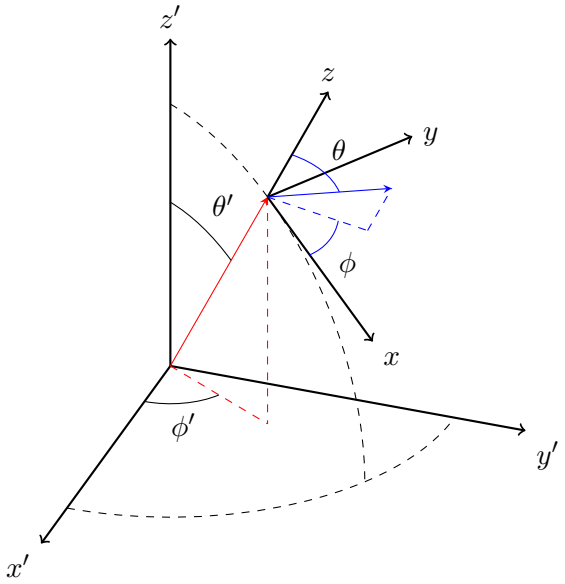

Figure 3.5: Coordinate system of the photon. θ and ϕ are the scattering angles, calculated relative to the photon's direction. They must be transformed back to the object coordinate system to calculate the direction of the photon after scattering. θ' and ϕ' give the photon's direction in the object frame before scattering.

The scattering angles are visualised in Figure 3.5. The scattering angles, θ and ϕ, are calculated relative to the photon direction. Therefore the photon's new direction, after scattering, must be transformed into the object frame of reference. To calculate the photon's new velocity in the object coordinate system, rotation matrices are applied. For initial photon velocity unit vector (v_x, v_y, v_z) with scattering angles θ and ϕ the new direction of the photon, (v'_x, v'_y, v'_z) is given by [78]:

$$v'_x = \frac{\sin\theta(v_x v_z \cos\phi - v_y \sin\phi)}{\sqrt{1-v_z^2}} + v_x \cos\theta \tag{3.8}$$

$$v'_y = \frac{\sin\theta(v_y v_z \cos\phi - v_x \sin\phi)}{\sqrt{1-v_z^2}} + v_y \cos\theta \tag{3.9}$$

$$v'_z = -\sin\theta\cos\phi\sqrt{1-v_z^2} + v_z \cos\theta \tag{3.10}$$

or if v_z is very close to 1:

$$v'_x = \sin\theta\cos\phi \tag{3.11}$$

$$v'_y = \sin\theta\sin\phi \tag{3.12}$$

$$v'_z = SIGN(v_z)\cos\theta \tag{3.13}$$

where $SIGN(v_z)$ returns -1 for negative v_z and $+1$ for positive v_z.

Once the scattering angles have been computed the photon's energy and direction are updated, and a new interaction site calculated using Equation 3.1. This is repeated for each photon until all have been absorbed, left the domain or reached the detector. To reduce run-time, photons are stopped if they reach a lower bound cut-off energy below which they are considered negligible; in most simulations this is set to 10 keV but is adjustable.

Random number generation is a key part of a Monte Carlo simulation. Software based methods generate pseudo-random numbers which pass most of the tests for randomness, but have a period after which the sequence repeats. Generators included in standard C++ libraries tend to have low periods, making them unsuitable for use in Monte Carlo methods. The pseudo-random number generator used in this model is the Mersenne twister MT19937 developed and coded by Matsumoto et al [83], and available online [84]. The authors find the algorithm to be suitable for a Monte Carlo simulation due to its period of $2^{19937} - 1$, much longer than most others, while it also obtains similar speeds [83].

Since each photon is independent of all the others the code has been parallelised with OpenMP to run on multiple CPU cores. To allow for parallel processing a new random number generator is defined in each thread using the thread number as the seed. This allows each thread to run independently, saving any detected energy to a shared memory detector after each photon run.

In order to get a full representation of a radiograph the analytical ray tracing and the Monte Carlo results are combined. The method used follows that described by Tabary et al (2004) in [67]; full details can be found in the paper, with a brief description given here. The method involves running two Monte Carlo simulations; these must be uncorrelated and simulate the same number of photons. The scatter image is calculated as the sum of the two Monte Carlo results, which is then filtered using a low-pass Butterworth

filter. The filtered image is scaled to the analytical dose using the average ratio between the analytical result and the direct radiation calculated in the Monte Carlo simulation. The scaled image can then be added to the analytical result, giving a combination of direct and scattered radiation. Noise also needs to be added. The noise is found by first subtracting the two Monte Carlo results, and calculating the variance of the resulting image. The variance is scaled to the analytical dose, using the same ratio as for the scatter image scaling. It is then used along with a Gaussian random number to calculate the final noise image. The final noise is added to the analytical and scatter images, giving the complete radiograph.

3.4 Results

To verify results, PRIM has been compared against CIVA and aRTist. A range of setups were compared to identify any causes of mismatch. Materials used included water, plastic, iron, lead and air, giving a good range of attenuation behaviours. Energies were between 200 keV and 1.2 MeV, with monoenergetic, gamma ray and x-ray sources used. Results were split into the analytical, direct Monte Carlo and scattered Monte Carlo components, with each compared separately to ensure a match in each component of the models.

An example of a simple test case is an iron block object with 50 mm thickness, and 150 mm side length in both other dimensions. Source to detector distance was 50 mm, with a detector size of 51.2 mm^2 and 512×512 pixels. A monoenergetic 1 MeV source was used, with a cone opening angle of 80 degrees and 1×10^{10} photons simulated in the Monte Carlo run. The resulting total energy reaching the detector, as calculated in the Monte Carlo method in PRIM, is shown in Figure 3.6. This Monte Carlo result was compared with the same setup simulated in aRTist. Example cross-sections through the detectors are plotted, with direct radiation shown in Figure 3.7 and scattered radiation in Figure 3.8. These show a good match between the models.

A second simple setup tested was of an iron pipe, with outer diameter 320 mm and wall thickness 25 mm. No defects or insulation were added to the setup, and the source used was again a monoenergetic 1 MeV, with a source to detector distance of 400 mm. The detector had a side length

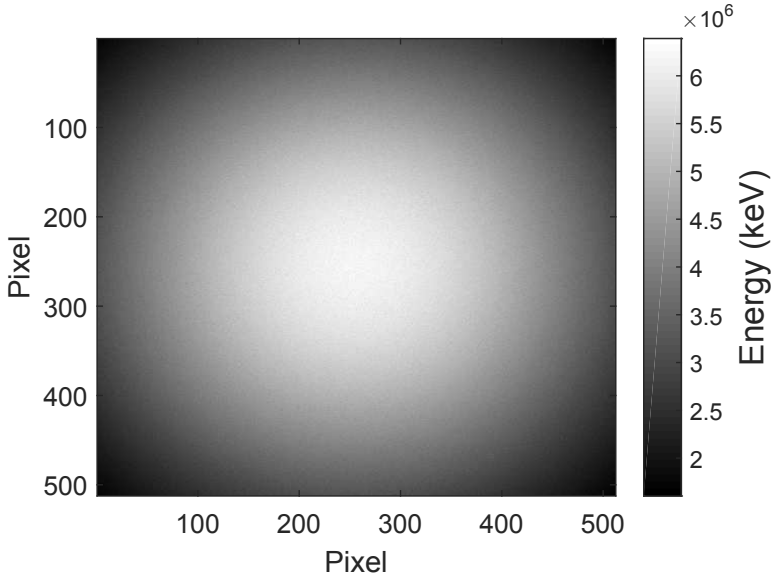

Figure 3.6: Total energy reaching the detector for a 50 mm iron block. Calculated using the Monte Carlo method in PRIM.

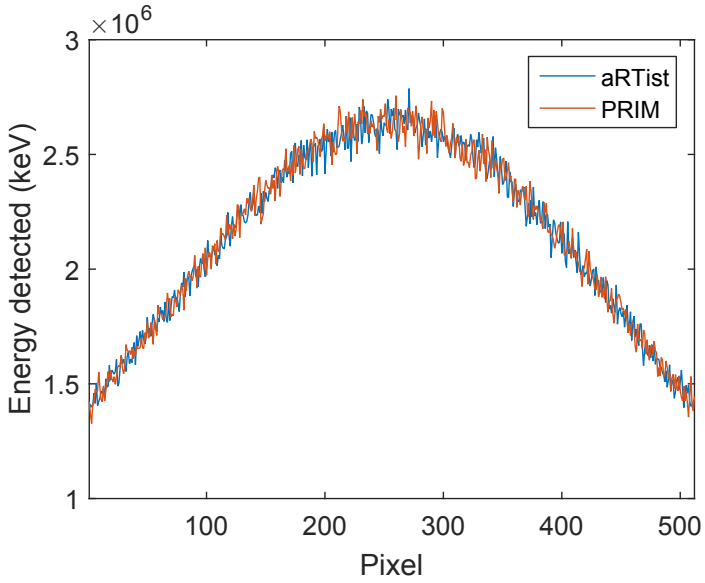

Figure 3.7: Comparison of direct radiation reaching the detector in aRTist and PRIM for a 50 mm iron block. The plot shows cross-sections through the centre of the detector, at pixel 256. Calculated from the Monte Carlo method in both cases.

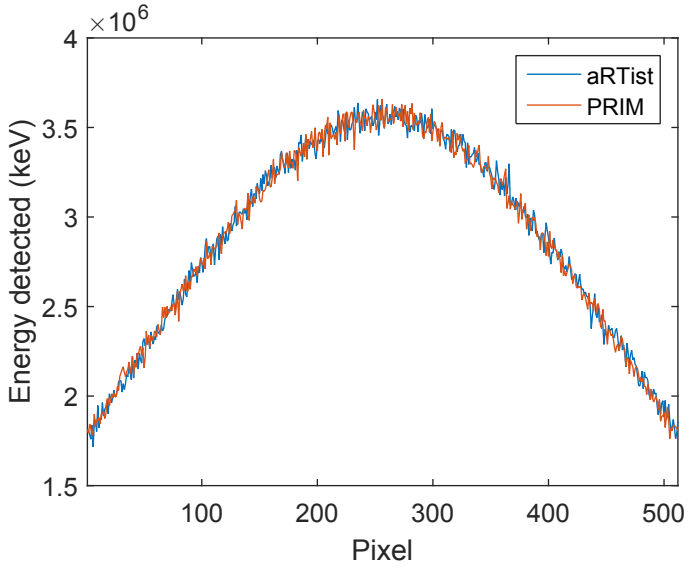

Figure 3.8: Comparison of scattered radiation reaching the detector in aRTist and PRIM for a 50 mm iron block. The plot shows cross-sections through the centre of the detector, at pixel 256. Calculated from the Monte Carlo method in both cases.

of 409.6 mm corresponding to 1024 pixels. Monte Carlo simulations were run in both aRTist and PRIM and results compared. Again a good match was found between the models; an example of cross-sections through the detector is shown in Figure 3.9.

The simple setups involving blocks and basic pipes were found to produce good agreement between the different models in all cases. More complex setups, containing multiple materials and objects were then tested. The next section details two example setups and results for simulations compared with CIVA. This is followed by another two examples, this time compared with aRTist.

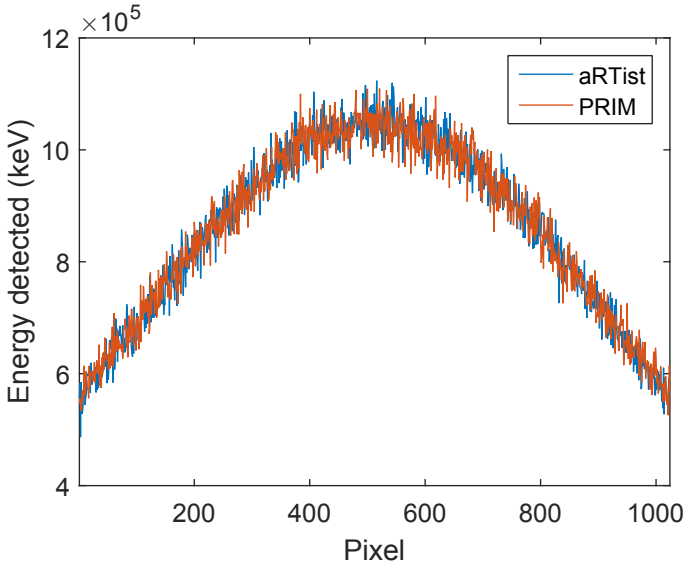

Figure 3.9: Total energy reaching the detector for a 320 mm outer diameter pipe. Calculated using the Monte Carlo method with 1×10^{10} photons.

3.4.1 Comparison with CIVA

Two sets of results are detailed here; together they demonstrate and verify some of the capabilities of PRIM. Figure 3.10 shows the setup for the first example. The setup includes many factors to test; different materials, a range of distances and sizes and a lead sphere modelled using the analytical defect method.

Both the Monte Carlo and the ray-tracing simulation were run on this set-up. Parameters used were 1×10^9 photons for the Monte Carlo and 100 s exposure time with a 1×10^9 Bq activity source for the ray-tracing model. The source is collimated into a 45° half-angle cone for the Monte Carlo simulation and is uncollimated in the ray-tracing model. The analytical result produced by PRIM is shown in Figure 3.11. For model validation the same set-up was modelled in CIVA. For comparison a cross-section is taken through the centre of the detector perpendicular to the pipe axis. Results for the analytical, direct Monte Carlo and scattered Monte Carlo are plotted in Figures 3.12, 3.13 and 3.14 respectively. In all cases CIVA results match those from PRIM very well.

To increase the complexity of the test case an insulation layer was added

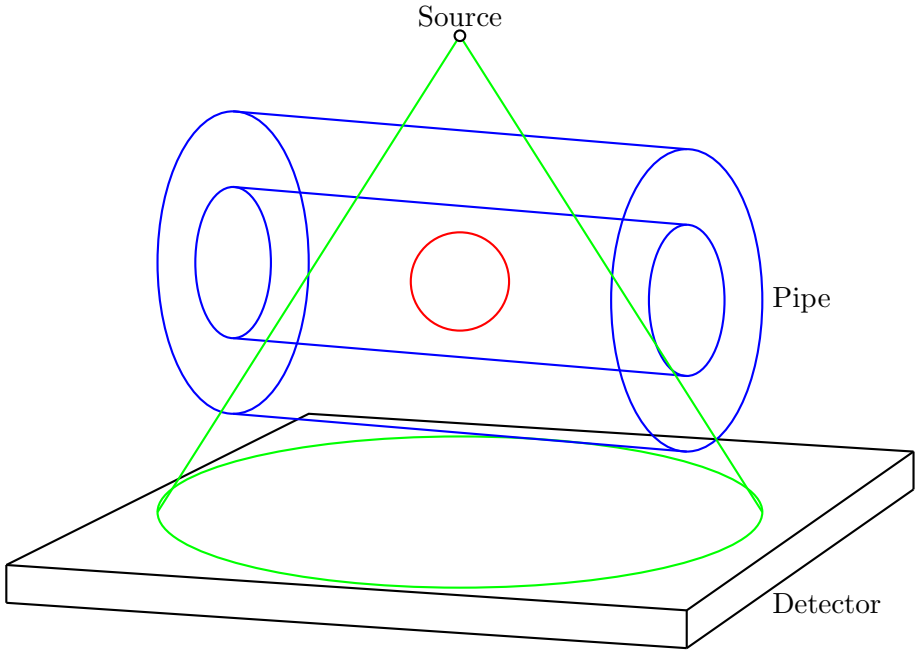

Figure 3.10: Test case used for model validation. The pipe is not insulated and is surrounded by a vacuum. The pipe material is iron and it contains water. To test defect inclusion a spherical ball of lead is modelled inside the pipeline at the centre of the set-up. The source is a monoenergetic 1 MeV. The detector is a perfect detector for the Monte Carlo method. Its size is 100 $\times$ 100 mm^2 and it consists of 800 $\times$ 800 pixels. The source to detector distance is 50 mm, pipe outer diameter is 30 mm and wall thickness is 5 mm. Diameter of the sphere is 6 mm.

with a thickness of 9.5 mm, leaving gaps of 0.5 mm at each side between object and the source and detector. A medium attenuation element, calcium, was used as the material. In addition to this the lead sphere was changed to a lead cube of side 8 mm and its position offset from the centre of the domain in all three coordinates. This tests the defect voxelisation method as it is modelling a cube set within a bounding sphere. The source was also changed from monoenergetic 1 MeV to a Cobalt-60 gamma ray source, with all other parameters kept constant. A Cobalt-60 source is high enough energy that pair production would occur; an interaction not included in either PRIM the version of CIVA (10.1) used in this work. However, pair production is not significant until photon energies of several MeV, as seen in Fig 2.2, so neglecting it for a Co-60 source will not have a noticeable impact.

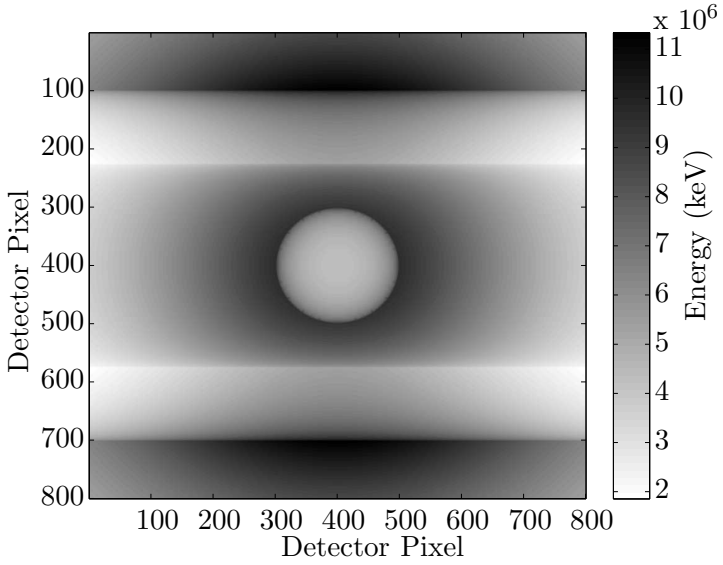

Figure 3.11: Full analytical result calculated by PRIM for the case of a water filled pipe containing a lead sphere. The source is uncollimated, monoenergetic 1 MeV.

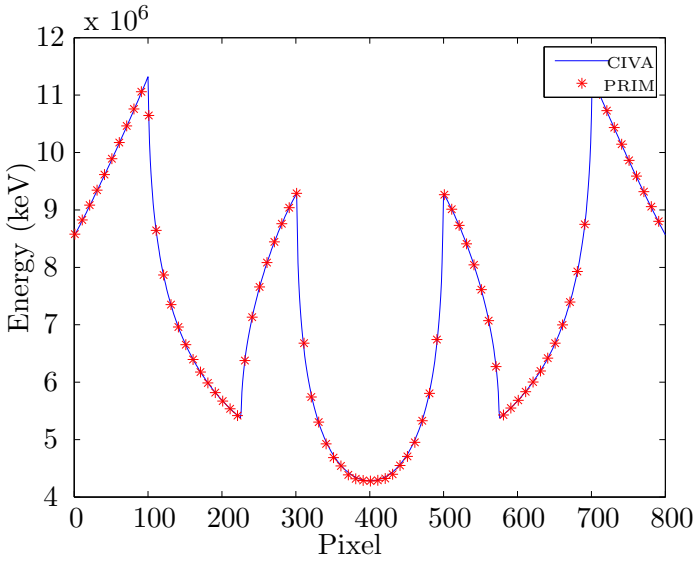

Figure 3.12: Cross-section through the analytical result for the case of a water filled pipe containing a lead sphere, calculated with both PRIM and CIVA.

Figure 3.15 shows the resulting analytical radiograph calculated in PRIM. A cross-section through the centre of the analytical detector, perpendicular

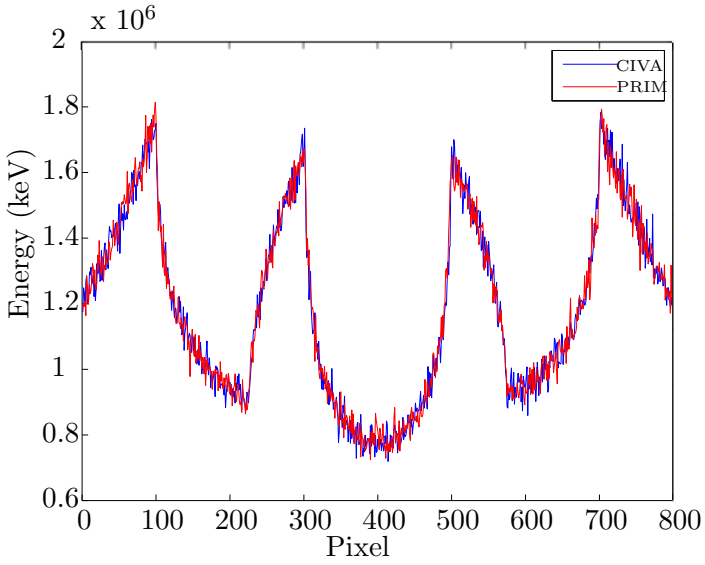

Figure 3.13: Comparison of direct Monte Carlo result in PRIM and CIVA, for the case of a water filled pipe containing a lead sphere.

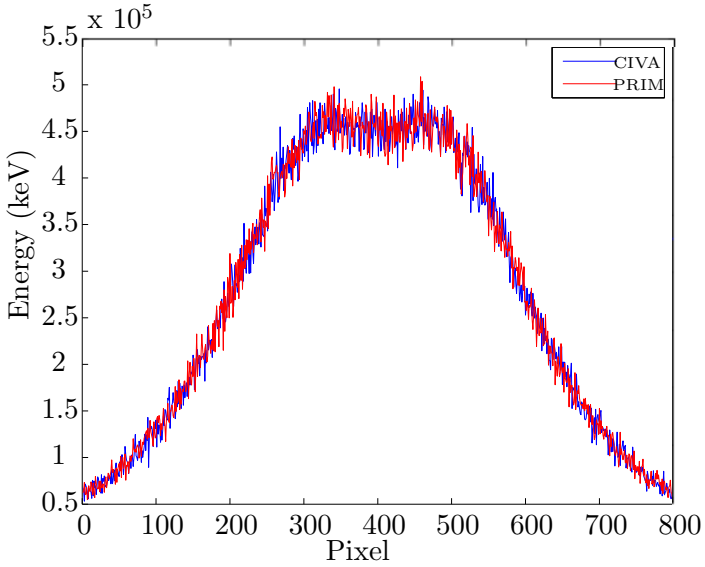

Figure 3.14: Comparison of scattered Monte Carlo result in PRIM and CIVA, for the case of a water filled pipe containing a lead sphere.

to the pipe axis, is shown in Figure 3.16, along with the result from CIVA. A comparison of cross-sections 10 mm (80 pixels) from the centre so as to cross the lead cube area is shown in Figure 3.17.

Results are shown in Figures 3.15 to 3.19. Figure 3.15 shows the radiograph resulting from the ray-tracing method. A cross-section through the centre of the detector perpendicular to the pipe axis is shown in Figure 3.16, and a cross-section 10 mm (80 pixels) from the centre so as to cross the lead cube area is shown in Figure 3.17. Results along this same cross-section for the direct and scattered Monte Carlo simulation are shown in Figures 3.18 and 3.19.

As an example of the time taken for the simulation to run, this PRIM Monte Carlo simulation took just under 8 minutes, while the same set-up in CIVA took 36 minutes. Both were run on the same standard desktop computer, with an eight core processor and eight gigabytes of RAM. The analytical method took less than 2 minutes in both models.

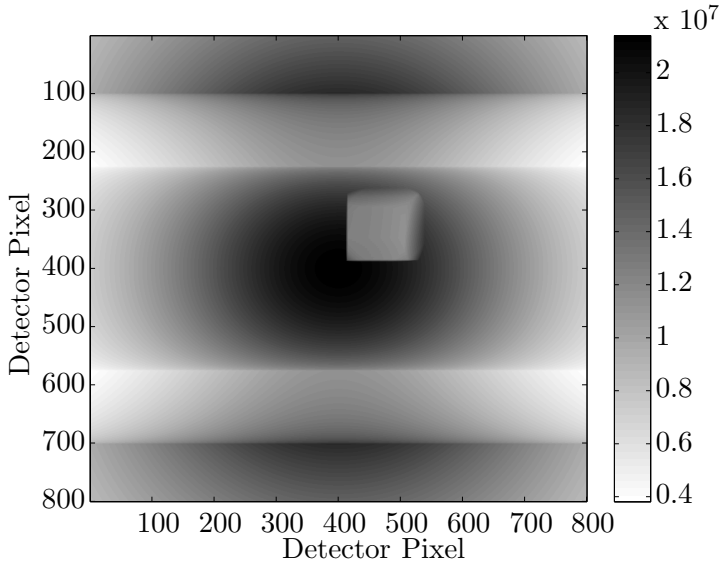

Figure 3.15: Full analytical result calculated by PRIM for the case of an insulated, water filled pipe, containing a lead cube. The source is Cobalt-60.

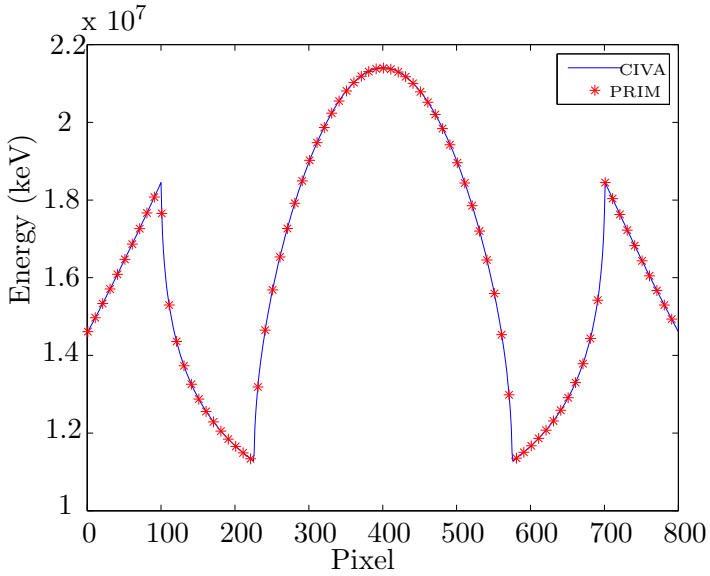

Figure 3.16: Cross-section through the centre of the analytical result for the case of an insulated, water filled pipe, containing a lead cube. Calculated with both PRIM and CIVA.

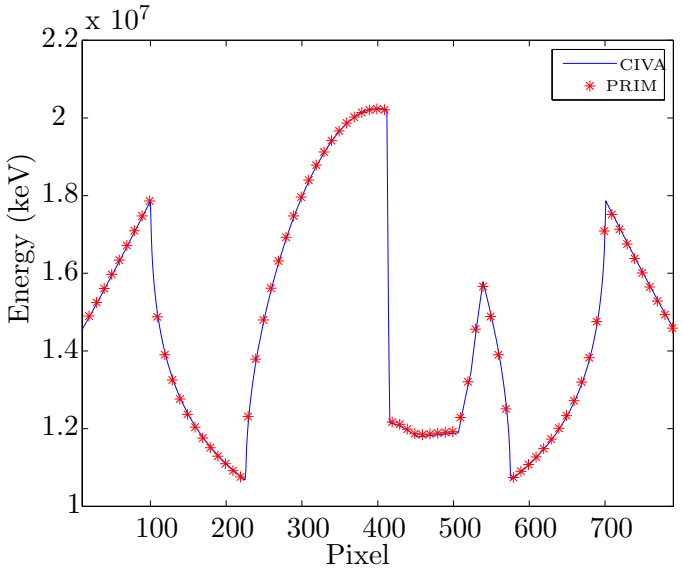

Figure 3.17: Cross-section through the analytical result, 10 mm along pipe from the centre, for the case of an insulated, water filled pipe, containing a lead cube. Calculated with both PRIM and CIVA.

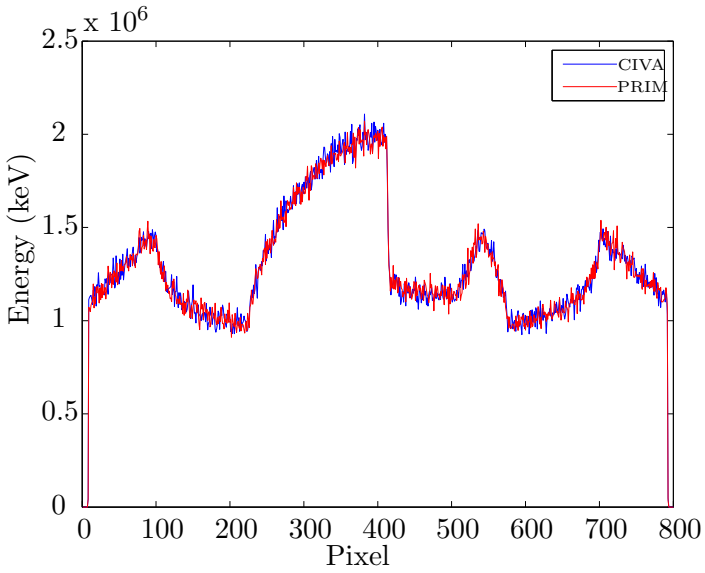

Figure 3.18: Cross-section through the direct Monte Carlo result, 10 mm along pipe from the centre, for the case of an insulated, water filled pipe, containing a lead cube. Calculated with both PRIM and CIVA.

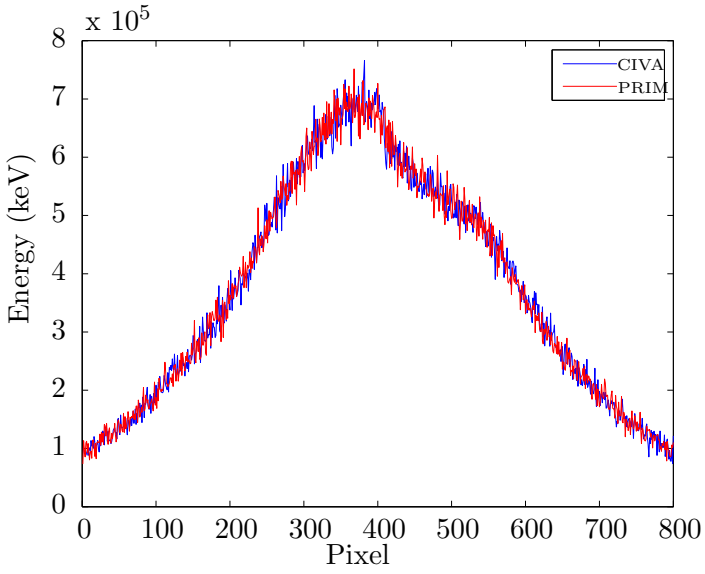

Figure 3.19: Cross-section through the scattered Monte Carlo result, 10 mm along pipe from the centre, for the case of an insulated, water filled pipe, containing a lead cube. Calculated with both PRIM and CIVA.

3.4.2 Comparison with aRTist

Two larger and more realistic simulation setups were used to compare PRIM and aRTist. The first test case was a 320 mm outer diameter iron pipe with a wall thickness of 25 mm. The source to detector distance was 400 mm, with the pipe centred between source and detector. The detector had a side length of 409.6 mm, corresponding to 1024 pixels. A flat bottomed hole defect with diameter 25 mm and centre thickness 3 mm was added to the inner pipe wall. The source used was an x-ray source with a maximum energy of 1 MeV. The x-ray spectrum was calculated in aRTist and can be seen in Figure 3.20.

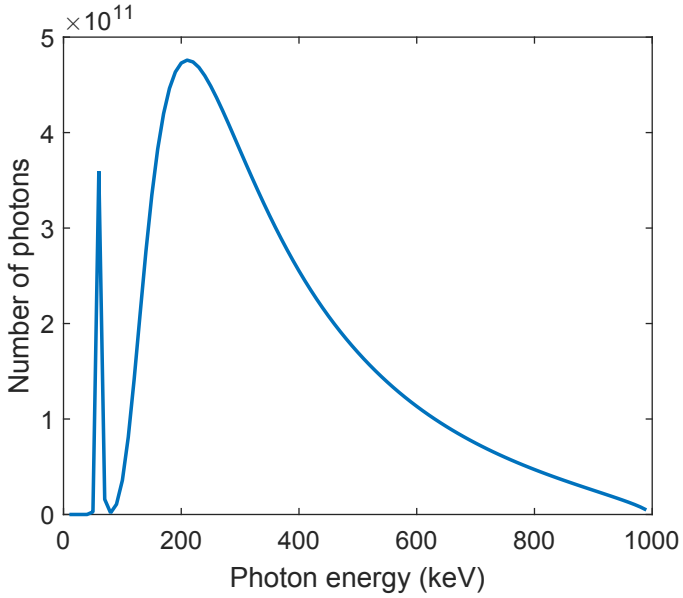

Figure 3.20: X-ray spectrum used in test setup of an iron pipe with a flat-bottomed hole defect. The spectrum was generated in aRTist and was used in both aRTist and PRIM simulations.

The total energy reaching the detector is shown in Figure 3.21, calculated using the Monte Carlo method in PRIM. A comparison of the analytical result in PRIM and aRTist is shown in Figure 3.22. The direct and scattered components of the Monte Carlo results are compared separately, and can be seen in Figures 3.23 and 3.24 respectively. In all cases good agreement is seen between the models.

A more complex case tested was of a water filled, insulated pipe. The

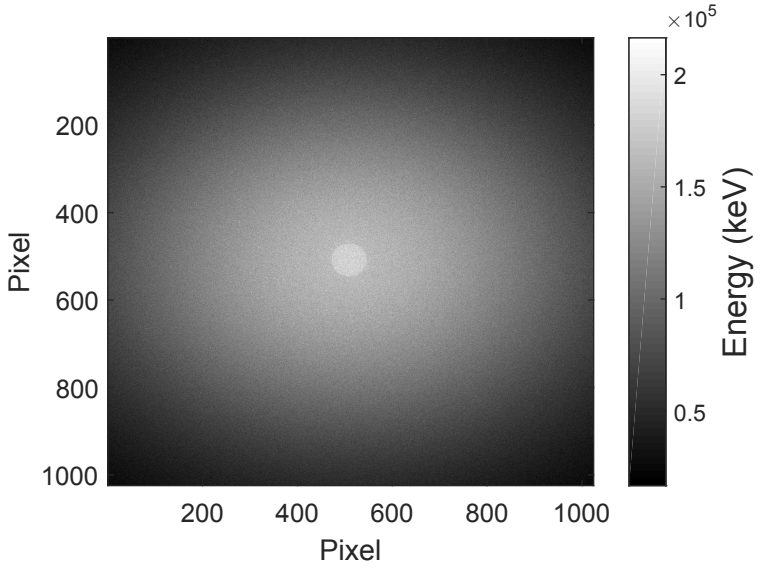

Figure 3.21: Total energy reaching the detector in PRIM for a 320 mm outer diameter pipe, with a flat bottomed hole defect. Calculated using the Monte Carlo method with 1×10^{10} photons.

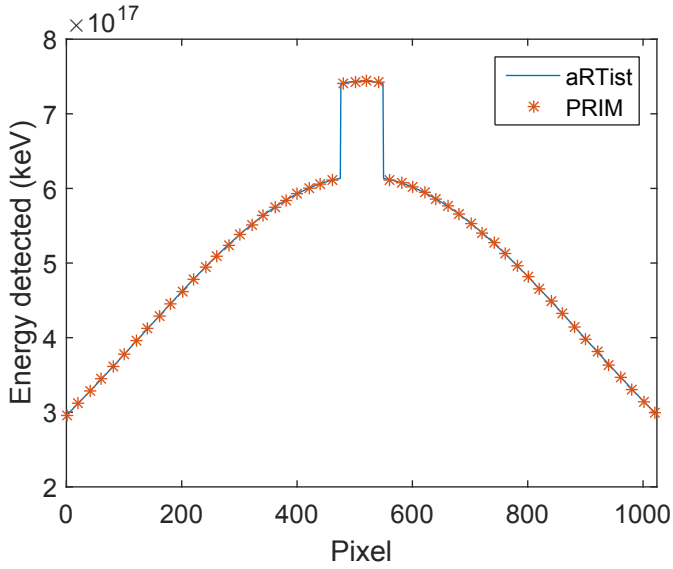

Figure 3.22: Comparison of analytically calculated direct radiation reaching the detector in aRTist and PRIM. The object was a 320 mm outer diameter pipe, with a flat bottomed hole defect. The plot shows cross-sections through the centre of the detector, at pixel 512.

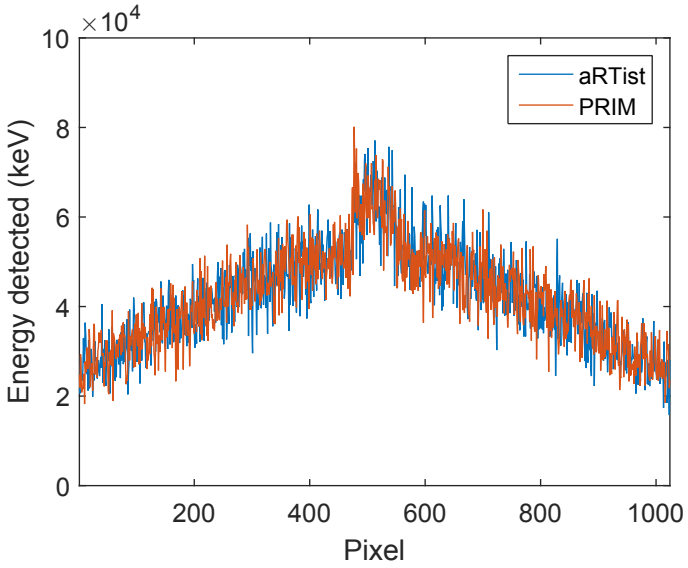

Figure 3.23: Comparison of direct radiation reaching the detector in aRTist and PRIM for a 320 mm outer diameter pipe, with a flat bottomed hole defect. The plot shows cross-sections through the centre of the detector, at pixel 512. Calculated from the Monte Carlo method in both cases.

simulated iron pipe had an outer diameter of 290 mm and wall thickness of 10 mm, and was covered with 15 mm thick plastic insulation. The pipe content was set to be water. A flat bottomed hole with 25 mm diameter and 3 mm centre depth, the same dimensions as in the previous test case, was included in the setup. The source used was a monoenergetic 1 MeV, while the detector had side length 409.6 mm and 1024 pixels. The Monte Carlo scattering simulation was run in both PRIM and aRTist, using 1×10^{10} photons in each case. The time taken to run the simulation in PRIM was 4.9 hours, while aRTist took 16.5 hours. Both were run on the same standard desktop computer, with eight cores and eight gigabytes of RAM. This illustrates the time saving achieved in PRIM through the use of analytical object shapes. The total energy reaching the detector, calculated using the Monte Carlo method in PRIM, is shown in Figure 3.25. As with the previous test case, aRTist and PRIM are compared by taking cross-sections through the resulting images. Examples of cross-sections through the direct radiation and scattered radiation components of the Monte Carlo result are shown in Figures 3.26 and 3.27 respectively. Again, good agreement is found.

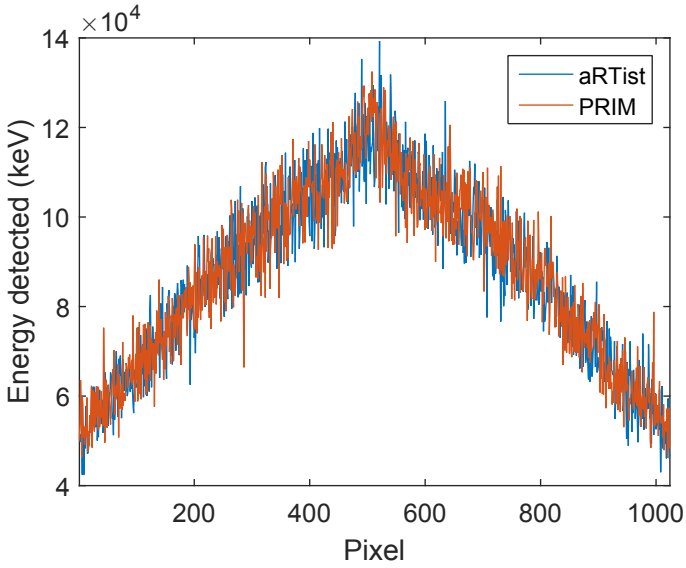

Figure 3.24: Comparison of scattered radiation reaching the detector in aRTist and PRIM for a 320 mm outer diameter pipe, with a flat bottomed hole defect. The plot shows cross-sections through the centre of the detector, at pixel 512. Calculated from the Monte Carlo method in both cases.

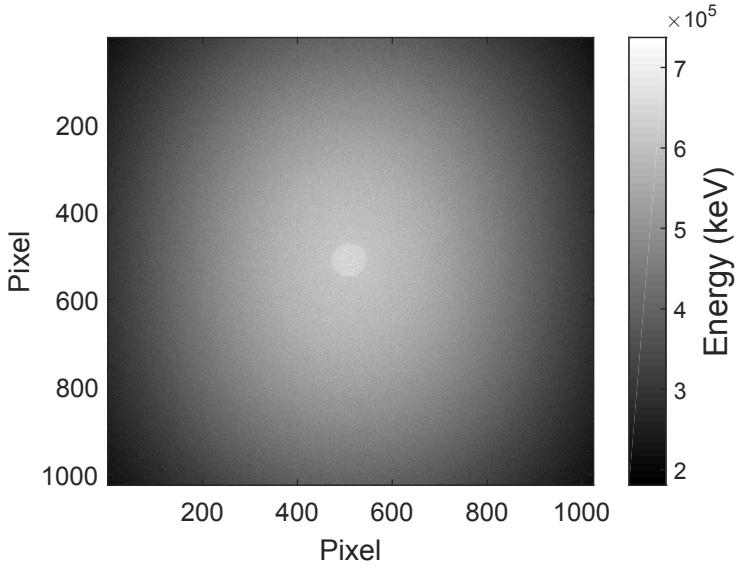

Figure 3.25: Total energy reaching the detector in PRIM for a water filled, insulated pipe with a flat bottomed hole defect. Calculated using the Monte Carlo method with 1×10^{10} photons.

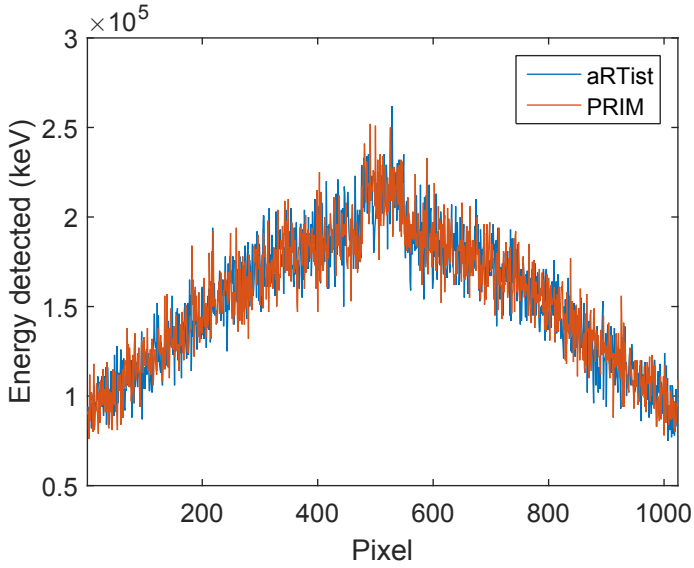

Figure 3.26: Comparison of direct radiation reaching the detector in aRTist and PRIM for a water filled, insulated pipe with a flat bottomed hole defect. The plot shows cross-sections through the centre of the detector, at pixel 512. Calculated from the Monte Carlo method in both cases.

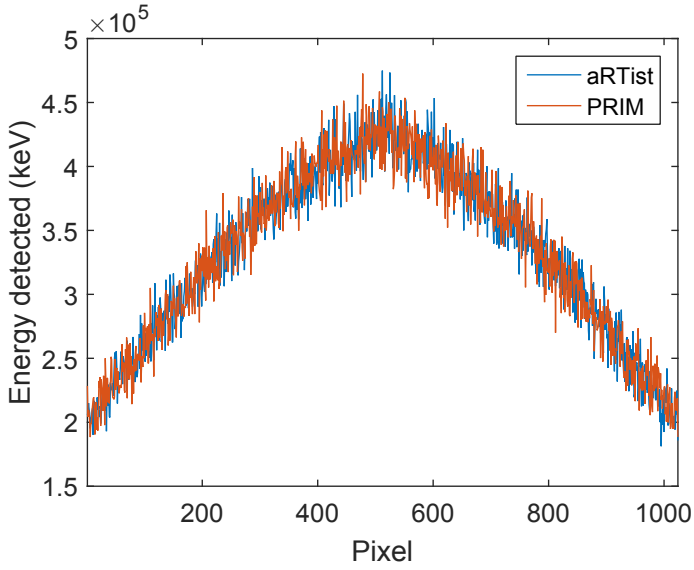

Figure 3.27: Comparison of scattered radiation reaching the detector in aRTist and PRIM. Results are for the same case as in Figure 3.26.

3.5 Summary

In this chapter the development of a radiographic simulation model has been described. The model, PRIM (Pipeline-specific Radiographic Inspection Model), is optimised for modelling of pipeline inspection configurations. The aim of the development was to provide a simple, fast alternative to commercially available models. In addition, the aim was to aid in understanding of the simulation methods used in models such as aRTist and CIVA; thus ensuring these models could be used accurately and efficiently in later project work.

PRIM uses a combination of an analytical calculation of direct radiation, and a Monte Carlo simulation for scattered radiation. This is the same approach as used in CIVA and aRTist. Both the analytical and Monte Carlo components of the model have been compared against CIVA and aRTist for validation. Test cases range from simple blocks of iron up to an insulated, water filled pipe containing a flat bottomed hole defect. In all cases good agreement was found between the models.

Subsea radiography makes use of high energy sources, such as a 7.5 MeV betatron. This means that PRIM could not be used to accurately replicate experimental subsea setups, due to not modelling pair production or including a realistic detector model. A suitable model for high energies is aRTist, as it includes pair production in addition to second order effects of photon interactions, such as electron transport. Therefore aRTist has been used for much of the project. However PRIM has continued to be useful, for example to provide images when developing the defect characterisation method described in Chapter 5.

4 Simulation Validation

4.1 Introduction

One of the initial aims of this project was to examine different methods of pipeline corrosion imaging in a subsea environment, analysing the impact of water and identifying the most effective setups. Ideally this would be done with experimental data, but sufficient data for research could not be obtained due to the cost and complexity of subsea inspections. An alternative is to use simulations, which are significantly more affordable and accessible than subsea experimental data, and are able to model a wide range of underwater radiographic setups. However, simulation models have not been fully validated as accurate for high energy underwater imaging, and before conclusions can be drawn from simulation results they must be shown to be comparable to experimental measurements. In particular, since we are interested in how image quality changes with water thickness, the image quality in an experimental image needs to be accurately reproduced in the simulation.

There are numerous studies comparing simulated radiographs to experimental images, and several focussing on analysing subsea pipeline radiography. However, most use different equipment or setup geometries to those of interest here, or do not include analysis of image quality parameters. A set of work with aims closely aligned to this project is covered in several papers: Souza et al. (2008, 2011, 2014) [85, 86, 87] and Correa et al. (2009) [88]. These detail comparisons between simulated and experimental radiographs, followed by the use of the simulation to investigate scattering in subsea pipeline imaging. The authors make use of the Monte Carlo N-Particle (MCNPX) code [89] developed at the Los Alamos National Laboratory [90]. MCNPX is a versatile code for particle transport simulation, and can be used for photon, electron and neutron transport. As it is not specifically aimed at radiographic image modelling it does not in-

clude features such as radiographic detector responses, and results must be post-processed to convert into standard 16-bit digital radiographic images [85].

Using MCNPX, the authors model a DWSI inspection setup with an Iridium-192 source and a computed radiography detector. As the CR detector is flexible it is curved around the pipe, giving a different inspection geometry to that of interest in this project. In addition the authors do not measure or compare image quality parameters such as SNR, CNR and SR_b in experimental and simulated images. Souza et al. (2008) [85] finds good agreement in overall trends between experiment and simulation, but there is visibly significantly more noise in the experimental images, which is not measured or analysed. Correa et al. (2009) [88] uses MCNPX to estimate weld thickness loss in subsea pipelines; however only grey level ratios are compared with experimental images. Souza et al. (2011, 2014) [86, 87] focus on analysing the impact of scatter on radiography of subsea pipelines. This is done purely through simulation in MCNPX, and results are given as a percentage scatter contribution for images with different setup parameters. While this is a useful measure, it is difficult to translate it into defect detectability or IQI visibility, which would give more information on the implications for inspections.

Other papers tend to focus on validation of particular simulation models or using specific setups and equipment. Tisseur et al. (2016) [91] describes the validation of CIVA for a high energy linear accelerator source. The validation is done through comparison with experimental images of a cylindrical steel casting using film as the detector, which is curved around the object. The results show good agreement between simulation and experiment. There is some error, which the authors put down to differences in the source, as the manufacturers did not release all the data required to simulate it. Another recent study, Kolkoori et al. (2016) [92] looks at the influence of scattering on dual energy x-ray imaging. A high energy betatron source is used, with simulation and experiment compared and good agreement found. Again a small error, about 1% deviation, is identified, with the authors suggesting a shift in the maximum beam intensity of the betatron as the cause.

Despite this range of research there has not been a study which definitively demonstrates the accuracy of a simulation model for high energy

underwater imaging. In this chapter I present an investigation into simulation model accuracy using the setup and equipment relevant for high energy subsea pipeline imaging. To do this I obtained a set of experimental radiographs of a well characterised pipe in water and simulated the same setups in the simulation tool aRTist [71]. The experimental data was used to adjust aRTist parameters with the aim of matching simulated to experimental radiographs. In particular, image quality parameters such as signal-to-noise ratio, contrast and basic spatial resolution were compared. With this method signal-to-noise ratio was successfully matched, while differences were still found in contrast-to-noise ratio comparisons. This means that measurements depending on absolute intensity are not accurate enough. However wall thickness measurements in tangential images, which are not based on absolute intensity, were found to produce similar results in simulated and experimental cases.

The differences in contrast and intensity are thought to be due to detector backscatter and additional scatter from out-of-setup objects within the exposure bay, due to a lack of source collimation. These would affect the experimental results but were not included in the simulated setup. This was investigated by including different proportions of peripheral water and other objects in the modelled setup and examining the effect on image quality parameters. Results show that additional scatter has a significant impact on the radiograph, particularly on image contrast, and is therefore the probable cause of differences between experimental and simulated images. This implies that it will be very difficult to completely match simulated to experimental results, as including all possible scattering objects in the model would be very complex. An improvement could be made by using real subsea data to estimate this additional scattering, which could then be used to calibrate the model. However there would still be significant uncertainties, for example due to lack of knowledge of what objects may be adjacent to any given subsea setup. This means there would still be uncertainty in the ability of the model to accurately produce realistic intensity and contrast.

As well as the uncertainties in modelling accuracy due to scattering, there is also the possibility that the source spectrum is incorrectly modelled. With today's technology it is not possible to measure the spectrum of a high energy, pulsed source such as a betatron; spectra used in modelling are calculated through Monte-Carlo simulations. So a contributor to the difference

between experimental and simulated results could be that the source spectra are not the same. Another issue is that there is an angular variation of the source flux and spectra in real sources. Current commercial codes do not take all these effects into account, giving more potential causes of error.

This set of work was performed in collaboration with the Institute of Materials Testing (BAM) in Berlin, where I spent time working in order to collect experimental data. The chapter is based on a journal paper which has been published in NDT&E International [9]. Experimental and simulation methods are explained in the next sections, followed by methods of tuning the simulation to match image quality parameters.

4.2 Experimental Method

Experiments were performed in the high-energy X-ray laboratory at BAM. The pipe used for testing and the experimental setup are shown in Figures 4.1 and 4.2 respectively. The sample, Fig 4.1, was a stepped pipe with an outer diameter of 322.6 mm and wall thickness from 8.5 mm to 25 mm. The pipe also has three sets of internal flat bottomed holes with depths of 10%, 20% and 50% wall thickness. The experimental setup, Fig 4.2, used a pulsed betatron with a maximum energy of 7.5 MeV [93] and a digital detector array. The detector (Perkin Elmer XRD 1621 model [94]) has a sensitive area of 409.6 mm x 409.6 mm with 2048 x 2048 pixels and a pixel size of 200 μm. To provide a higher signal-to-noise ratio the detector was used in pixel binning mode. This is where the image pixel is calculated from the sum of four detector pixels, resulting in an image with 1024 x 1024 pixels of 400 μm.

A source to detector distance of 1650 mm was used, with a pipe centre to detector distance of 504 mm as shown in Figure 4.3. Due to equipment constraints it was not possible to move the source or detector closer to the pipe, as required for the double wall single image method. Instead images were taken with the double wall double image and tangential methods. All images were taken with the same exposure time of 2 s per frame and the same calibration, using a 100 frame gain image and a 20 frame offset image. Copper filters (1 mm thickness) were used at the source and/or detector in some images to improve image quality.

To add water to the setup the pipe was placed in the centre of a rectan-

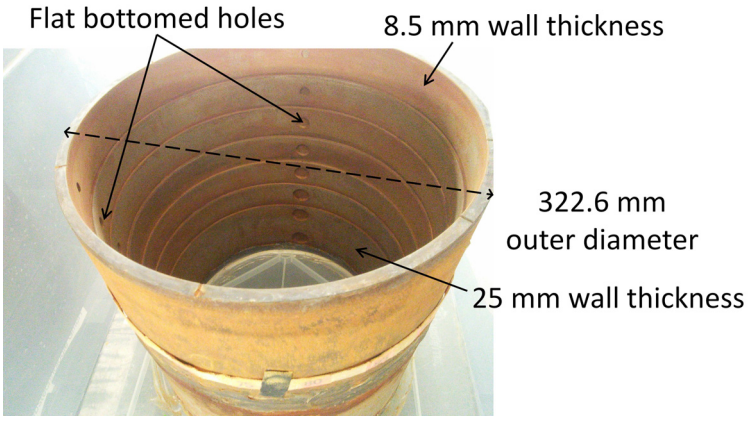

Figure 4.1: Stepped pipe used as test object.

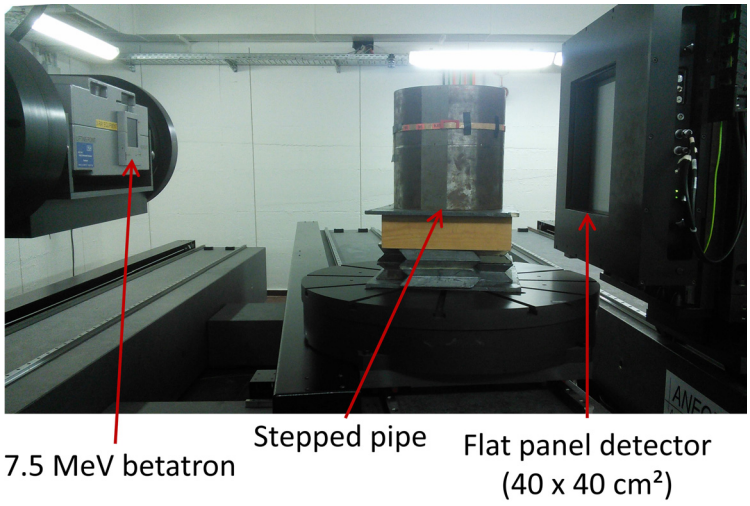

Figure 4.2: Setup for high energy radiography of the pipe.

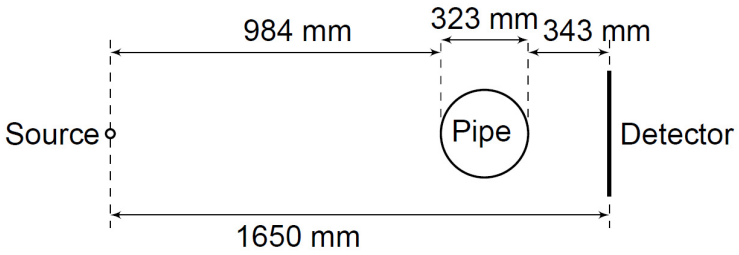

Figure 4.3: Setup dimensions used for experimental image acquisition.

gular plastic water tank. This allowed for setups with two different water thicknesses to be imaged by rotating the water tank, as illustrated in Figure 4.4. Silicone sealant was used to create a seal around the base of the pipe allowing for images to be taken with water around the pipe but air inside, in addition to those with water both inside and outside the pipe.

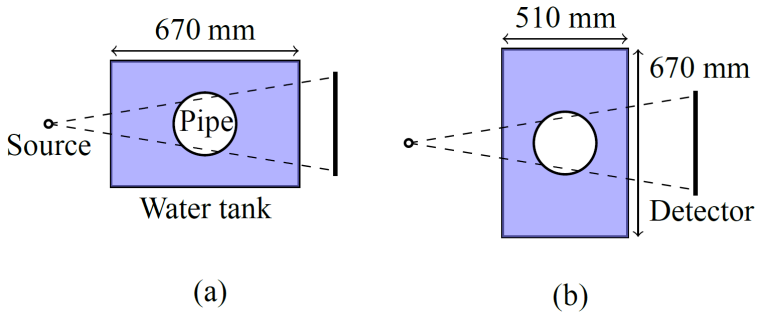

Figure 4.4: The stepped pipe was placed in a rectangular water tank, (a) & (b) show two setups with different water thicknesses made possible by rotating the water tank.

4.3 Simulation Method

The same setups as used experimentally were simulated in aRTist, a simulation tool developed by BAM. A visualisation of the simulation setup is shown in Figure 4.5.

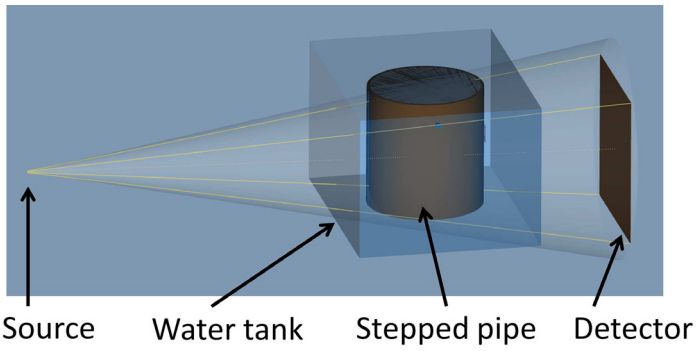

Figure 4.5: Radiographic setup modelled in aRTist. Dimensions and distances used were as in experimental setups.

Further details on aRTist can be found in Bellon et al. (2012) [95] and Jaenisch et al. (2011) [96]. The detector was modelled using a new Detec-

tor Calculator module [97] which uses data from an experimental reference image to characterise the detector, while the betatron source was modelled with the spectrum calculator incorporated into aRTist [98]. The source spectrum is plotted in Figure 4.6. Although the maximum energy of the betatron is 7.5 MeV the majority of the photons produced are at much lower energies. This makes simulation of photon scattering very important as Compton scattering is the dominant photon interaction for most of the betatron energy range. aRTist makes use of a Monte Carlo technique to model scatter, combined with an analytical straight-line calculation of direct radiation.

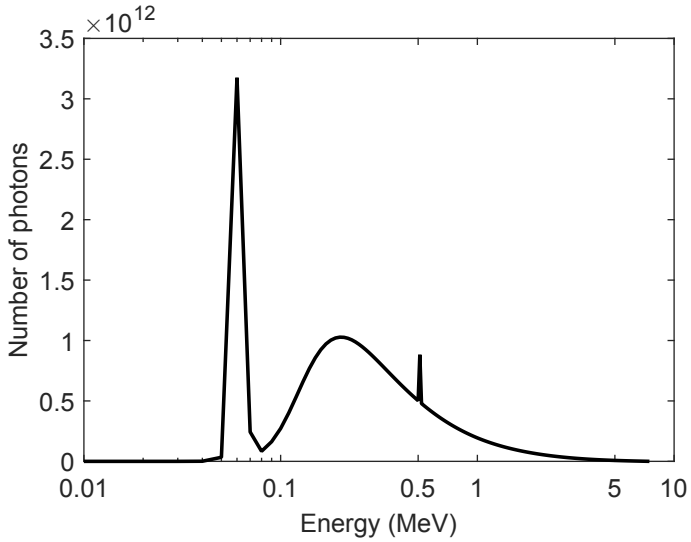

Figure 4.6: Spectrum of the 7.5 MeV betatron as modelled in aRTist.

4.4 Simulation Tuning

The simulation was adjusted with the aim of matching the main image quality parameters to those measured experimentally. These include Signal-to-Noise ratio (SNR), Contrast-to-Noise ratio (CNR) and basic spatial resolution ($SR_b^{detector}$). Chapter 2 described the method of measuring these parameters according to the standards [3, 4]. However, some additional steps were required in practice. A key requirement for measuring the standard deviation or signal-to-noise ratio in a section of an image is that there should be no overall trend in grey level in the area of measurement. It

was found that almost every region of the images had a significant trend in grey level, meaning a standard deviation calculation would overestimate the noise. Therefore a pre-processing step was used in which, for each line of pixels to be included in a measurement, a best-fit polynomial line was calculated. This line was used as a baseline to remove the grey level trend, with the mean value of the pixel line kept the same. This procedure effectively compensated for the problem of grey level trends in the images, and ensured calculated SNR and noise levels in different images were comparable.

In addition to matching the main image quality parameters, the profile across the edge of the pipe in tangential images was also taken and compared in simulated and experimental cases. Taking a line profile across the radiograph, the edge profile is a portion of this in which the edge of the pipe is visible, as visualised in Figure 4.8(a). Figure 4.8(b) shows the grey value (intensity) versus pixel plot for this portion of the radiograph, where the pixel refers to the detector pixel number and is equivalent to a distance along the radiograph. The main parameter affecting the shape of the profile is unsharpness. Images with low unsharpness have clearer, better defined edges, while those with high unsharpness have smoother edges and lower contrast. Unsharpness has been shown to be a superposition of a short range effect and a long range effect [99]. The short range unsharpness can be seen by measuring the slope of an edge profile, while the long range component manifests as the extended rounded spurs to either side of the edge. The difference between long and short range unsharpness is illustrated in Figure 4.7.

In aRTist the long range unsharpness can be varied directly, while the 'unsharpness ratio' parameter sets the relative proportions of long and short range unsharpness. Results of simulations with example values of low, medium and high unsharpness are plotted to illustrate the effects of these parameters, along with the experimental profile. The unsharpness parameters were varied to get a similarly shaped profile to experimental results.

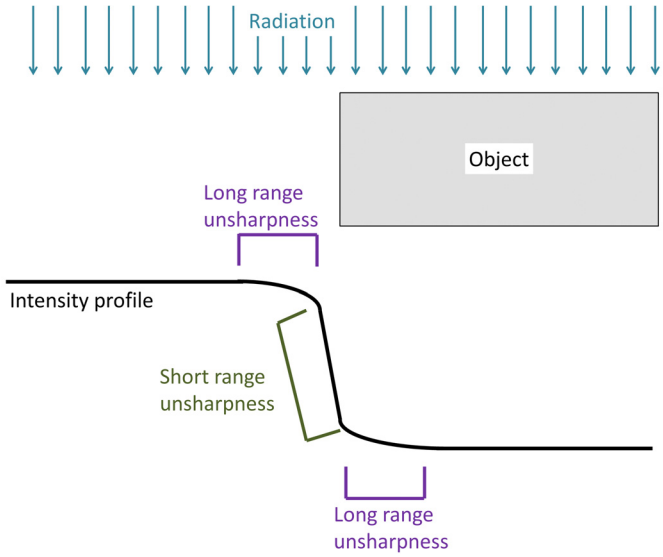

Figure 4.7: Diagram illustrating long and short range unsharpness.

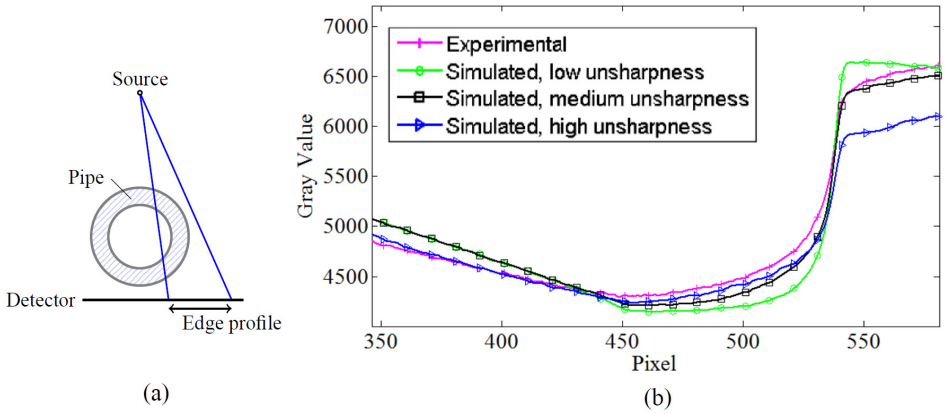

Figure 4.8: (a) Diagram illustrating the edge profile, a portion of the line profile across the radiograph in which the edge of the pipe is visible, (b) The edge profiles of experimental and simulated images are plotted. The minimum intensity seen at pixel 451 identifies the inner pipe wall position, while the outer pipe wall is at the point at pixel 542 where the rate of increase in intensity suddenly stops or slows significantly.

4.5 Results

An example of an experimental tangential radiograph with points of interest highlighted is shown in Figure 4.9.

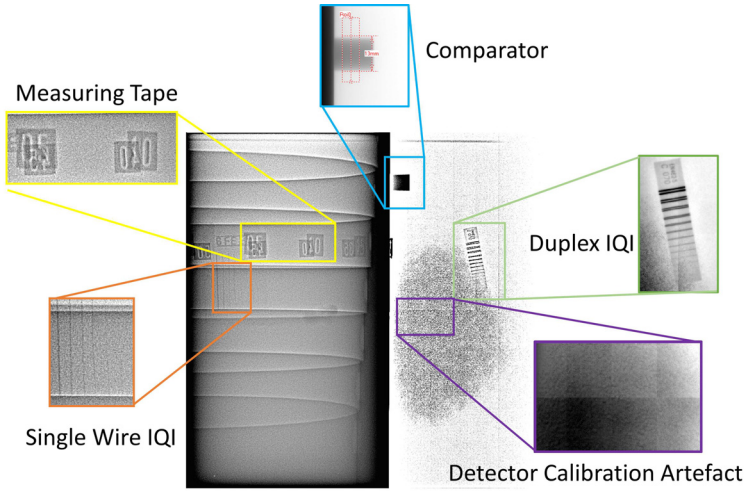

Figure 4.9: An example of an experimental tangential radiograph. It has been filtered for better visualisation and points of interest are highlighted. A 13 mm comparator was fixed to the edge of the pipe to calibrate dimensions in the image. A measuring tape with lead numbers was wrapped around the pipe. A single wire IQI was placed on the outer pipe wall, on the side nearest the detector while a duplex wire IQI was placed on the detector in the free beam area of the image. Although a detector calibration was applied there are still some step-like artefacts visible in the free beam area of some of the images.

Edge profiles across simulated and experimental images were taken and compared. These profiles include the edge of the pipe and a distance to either side. Figure 4.10 shows simulated and experimental profiles for (a) the setup with no water either inside or outside the pipe, and (b) the setup with water outside the pipe but not inside.

Examining these profiles it can be seen that there is an offset in intensity in some areas. The differences in simulated and experimental intensity values means that the contrast-based measurements of double wall imaging in simulated images will not match the same measurement in experimental images. However, tangential imaging does not depend on the particular intensity values but on the positions of the inner and outer pipe wall given by the minimum intensity (inner wall) and the point where the sharply increasing intensity stops or slows significantly (outer wall). From the profiles in Fig 4.10 it can be seen that these pipe wall positions are fairly accurately

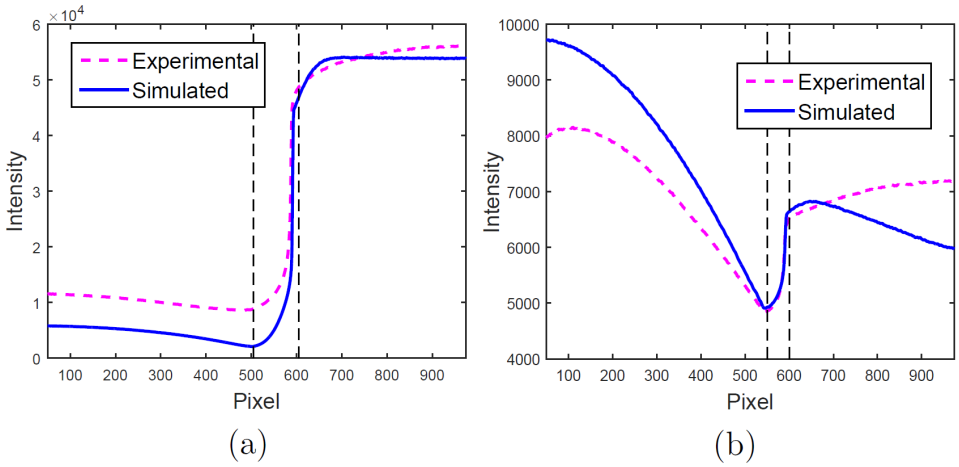

Figure 4.10: Profiles across the radiograph for experimental and simulated images in the cases of (a) No water, (b) With water outside the pipe but not inside. For each image the dashed black line indicates the positions of the inner and outer pipe walls.

reproduced in the simulated results, meaning tangential measurements may be equivalent to experimental results.

To test this, wall thickness measurements were taken of the thickest, 25 mm, pipe wall in a set of images. Results are shown in Figure 4.11 for one simulated and experimental image in each of the five setups used: those with water both inside and outside the pipe and with either the longer, 670 mm, or shorter, 510 mm, water tank thickness, those with water just outside the pipe and with the 670 mm or 510 mm thickness and finally those with no water. All measurements are within ±0.8 mm of the actual value, and although the simulated results tend to be lower than experimental ones this difference is fairly small. Analysis of more images is needed but an initial conclusion is that the simulation produces results comparable to experimental ones for tangential measurements.

Contrast-to-noise and signal-to-noise ratios were also measured and compared in experimental and simulated images. CNR was measured across several pipe wall thickness steps in each radiograph and results averaged to get a single value to compare for each image. While there is a trend in CNR with wall thickness within each image there is also an overall trend between images. Comparing just a single step measurement has more inaccuracy as it is only a single measurement for each image. Since we are interested in

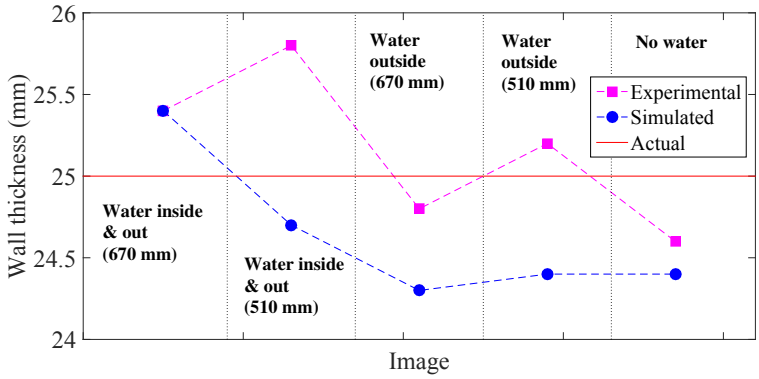

Figure 4.11: Wall thickness measurements of the 25 mm pipe wall in tangential experimental and simulated images for the five different setups used.

the differences between images rather than actual CNR values then averaging reduces the noise and shows the trend between images more clearly. Using the same measurement points in each image ensures comparability of the resulting CNR. Figure 4.12 shows the CNR for images in all five setup types. Images are numbered with 1 – 5 referring to the setup type, while a – d refers to the copper filter used, as labelled in the figure.

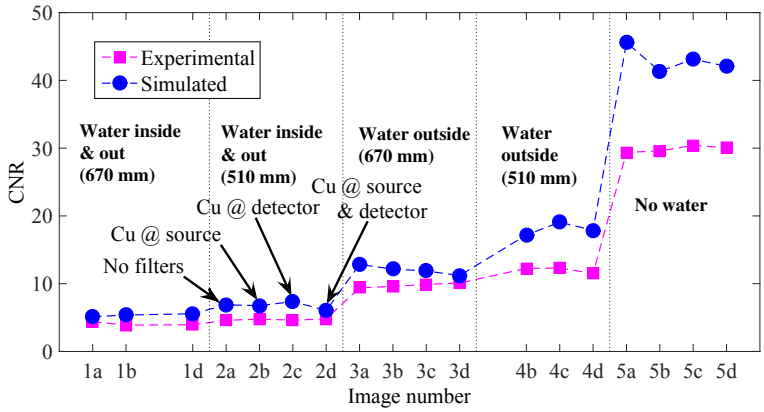

Figure 4.12: Contrast-to-noise ratio for a series of simulated and experimental images in the five different setup types. The images were all taken with 100 frames. Copper filters were used in some images, labelled a – d where a = no filter, b = 1 mm copper at the source, c = 1 mm copper at detector and d = 2 mm copper in total with 1 mm at both source and detector.

From Fig 4.12 it can be seen that the simulated CNR values are higher than the experimental ones. This is the same problem as seen in the profile comparisons. However, although the CNR values differ, the same overall trend of increasing CNR with decreasing water thickness seen experimentally is reproduced in the simulation results. This demonstrates that the model takes into account the effects of water and correctly responds to changes in water thickness.

SNR was also measured, near to the CNR measurement points, and similarly averaged. Results are shown in Figure 4.13. In the case of SNR both the absolute values and overall increasing trend of experimental measurements are reproduced in the simulated results. This is an encouraging result as the frame number used in the simulations, which directly affects SNR, was tuned using experimental images from only one setup type. All simulated images were then taken with the same frame number, with the agreement in trend again demonstrating that the effects of water are being taken into account correctly by the model.

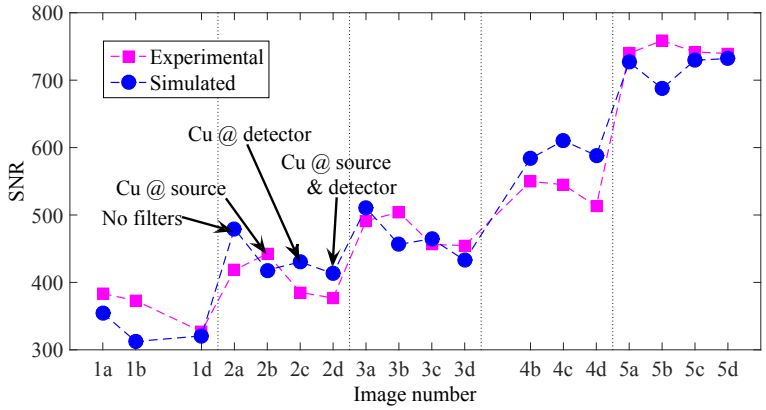

Figure 4.13: Signal to noise ratio for the same set of images as in Fig 4.12.

4.6 Peripheral Scatter

The simulated setup, while including all objects in the direct source-detector path, does not account for scattering from out-of-setup objects that would have occurred experimentally. Peripheral scattering refers to the case in which a photon is emitted off to the side of the object being imaged, in this case the stepped pipe, and then undergoes one or more

scattering interactions with other objects in the exposure bay. With each scattering event the photon's direction may be changed, which could result in the photon reaching the detector after one or more peripheral interactions. No source collimation was used either in the experimental or simulation methods, meaning photons will have been emitted over a wide angular range. The next section describes simulation setups used to investigate how significant this additional scattering is, followed by results.

4.6.1 Simulation method

It is too complex to model the entire experimental area, but an idea of how big an impact this type of scattering has was obtained by increasing the height and length of the modelled water tank as shown in Figure 4.14. Images with a range of water tank sizes were simulated, with the tank depth kept constant such that the straight line path from the source to any detector pixel was the same for all images. All images were simulated with an air-filled pipe and a fixed source opening angle.

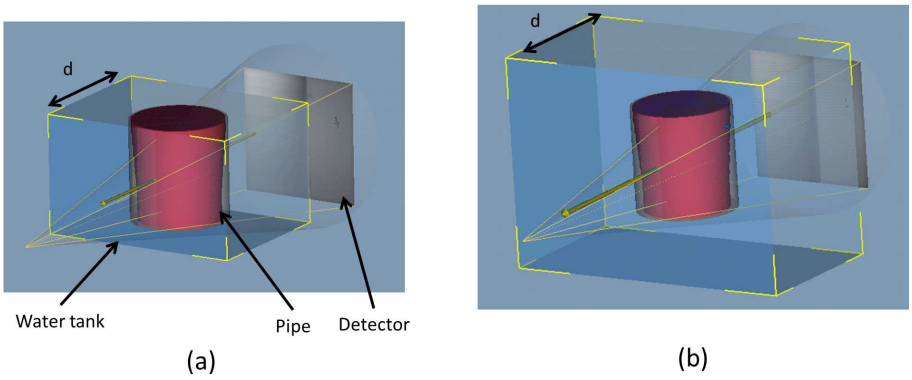

Figure 4.14: Radiographic setup modelled in aRTist for peripheral scatter study, (a) Original setup matching experimental dimensions, (b) With water tank height and length increased. Tank depth, d, is kept constant meaning the thickness of water in the source-detector line is as in the experimental setup. The impact of scattering from the additional peripheral water can be examined by comparing images with different sized water tanks.

A more realistic setup including simulated surroundings was also modelled, as shown in Figure 4.15. In this case objects similar to those in the experimental surroundings were placed in the model. Two scattering

regimes were tested by setting the model surroundings first as low scattering iron and then as higher scattering water. No water tank was used and the pipe was air-filled, making these images comparable to the experimental setup with no water present.

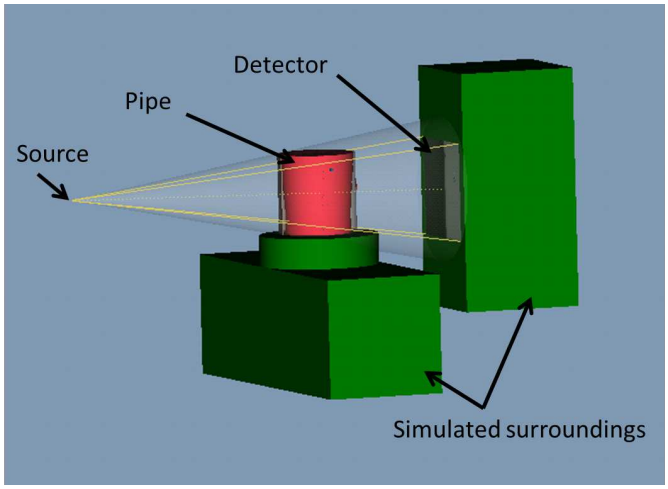

Figure 4.15: Radiographic setup modelled in aRTist including some nearby, peripheral objects similar to actual surroundings in the experimental setup. The material of the additional objects was set to be either iron or water, as examples of a weakly and a strongly scattering material.

Simulation parameters were kept as previously set, however exposure time was varied between images. This was in order to keep the maximum grey level constant as images receiving higher scattering have higher grey levels making direct comparisons difficult.

4.6.2 Results

Profiles across an experimental tangential radiograph and simulated results for water tanks varying in size are shown in Figure 4.16. The water tank size was varied from the original 670 mm length and 400 mm height up to a maximum of 1150 mm length and 880 mm height, corresponding to an additional 480 mm in each dimension. The increased size of the water tank is seen to have a significant impact on the profile with the contrast and definition of the pipe wall very much reduced for the larger water tanks. This is due to the additional scattering reaching the detector in these cases,

as the source to detector direct path remains unchanged.

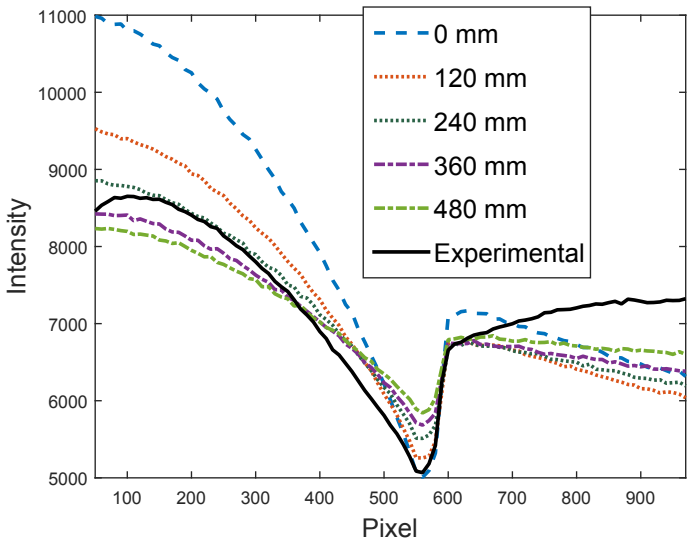

Figure 4.16: Profiles across the radiograph for experimental and simulated tangential images with increased water tank lateral dimensions. Numerical values in the legend indicate the increase in water tank size, with 0 mm as the original 670 × 400 mm tank and 120 mm as an increase to a 790 × 520 mm tank, etc.

Contrast-to-noise ratio was also measured for each image. The method of CNR measurement is as previously described, with measurements taken across seven wall thickness steps in an image. The measurements were then averaged, giving a mean CNR value for each image. Mean CNR as well as CNR measured across three of the steps is shown in Figure 4.17 for a series of images with different water tank sizes. Simulated images are labelled from 0 to 12 and have a difference of 40 mm in water tank height and length between them, ranging from the original 670 × 400 mm tank, labelled 0, up to the 1150 × 880 mm tank, labelled 12.

From Fig 4.17 it can be seen that increasing the water tank size causes a sharp decrease in contrast for the first few 40 mm increases (images 0 to 4). These differences begin to tail off, becoming insignificant around image 8, corresponding to a water tank size of 990 × 720 mm. This is consistent with expected behaviour of out-of-beam scattering objects as additional water close to the beam will have a larger effect than that further away.

The mean signal-to-noise ratio for the same set of images is shown in Fig-

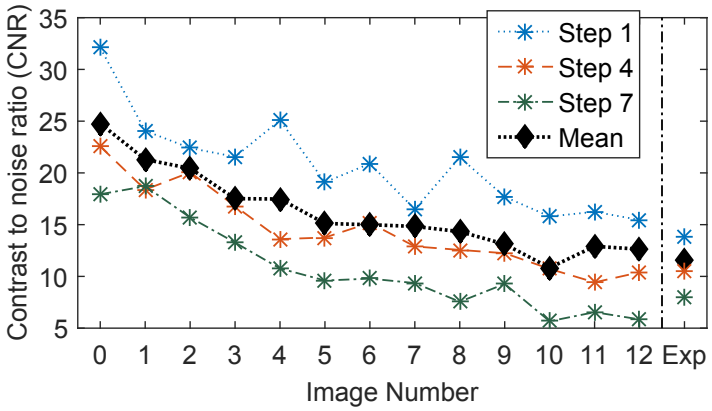

Figure 4.17: Contrast-to-noise ratio for images with different sized water tanks. Simulated images are numbered from 0 to 12 in order of increasing water tank size, with increases in 40 mm steps. Mean CNR is the mean of seven measurements for each image, three of which are also shown as Steps 1, 4 and 7. Step 1 is a measurement taken near the thinner, top area of the pipe, step 4 is near the centre and step 7 is near the thickest, lower portion of the pipe.

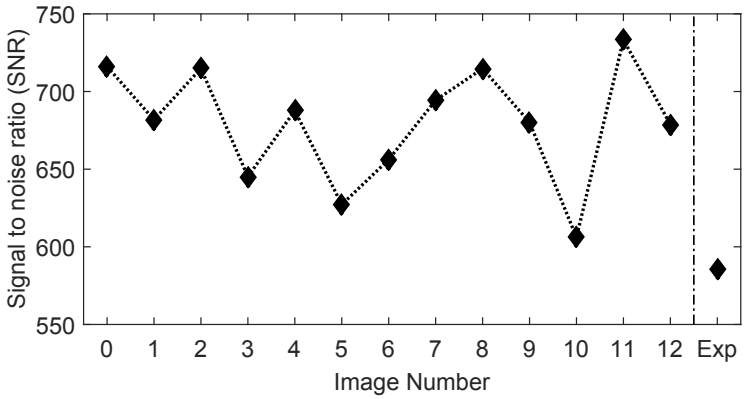

Figure 4.18: Mean signal-to-noise ratio for images with different sized water tanks. Images are labelled and ordered as in Fig 4.17. In this case only the mean value is plotted, calculated as the average of measurements near each of the seven steps.

ure 4.18. The simulation was not directly calibrated with the experimental image in this case, and exposure times were varied to get better matching grey levels, hence SNR has no clear trends and shows the simulated results to be much higher than experimental. To ensure differences in noise were

not responsible for the observed change in CNR the relative contrast (Cr) was also measured, shown in Figure 4.19. With some minor differences the relative contrast produces the same trend as CNR.

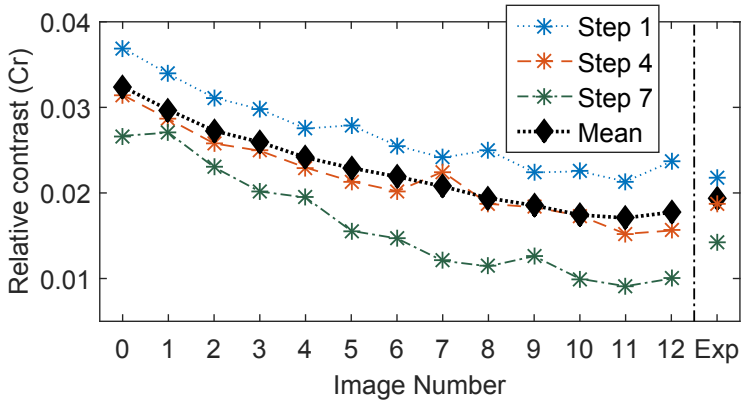

Figure 4.19: Relative contrast for images with different sized water tanks. Images are labelled and ordered as in Fig 4.17.

The same comparisons were also performed for the images without water inside or around the pipe, but with simulated surroundings as in Fig 4.15. In this case four images were compared: one experimental, the original simulated image without surroundings, a simulated image with iron (Fe) surroundings and a simulated image with water surroundings. Profiles of these four images are shown in Figure 4.20. Again, the change caused by additional peripheral scattering is significant. The case of iron surroundings results in a slight decrease in contrast from the original. Iron is relatively weakly scattering so this is as expected. For the stronger scattering water the change is much greater, with the inner pipe wall barely identifiable in the profile.

Contrast-to-noise ratio for the four images is shown in Figure 4.21. CNR with additional scattering is much lower compared to the original simulated image, with experimental CNR higher than the simulated water case but lower than simulated iron, indicating an actual rate of additional scattering between the two. To check that results are not due to differences in noise the relative contrast is shown in Figure 4.22. Relative contrast can be seen to produce the same trend, confirming this result.

To examine how different energies within the betatron spectrum contribute to peripheral scattering, simulations were also run with monoen-

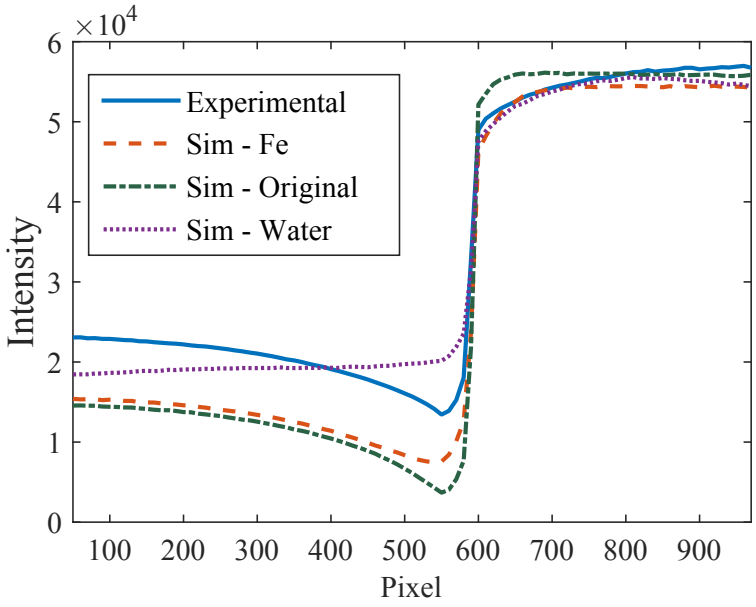

Figure 4.20: Profiles across the radiograph for experimental and simulated images with no water in the beam path. Three simulated images are shown, one with no peripheral objects, one with iron surroundings and one with water surroundings both simulated using the setup shown in Fig 4.15.

ergetic sources. Two energies were chosen; 300 keV and 2 MeV. 300 keV was used because it is near the peak in photons produced by the betatron in the 100 keV to 1 MeV range as shown in Fig 4.6. 2 MeV was used as an example of a high energy (over 1 MeV) in the betatron spectrum. The setup in Fig 4.15 was used as the test setup. Four simulations were run; two with each monoenergetic source, of which one included water surroundings while the other had no additional scattering objects. For each image the scatter-to-primary ratio, SP, was calculated at every pixel. SP is given by:

$$SP = \frac{I_S}{I_P} \tag{4.1}$$

where I_S is the intensity of scattered radiation and I_P the intensity of primary radiation. It is customary to express scatter contribution in terms of build-up factor, which is defined as $1 + SP$. However in this case using SP directly gives more insight. In order to compare the difference in scattering between the two source energies a relative scatter-to-primary ratio for each

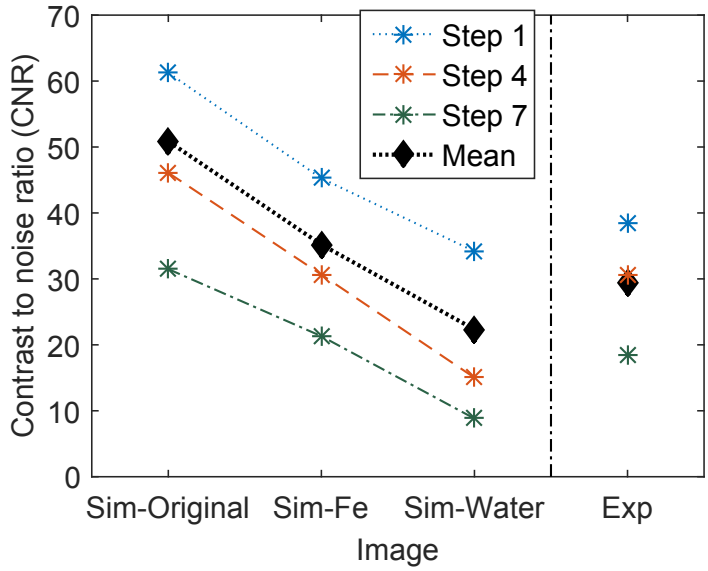

Figure 4.21: Contrast-to-noise ratio for images with different peripheral objects. Sim-Original has no additional objects, while Sim-Fe and Sim-Water have simulated surroundings made of iron and water respectively.

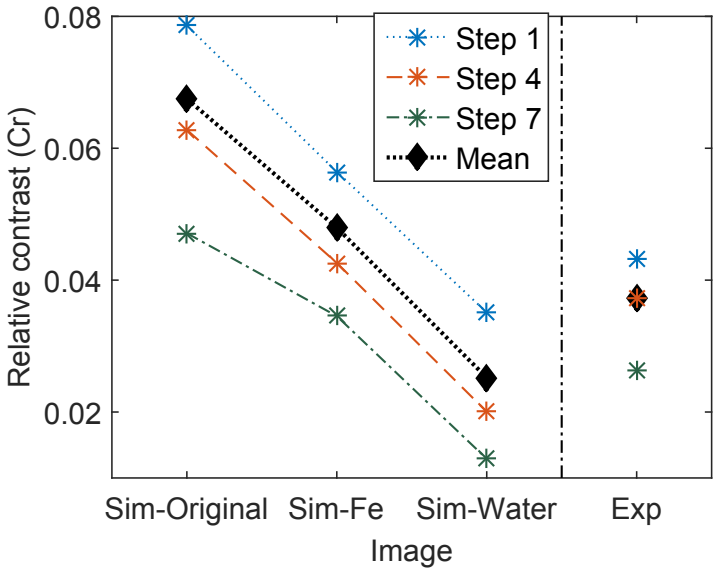

Figure 4.22: Relative contrast for images with different peripheral objects, as in Fig 4.21.

source was calculated. The relative scatter-to-primary ratio, S_{Rel}, demonstrates the change in scatter ratio caused by the water surroundings and is calculated from:

$$S_{Rel} = \frac{SP_{water}}{SP_{none}} \tag{4.2}$$

where SP_{water} is the scatter-to-primary ratio in the image with water surroundings and SP_{none} is the scatter-to-primary ratio in the image without additional surroundings. The relative scatter ratio for each image pixel is calculated, however for ease of comparison a cross section down the image, in the free beam area, was taken.

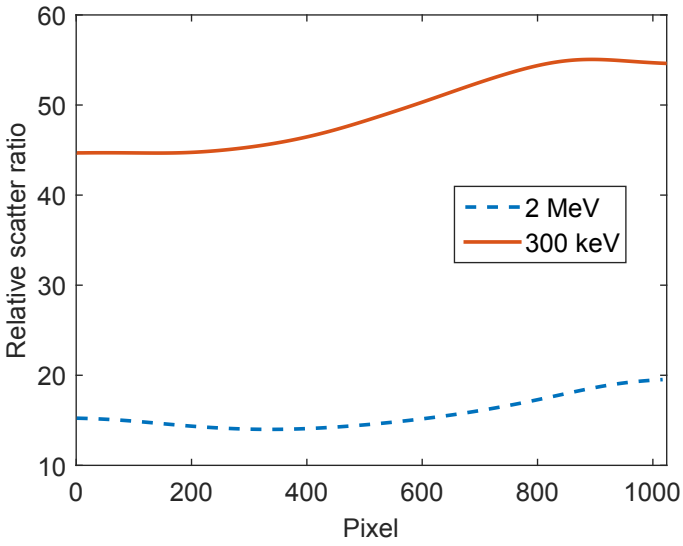

Figure 4.23: Relative scatter ratios for the cases of monoenergetic 300 keV and 2 MeV sources. The plotted section is a cross section down the image in the free beam area. Pixel 1 is at the top of the image while pixel 1024 is the lowest pixel. The increasing trend from pixel 1 to pixel 1024 is due to the additional scattering objects being placed under the pipe, giving higher scattering in the lower portion to the detector. The difference between the 300 keV and 2 MeV cases demonstrates that the lower energy is impacted by peripheral scattering to a much greater extent.

The relative scatter ratio, S_{Rel}, for each source is plotted in Figure 4.23. This shows that the relative scatter ratio is much greater for the 300 keV source than the 2 MeV source. The implication is that peripheral scattering has a much more significant effect on low to medium energy photons. This

is consistent with the attenuation coefficients plotted in Fig 2.1, showing total attenuation to decrease with energy until much higher, tens of MeV, energies. A more in depth analysis of scattered radiation could be achieved by calculating the energy spectra; for example to compare the initial spectrum with that reaching the detector. This could form the basis of valuable future work.

4.7 Discussion

Results from the original simulation-experiment comparison (Section 4.5) show differences between the two, particularly in image contrast. However, the simulation did not account for the additional scatter from other objects in the exposure bay which would have happened experimentally. This scatter was initially assumed to be negligible, however when investigated in aRTist (Section 4.6) it was found to have significant effects on the image, reducing the contrast to values closer to those measured in the experimental data.

The high impact from peripheral scattering can be explained by looking at the source spectrum of the betatron, Fig 4.6, and the attenuation coefficients of water and iron shown in Chapter 2 in Figs 2.2 and 2.3. The source spectrum shows that, although the maximum energy is 7.5 MeV, most photons are at much lower energies. Those below about 100 keV are likely to be absorbed relatively quickly, particularly if passing through the pipe as, from Fig 2.3, photoelectric absorption is the most probable interaction for photons below 100 keV in iron. This leaves most photons in the 0.1 MeV to 1 MeV range. At these energies Compton scattering is the most probable interaction, and the photons also have high enough energies that they are likely to be able to undergo multiple scattering events before reaching negligibly low energies. This makes it more likely that photons that have been scattered away from the detector will, after one or more additional scattering events, still reach the detector with significant energy remaining.

The high impact of peripheral scattering on an image with a 300 keV monoenergetic source is demonstrated in Fig 4.23, in which the relative scatter ratio is plotted along with that from a 2 MeV source. These effects, combined with the simulated results in Section 4.6, demonstrate that the probable cause of the difference between experimental and simulated

data is peripheral scattering. To confirm this, additional experiments in a more highly controlled environment could be performed, with lead shielding around the setup and fewer potential scattering objects in the exposure bay. While there would still be scattering from the lead, it has a much higher probability of photoelectric absorption compared to other materials such as iron or water. In lead, photoelectric absorption is a larger effect than Compton scattering up to about 500 keV, compared to 30 keV in water and 100 keV in iron. So a much greater proportion of the betatron spectrum would be absorbed rather than scattered if lead shielding were used. However, lead generates x-ray fluorescence at about 80 keV meaning some detectors may need additional copper shielding between the detector and lead.

The high proportion of peripheral scattering found in this study could have significant impacts for accurate simulation of radiographic inspections. Modelling is often used to check the feasibility of inspection setups and to calculate the expected quality of results. However generally only materials between the source and detector are included in the model, meaning scattering may be underestimated and results not representative of the actual inspection. For the example of a subsea pipeline inspection, accurate modelling would need to include the equipment surrounding and manipulating the source and detector as well as the water for some distance around the setup. In this case the actual inspection setup may be simpler to model than a laboratory setup, as in the actual inspection there is a large thickness of water all around which will greatly reduce scattering from objects at more than a short distance from the beam. In the laboratory case the water is likely to be in a relatively small container, allowing scatter to potentially reach all around the exposure bay.

The effects of additional scattering also make it harder to fully validate simulation models. It is very difficult to include an accurate representation of all possible scattering objects from an experimental setup in a modelling setup. Therefore when comparing simulated and experimental data there are likely to be differences even if the simulation is accurate for the modelled setup. This makes it harder to identify any other potential differences between experiment and simulation.

Instead of attempting to model many potential scattering objects it may be possible to achieve a better matching model by calibrating it with real data. In this case real data means data from the type of inspection being

modelled rather than experimental laboratory data. For the case of subsea pipelines, if real data of a subsea inspection can be obtained it could be used to estimate the proportion of peripheral scattering, which could then be added into the model. This would greatly simplify the model as it would not need to include the equipment surrounding the setup. However there would still be significant uncertainties, for example due to the sea floor. This could cause uneven scattering across the detector which would change if the setup were rotated. Any type of local scatter like this could cause inaccurate calibration of the model, either including the local scatter in all images or in none, depending on which experimental data was used for calibration.

4.8 Summary

The aim of this work is to investigate the accuracy of a radiographic simulation model for subsea pipeline imaging. A set of experimental data was obtained and used to adjust simulation parameters, aiming to match simulated results to experimental ones. The model was found to produce matching signal-to-noise ratios and the correct trend in contrast-to-noise. However differences were found in the profile across the radiograph and the CNR values. A possible cause of the discrepancies is scattering from objects in the experimental exposure bay which were not included in the simulation setup. Compton scattering is the dominant effect for the range of energies most common in the betatron spectrum, meaning the contribution of uncollimated scatter may be particularly strong for the setups examined in this work. Additional simulations were performed to test this possibility. Scatter from peripheral, out-of-setup objects was found to have a significant effect on the resulting image, in particular reducing the contrast. These results show that additional scattering from objects not included in the model is probably the cause of differences between experimental and simulated data. The implication is that for accurate modelling of an inspection scenario an area around the setup should be included in the model to account for additional scattering. An alternative would be to calibrate the model using a set of experimental data from the actual inspection being modelled. However there will still be unavoidable uncertainties, particularly in interpretations based on intensity.

5 Defect Characterisation

5.1 Introduction

Techniques of pipeline corrosion mapping with radiography have been investigated and standardised [3, 4] for use above water. Accepted inspection methods are the tangential and double wall techniques, with the double wall method being used in current practical subsea radiography. Double wall imaging is good for defect detection, imaging a relatively large portion of pipe wall in one exposure. For full coverage of the pipe wall the setup needs to be rotated about the pipe and images taken at different angles, but the number of images required is relatively low compared to the tangential method. However defect characterisation from double wall imaging can be difficult. Traditional methods of radiographic defect sizing rely on using additional objects of known size placed in the setup. For example, to estimate defect depth a step wedge must be included in the exposure, placed on the pipe as close as possible to the region of interest [4]. The step wedge is used in the resulting image to calibrate the relation of intensity to material thickness, allowing for defect depth to be calculated from its change in grey level. In a subsea environment, where the inspection is being controlled with a remotely operated vehicle, inclusion of objects such as a step wedge would add an additional layer of complexity to an already difficult inspection. Factors such as the positioning of the step wedge can impact the accuracy of the resulting defect characterisation, which could affect the reliability of the method. It has also been found that high levels of scattering – which would occur in subsea imaging – complicates analysis [100] and potentially causes errors. Therefore it would be advantageous to develop methods of defect characterisation for double wall pipeline radiography that do not require additional objects in the setup.

One method of full defect characterisation is computed tomography (CT). It would be ideal if a full 3D reconstruction could be achieved, as in CT.

However, it would not be feasible to acquire a CT scan along a subsea pipeline, partly due to the required acquisition time and therefore cost, and partly due to the less-than optimum setup of double wall single image causing severe truncated projection artefacts, as described in Chapter 2. An alternative promising technique is 3D point reconstruction. This method is based on stereography, in which two images are taken with the object in different positions. The setup geometry must be known, and 3D positions can then be obtained by triangulating points from the two images. The method was developed by Doering (1992) [101], and found to produce a significant amount of the information given by CT but with much lower cost and acquisition time. Research building on Doering's work includes that by Lindgren (2014, 2015, 2015) [102, 103, 104], which focusses on detection, sizing and positioning of submillimeter welding pores using 3D point reconstruction. Again the method is found to produce very good results. Another similar method is automatic multiple view inspection [105, 106], in which flaws are tracked through multiple radiographs in order to eliminate false positive indications. While both the setup and defect size range is very different from subsea pipelines, these methods demonstrate a capability to identify and characterise defects using relatively few radiographic images.

In this chapter I present a method of pipeline defect characterisation based on knowledge of the setup geometry and the use of images taken at different angles around the pipe. The method does not require changes to the radiographic setup or additional objects. It has been tested on a range of simulated and experimental data and found to give good agreement of lateral and axial defect size, and reasonable estimates of defect thickness in most cases. The method has the potential to be fully automatic, requiring input of a set of images and setup geometry and from this calculating defect size without further manual intervention. The defect characterisation method is described in detail in the following section. This chapter is based on a paper which has been published in NDT&E International [10]

5.2 Methods

For any radiographic setup, if the source and detector positions are known then the straight-line path from the source to each detector pixel in 3D space can be calculated. If the pixels in an image showing a defect can be identified

then the range of possible positions and sizes for the defect is found. This is illustrated as the cone of possible defect locations in Figure 5.1.

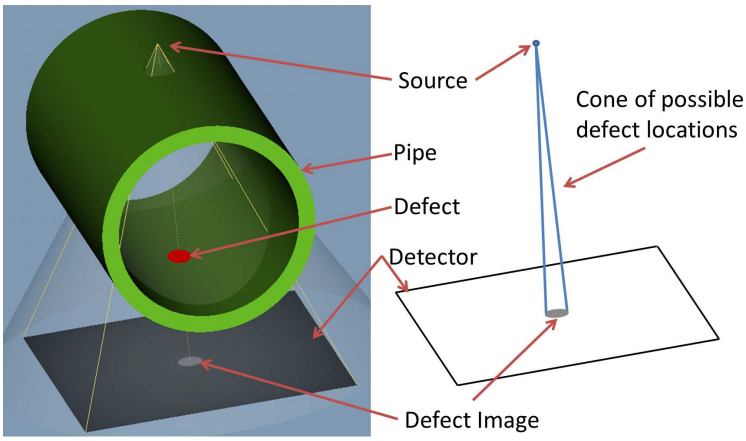

Figure 5.1: Left: An example setup for radiography of a pipe containing a flat bottomed hole defect. Right: Using just the source and detector positions, along with the extracted defect pixels, a cone of possible defect locations is calculated through ray tracing.

For a single image the range of possible defect locations and sizes is large, and no useful sizing conclusions can be drawn. However, if multiple radiographic images are taken at different angles around the pipe, with the same defect visible in several, then the range of defect sizes and locations can be significantly narrowed. The process of tracing a path from defect pixels to their corresponding source is repeated for each image, with the possible defect now limited to the region where rays from all images overlap. An illustration in 2D is shown in Figure 5.2 for the case of three rotated images of the same defect.

Characterisation from ray tracing of multiple images is significantly improved on single image results, particularly with regard to lateral and axial dimensions which are accurately determined at this point. However the depth resolution is still poor. In order to improve defect thickness calculations a series of constraints on possible defects are applied. For example, a constraint is applied on the pipe wall, and assumes the approximate location of the inner and outer pipe walls are known. Only that part of the possible defect volume which is inside the pipe wall can be defect, so any regions outside the pipe wall can be removed from consideration. Several

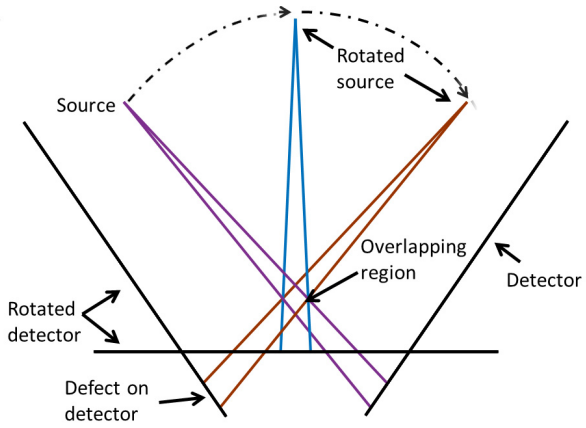

Figure 5.2: Lines are drawn from each defect pixel to its corresponding source position. If this is repeated for multiple rotated images showing the same defect then the 3D volume within which the lines overlap is the area where the defect is. An example for three images shown here.

other constraints are also applied and combine to greatly improve depth resolution.

The overall defect characterisation method is split into three parts: feature extraction, ray tracing and the application of constraints. The feature extraction method is based on background subtraction and is used to identify pixels showing a defect in radiographic images. This is followed by ray tracing, which makes use of the known source and detector positions and the angle of rotation between images to calculate the potential defect volume. Finally, constraints are applied.

5.2.1 Feature Extraction

The feature extraction method is based on background subtraction. The object being imaged is a pipe, so radiographs taken at different angles around the pipe should look broadly the same if no defects are present. Therefore images with no defect can be used to define the background. The background here refers to changes in grey level across an image not due to a defect. These background intensity variations can obscure changes caused

by a defect, and so background subtraction can be used to improve defect visibility. In order to define the background a minimum of two radiographic images of the pipe without any defects present are needed. More images provide improved resilience to effects such as changes in exposure conditions between images or differences due to pipe ovality. Figure 5.3 shows examples of the background mean and standard deviation calculated from a set of four simulated images of a pipe taken at different angles, with no defects visible.

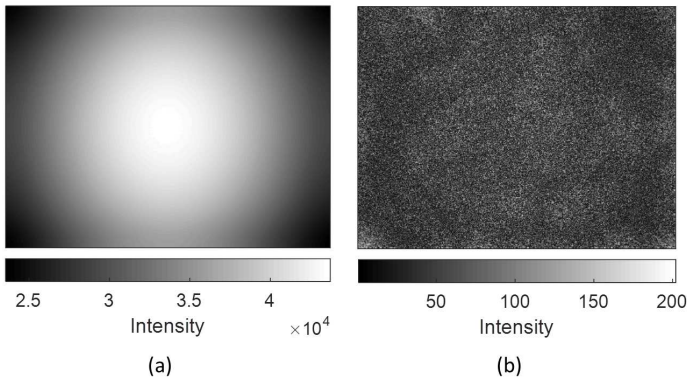

Figure 5.3: Characterisation of the background is key for feature extraction. The background mean, (a), is the mean intensity of the set of images without a defect present. The standard deviation of the same images is shown in (b).

Once the background has been characterised the next step is to subtract the background mean from the image of interest, which should allow the defect to be seen much more clearly. An example image of interest with a visible defect is shown in Figure 5.4. The new image, shown in Figure 5.5, is defined as $I_{norm} = I - B_m$ where I is the original radiograph and B_m is the background mean. With the background intensity variation removed the defect is much clearer in Fig 5.5.

If the background has been successfully removed then the average intensity in the image should be close to zero, with pixels that show a defect being furthest from this average. At this point a thresholding method is used to identify defect pixels in I_{norm}. A threshold T is chosen and pixels

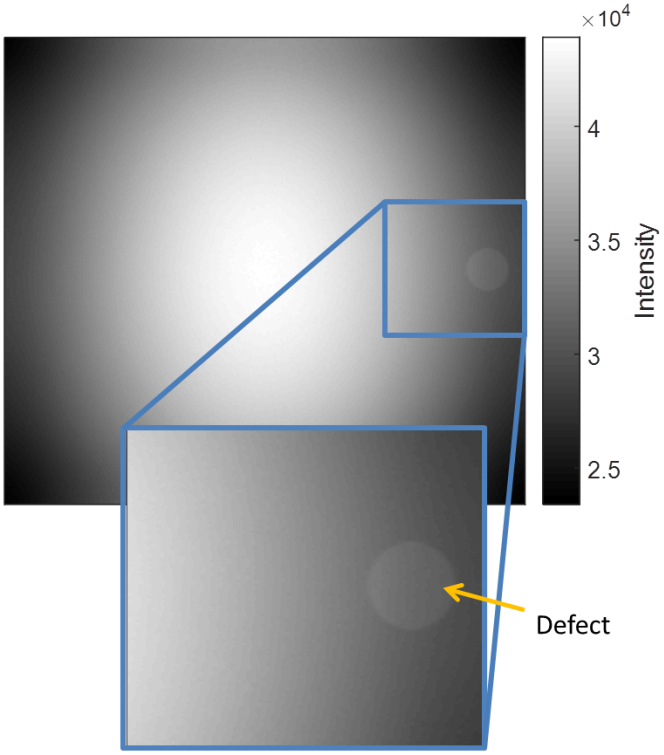

Figure 5.4: Original radiographic image, with the defect highlighted.

are selected as defect if the following relation is true:

$$|I_{norm}| > T \times B_{std} \tag{5.1}$$

where B_{std} is the background standard deviation. The initial threshold value T is set fairly high such that the incidence of false positives – pixels falsely identified as defect – is small, with the effect that not all defect pixels are identified. Figure 5.6 shows I_{norm} after thresholding, with defect pixels marked in red.

As is clear from Fig 5.6 this thresholding does not identify all defect pixels, therefore a lower threshold is needed to fully extract the defect. The lower threshold is adaptively chosen based on the defect pixels already found. These defect pixels are used to calculate a mean I_{norm} intensity for the defect, with a background mean I_{norm} calculated from the remaining pixels. By analysing a histogram of I_{norm} between the two means a lower threshold

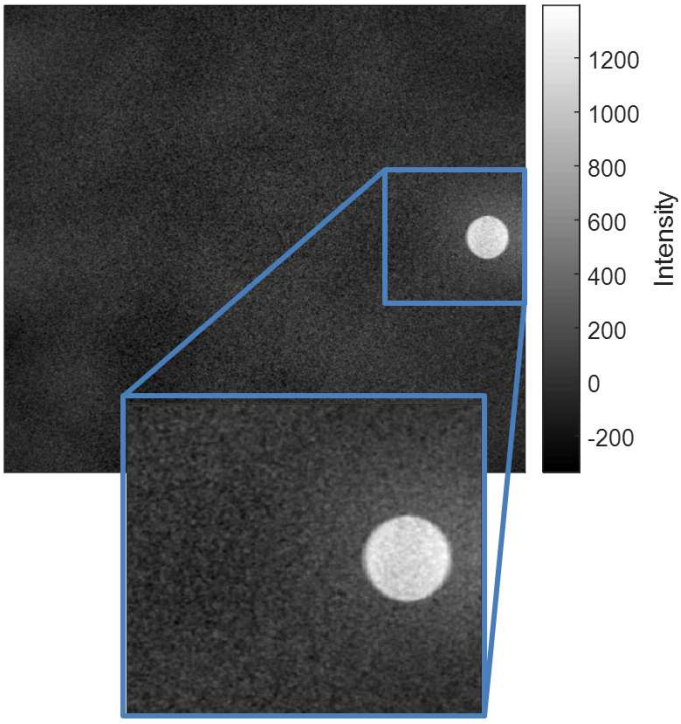

Figure 5.5: I_{norm}, the image after subtraction of the background mean. The defect is much more clearly visible compared to Fig 5.4, and most of the background intensity variation has been removed.

can be found. Beginning at the mean background value each histogram bin is compared to its neighbouring bins. The threshold is chosen as the first histogram bin which has greater frequency bins on both sides. Effectively, a minimum is identified between the background and defect means. This is illustrated in Figure 5.7, which shows a histogram of I_{norm} split into defect and background components, with both defect and background means marked, along with the identified border.

The lower threshold is then applied, selecting the remaining defect pixels. A filter is also used to remove isolated pixels. These are pixels which may have been picked as defect but have no neighbouring defect pixels and are therefore likely false positives, or vice versa for pixels set as background but surrounded by defect pixels. The filter is applied to the binary image in which a pixel is either a one for defect or a zero for background. It works by

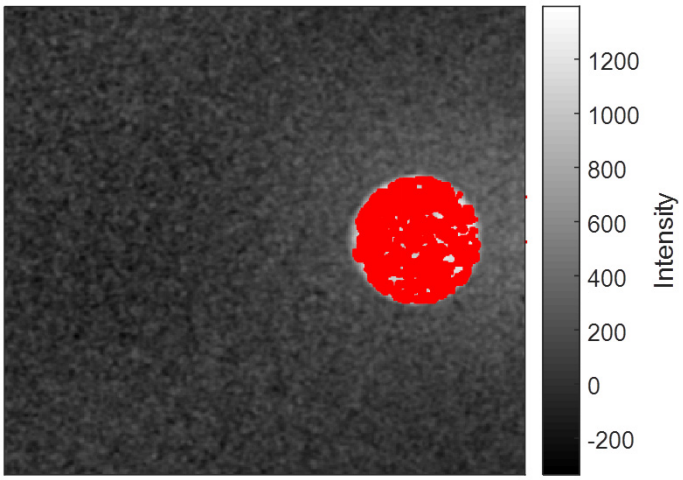

Figure 5.6: An enlarged area of I_{norm} after thresholding, with defect pixels marked in red. It is clear that not all defect pixels have been identified.

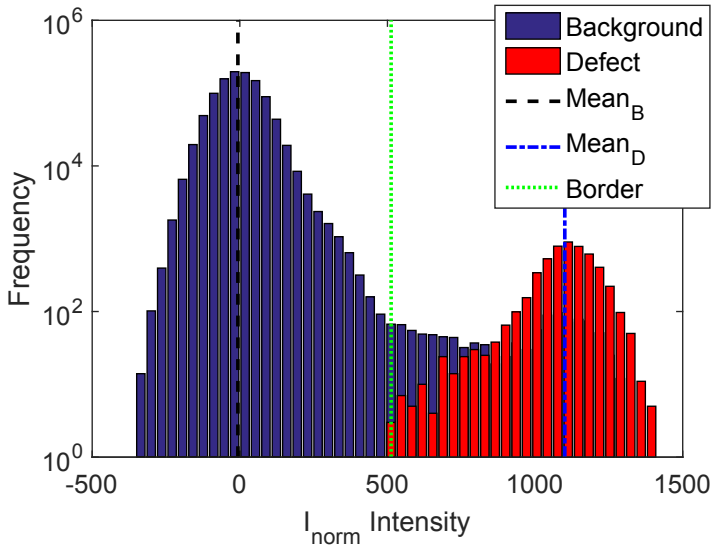

Figure 5.7: Log scale histogram of I_{norm} pixels. The histogram is coloured according to defect and background components.

first summing over the eight neighbours of each pixel, and then comparing this sum of neighbours with the value of the pixel. For a defect pixel the

sum should be greater than two, or for a background pixel it should be less than seven. If this criterion is not met then the pixel type is switched from defect to background or vice versa. Figure 5.8 shows the final I_{norm} with defect pixels in red. The detector coordinates of each defect pixel are now known, along with the intensity and difference from the background intensity. This is the key input for the ray tracing method.

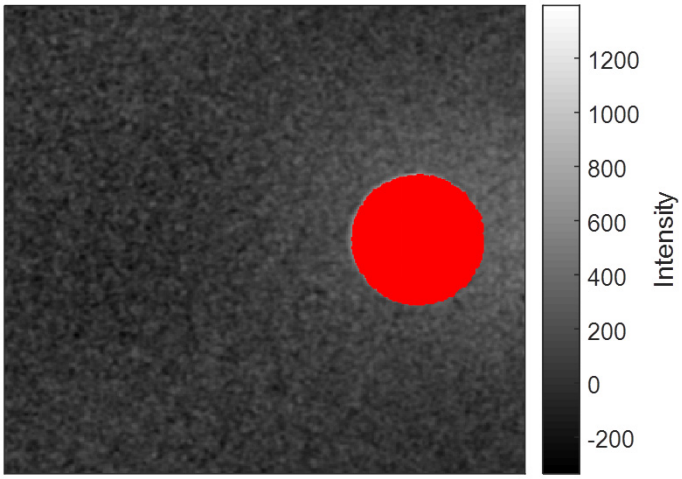

Figure 5.8: Resulting I_{norm}, with defect pixels marked in red. The majority of defect pixels have been successfully identified, although a small number around the edges of the defect may be missed.

5.2.2 Ray Tracing

In the ray tracing method, the space between source and detector is discretised into a 3D array of volume elements called voxels. The voxels through which each pixel to source line passes are calculated using a voxel traversal algorithm [107, 73, 74]. Voxels through which rays pass are flagged as a possible defect location, as shown in a simplified 2D case in Figure 5.9.

The ray tracing process is repeated for the images taken at different angles around the pipe, using the same voxels. Thus voxels through which rays from all images pass are identified. These overlapping voxels give a 3D volume and represent the range of potential sizes and locations of the defect. At this point the lateral and axial dimensions of the defect can be calculated

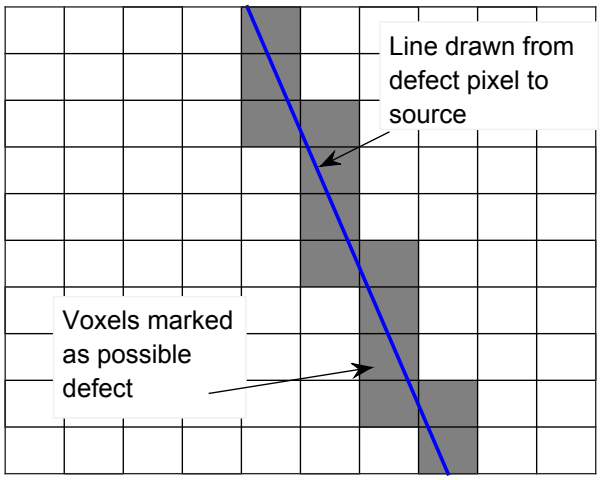

Figure 5.9: A line is traced back from each defect pixel to its source.

from the voxels. However, depth resolution is poor, with typically a range many times the actual defect size. Figure 5.10 shows the thickness map for the example of ray tracing of three images of a defect, one with the defect centred below the source and the other two at $\pm 60°$ angles. The defect is an inner wall flat bottomed hole with lateral and axial sizes of 25 mm in both dimensions and a maximum thickness of 3.05 mm. From the overlapping voxels the lateral and axial sizes are calculated as 25.2 mm and 25.5 mm respectively, in good agreement with the real size. However the maximum defect thickness, Fig 5.10, is found to be 35 mm, over ten times the actual defect maximum thickness. Therefore additional constraints on the defect volume are needed to better define the thickness. Note that defect thickness is used throughout this chapter to refer to the through-wall extent of the defect, or thickness of material removed.

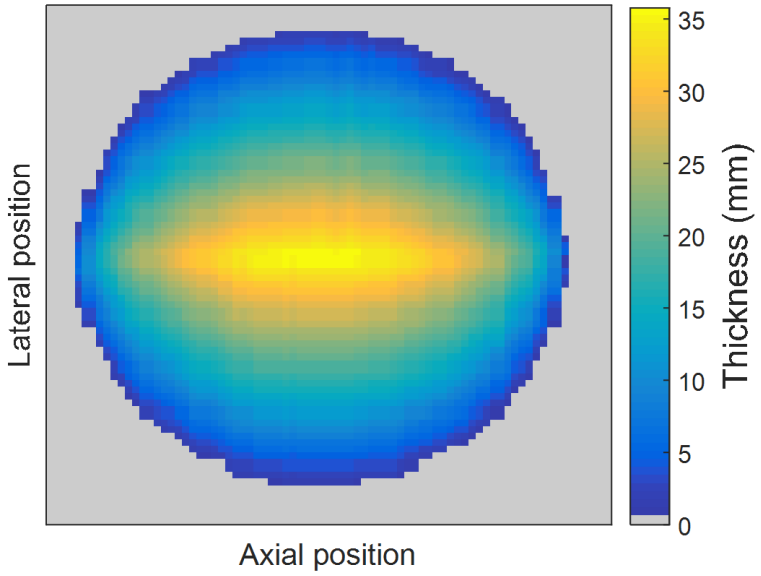

Figure 5.10: Defect thickness map calculated from the overlap volume produced by ray tracing. The actual defect thickness is 3.05 mm, demonstrating the need to apply additional constraints.

5.2.3 Application of Constraints

The simplest constraint to apply is on the pipe wall. This constraint requires that the approximate positions of the inner and outer pipe walls are known. Some error in position is acceptable, as the input positions will be varied to identify if any close positions are more likely. The pipe wall constraint is that for voxels to be considered as part of a defect they must be between the inner and outer pipe wall positions. This is illustrated in Figure 5.11 which shows the pipe location imposed over the simple 2D ray tracing example. The area of potential defect is significantly reduced, as any part of the overlapping volume outside the pipe wall is no longer considered. The thickness map of the potential defect volume after application of the pipe wall constraint is shown in Figure 5.12. The maximum possible thickness has been reduced by almost a factor of two. However, it is still fairly large and has not been narrowed sufficiently to give a good estimate of the defect thickness.

The next constraint that is applied makes use of the intensity of each pixel. Taking each image in turn the thickness map for that image is calculated; that is, the distance a ray travelled through the defect before arriving at each

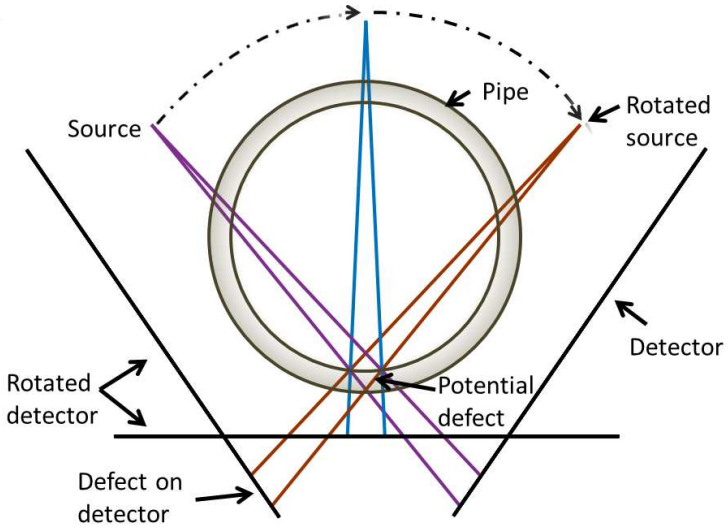

Figure 5.11: The potential defect must be in the region within the pipe wall.

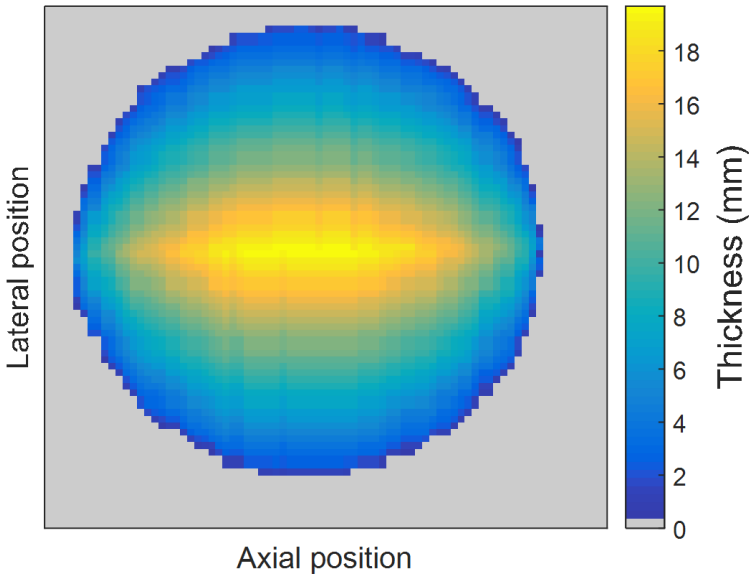

Figure 5.12: Thickness map of potential defect after applying the pipe wall constraint. The maximum possible thickness has been reduced from Fig 5.10 by almost a factor of two.

pixel. These image specific thickness maps are calculated from the potential defect voxels resulting after application of the pipe wall constraint. From the background subtraction the difference between the detected intensity and background intensity, I_{norm}, is known for each image pixel. The magnitude of I_{norm} indicates the impact of the defect, with a high I_{norm} meaning a more significant impact than low I_{norm}. Although the exact mapping from I_{norm} to distance travelled through the defect is unknown, it should be the case that a ray travelling through a thick defect will result in a larger I_{norm} than one travelling through a thin defect. Therefore the relationship of higher I_{norm} meaning longer distance can be imposed on the defect pixels. This relationship is only imposed within an image as there may be other causes of different I_{norm} between images.

Figure 5.13 shows the intensity of each defect pixel for the image with a centred defect. The procedure is to sort the pixels by intensity. The distance travelled through the defect volume for each pixel can then be analysed in relation to intensity. The defect thickness, or distance, is modified such that a pixel with lower intensity will also have a shorter distance travelled through the defect. The process is illustrated for a small number of pixels in Figure 5.14 which shows the original distance and that after processing. The same minimum and maximum overall thicknesses still remain after distance processing, but they have been redistributed to match the intensity. The image specific defect thickness after distance processing is shown in Figure 5.15. Comparing with the I_{norm} intensity map, Fig 5.13, the maximum distance now corresponds to the maximum intensity.

The final constraint used is on the effective attenuation coefficient. This constraint is also applied within each image individually, based on the image specific thickness maps. The intensity of direct radiation arriving at a pixel, I, is given by the Beer-Lambert law of attenuation:

$$I(E) = I_0(E)e^{-\mu(E)x} \tag{5.2}$$

where E is the energy of the photons, I_0 is the initial radiation intensity, μ is the attenuation of the material and x is the distance travelled through the material. In this case we have two images; one of the background and one with a defect present. For a given pixel in the defect image the intensity

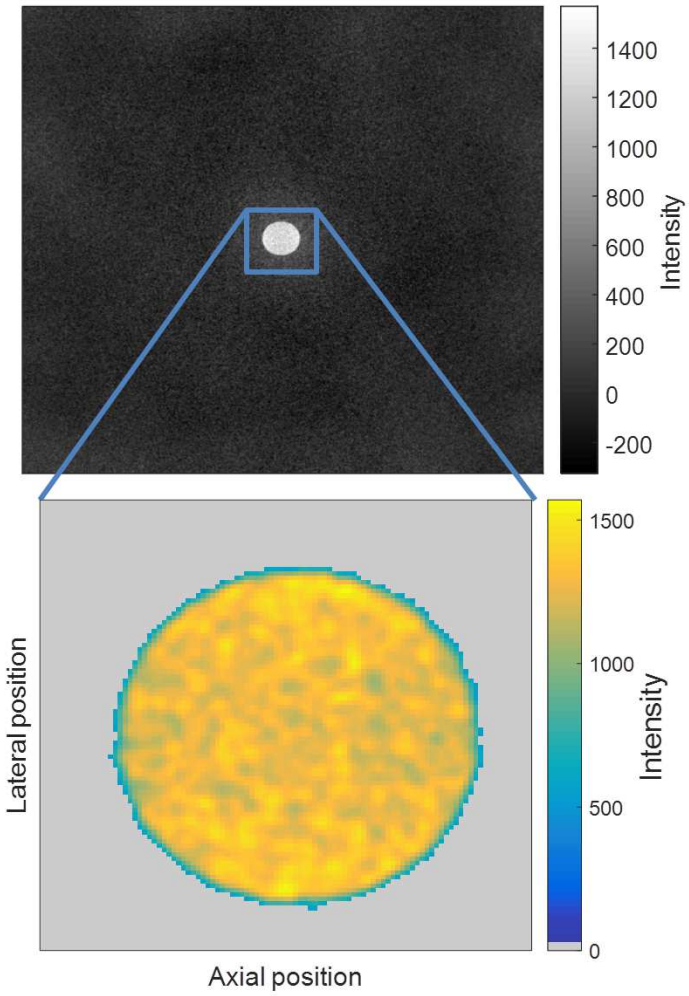

Figure 5.13: Intensity (I_{norm}) of the pixels in the image with a centred defect. Pixels not identified as defect are ignored, hence they are set to zero in this example image.

of the background I_B and the intensity through the defect, I_D, are:

$$I_B = I_0 e^{-\mu_{eff} x_t} \tag{5.3}$$

$$I_D = I_0 e^{-\mu_{eff}(x_t - x_D)} \tag{5.4}$$

where x_t is the total distance from the source to pixel, x_D is the distance travelled through the defect and μ_{eff} is the effective attenuation coefficient which depends on both the materials travelled through and the photon

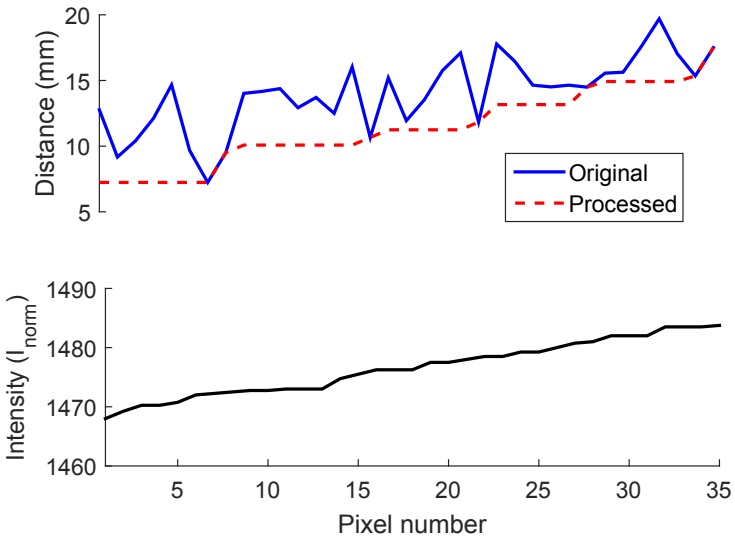

Figure 5.14: An example of distance processing. Defect pixels are sorted in order of increasing normalised intensity ($I_{norm} = I - B_m$). The distance travelled through the calculated defect by each pixel is then modified to follow the same relation as intensity, ie if a pixel has a lower intensity than another it must also have a smaller distance.

energies. Dividing these equations:

$$\frac{I_D}{I_B} = \frac{e^{-\mu_{eff}(x_t - x_D)}}{e^{-\mu_{eff} x_t}} = e^{\mu_{eff} x_D} \tag{5.5}$$

This leads to the final equation for effective attenuation coefficient:

$$\mu_{eff} = \frac{1}{x_D} \ln\left(\frac{I_D}{I_B}\right) \tag{5.6}$$

In this equation both I_D and I_B are known and an estimate of x_D has been found, as shown in Fig 5.15. This means the effective attenuation coefficient for each pixel in an image can be calculated. The effective attenuation coefficient for each pixel is shown in Figure 5.16.

At this stage a constraint can be applied on the range of μ_{eff} values. It is assumed that, as the defect is fairly localised, μ_{eff} should not vary significantly between pixels with similar intensities. The allowed range in μ_{eff} is decided based on the range in I_{norm}; images with a large range of

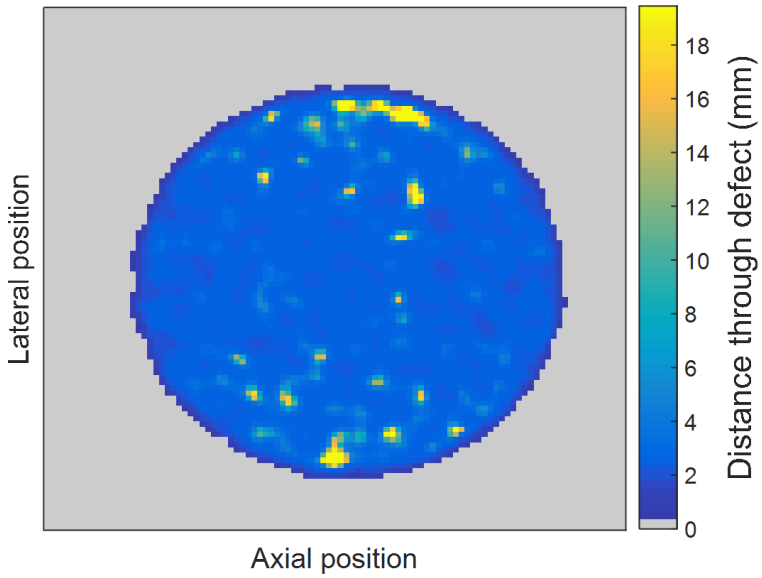

Figure 5.15: Defect thickness after distance processing. Pixels of high intensity are now assigned higher thickness than low intensity pixels. This is the image specific defect thickness, calculated as the distance travelled through the defect for each pixel in the image with a centred defect.

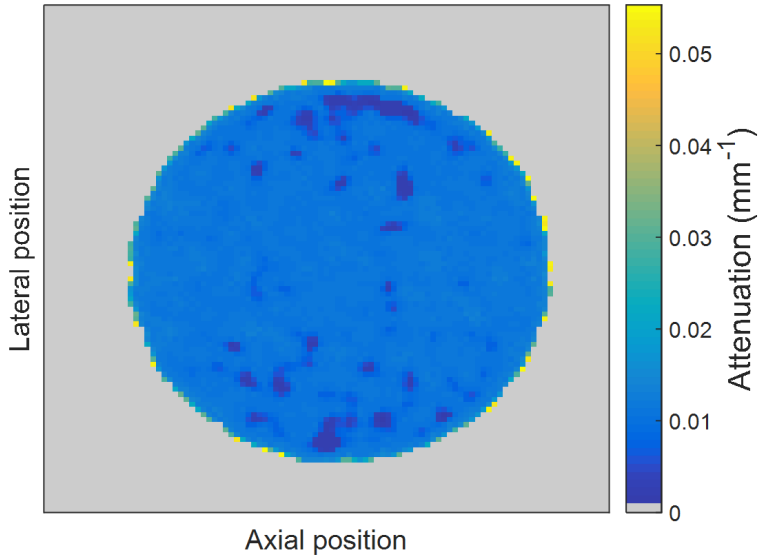

Figure 5.16: The effective attenuation coefficient for each pixel, calculated using the distances through the defect illustrated in Fig 5.15.

intensity are allowed a larger range in μ_{eff} than those with small intensity ranges. The calculated μ_{eff} values are then mapped to the allowed range, with the mean value and the relative ordering of pixels conserved. Finally Eqn 5.6 is inverted to calculate x_D based on the new μ_{eff} values. The effect is to remove extreme values of defect thickness, both high and low. The resulting image specific defect thickness is shown in Figure 5.17. Comparing with the defect thickness prior to this constraint, Fig 5.15, it can be seen that the extremes in defect thickness have been removed. Since the ordering of pixels was conserved the relation of longer distance occurring in pixels with higher intensity still holds, as can be seen comparing to the intensity map Fig 5.13.

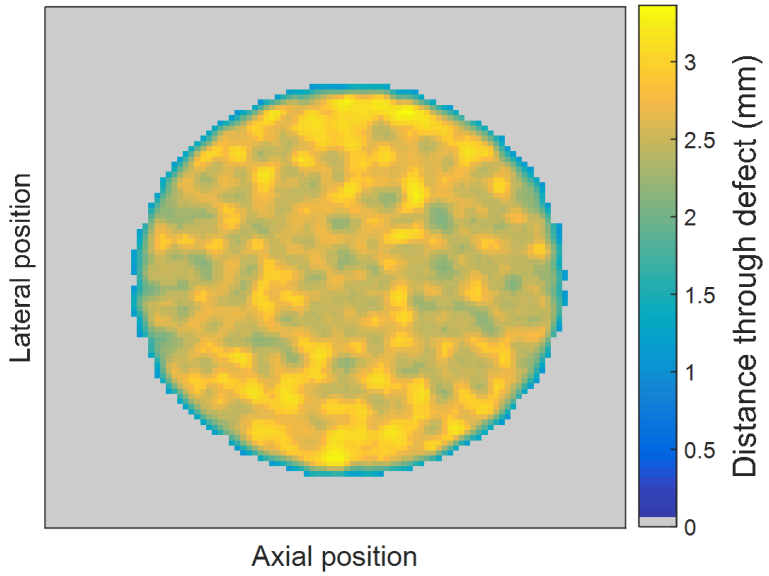

Figure 5.17: Distance travelled through the defect for the image with the defect centred, after the application of all constraints.

The final step is to convert the image specific thickness map back into voxels so that the dimensions in x, y and z can be calculated. If an image with a centred defect was used then this image produces the most accurate results after application of the last two constraints, relating to intensity. This is because, with the defect in line with the source, intensity maps more directly to defect thickness than in images taken at an angle. Therefore the specific thickness of the centred image is used to calculate the final defect thickness map. If the centred image is not available then the final

defect thickness map can be calculated by combining the specific maps of all images, however this will result in higher errors. In this example the centred image is used to calculate the final thickness map, shown in Figure 5.18.

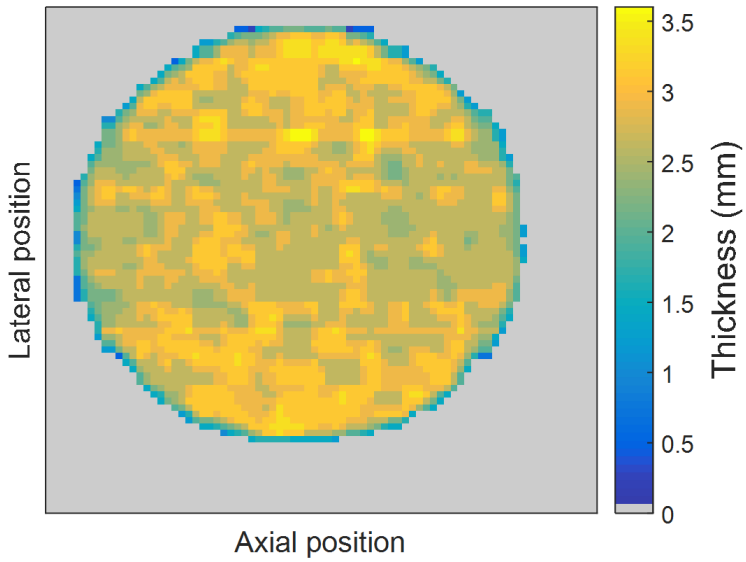

Figure 5.18: Thickness map of the defect after application of all constraints.

The true thickness map of the defect is shown in Figure 5.19. Comparing Fig 5.18 and Fig 5.19, it can be seen that the calculated defect is very close to the real one. While individual pixel values are variable, the overall maximum thickness is within 0.5 mm of the actual maximum. Instead of taking the single maximum thickness, an estimated defect depth is calculated as the mean of the highest 1% of pixels. This provides resilience against possible effects of a very small number of high thickness pixels. In this case the estimated defect thickness is calculated as 3.25 mm, while the true thickness is 3.05 mm.

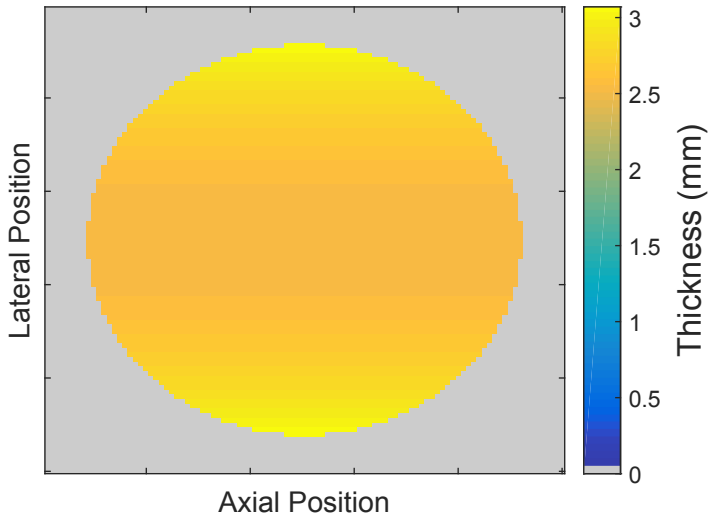

Figure 5.19: Real thickness map of the defect.

5.3 Experimental and Simulation Studies

5.3.1 Data Acquisition Methods

The defect characterisation method described in the previous section has been tested on a range of defects; both simulated and experimental flat bottomed hole defects and simulated realistic corrosion defects. This section details the methods used in obtaining the data.

Simulated data was produced in aRTist; for more detail, Chapter 4 explained methods of simulation in aRTist. The simulated source and detector were modelled based on a 7.5 MeV betatron source and a digital detector respectively. The setup used was a 320 mm diameter pipe with 25 mm wall thickness and a source to detector distance of 400 mm, giving a double wall single image inspection configuration. Two different types of defect were used; ideal flat bottomed hole defects and realistic corrosion type defects. Defects were positioned in the inside pipe wall in line with the source such that at 0° rotation the defect was centred in the image. The simulation was run in Computed Tomography mode so that it would rotate the setup, taking images at defined angular intervals. Each simulation was run with a single defect present, so images produced never had more than one defect visible. Background images were taken as a set of four images in which the

defect was out of view. The same set of background images was used for all simulated cases.

The experimental data used here was collected during the Simulation Validation work described in Chapter 4. The data is of the same stepped pipe, source, detector and setup parameters as previously described. The data of most use here is a set in which the pipe was placed on a turntable and rotated, with images taken at every 5° rotation. The centre of rotation was as close as possible to the pipe centre. An example of a resulting radiograph is shown in Figure 5.20.

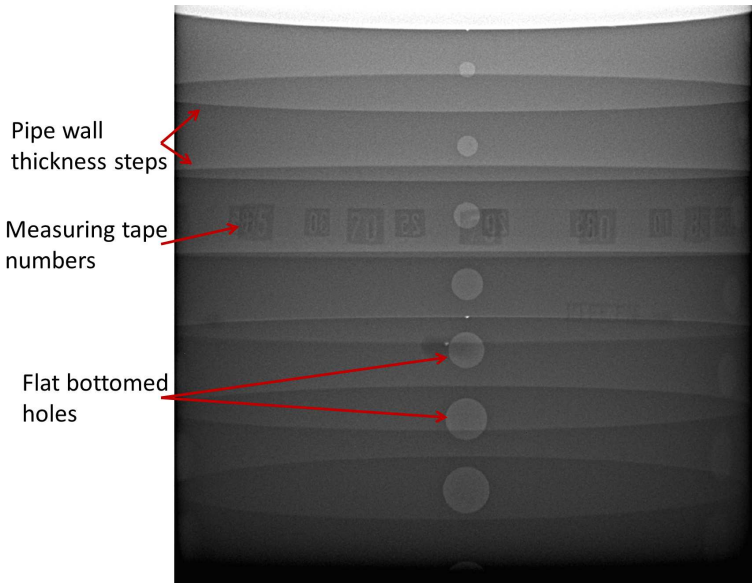

Figure 5.20: An example of an experimental double wall radiograph. It has been filtered for better visualisation. The steps in pipe wall thickness are clearly visible, along with one set of flat bottomed holes. A measuring tape with lead numbers that was wrapped around the pipe can also be seen.

As this data was collected for a different set of work [7] it is not ideal data for testing the defect characterisation method. Multiple features, both flat bottomed hole defects and step changes in wall thickness, are present in all images. This means there was no background set of images without defects present to use for feature extraction. Instead, a set of images was chosen in which no features overlapped significantly with the region of interest, allowing for their use as background images. A window around each region of interest in the images was set manually, and in cases where slight overlap

of outside features occurred the threshold was also adjusted manually.

5.3.2 Results

The defect characterisation method was tested on both simulated and experimental flat bottomed hole defects and simulated corrosion defects. Current work is focussed on inner wall defects and hence defects tested are all inner wall. However the method is also applicable to outer wall defects, which we aim to examine in future work. A key point is that for any defect the method calculates a potential size for both inner and outer wall, and if possible decides which is more probable based on consistency with input parameters. If it is known that the expected defect is inner or outer wall then this can be input to the model. If it is not known and the model is unable to select one then both sets of results are produced, generally resulting in a wider potential range in defect size. For the following results the model was successful at designating the defect as inner wall, however an example set of results is given to demonstrate the effect of calculating defect size with the incorrect assumption of an outer wall defect.

Simulated Flat Bottomed Holes

The 25 mm diameter flat bottomed hole defect with maximum depth 3.05 mm, as used to illustrate the method in Section 5.2, was used to investigate the impact of the angle between images on the resulting characterisation. Images were taken at 5° angles around the pipe. The defect was found to be fully visible in the images between ± 60°, with further rotation putting it partially or completely out of the shot. The method requires three input images; the key recommended image is that with the defect centred, as this should give greater accuracy both in calculating lateral and axial dimensions and in application of constraints on thickness. Therefore the centred defect image was included in all sets of images. The other two images were set as ranging from ± 5° to ± 60°, giving twelve sets of images with the same angular separation between all three images in each set. The defect characterisation method was run on all sets of images. The resulting axial and lateral dimensions are plotted in Figure 5.21. Results show an improvement in sizing with greater angular separation between images, but even for the 5° separation the calculated size is within 1 mm of the actual size.

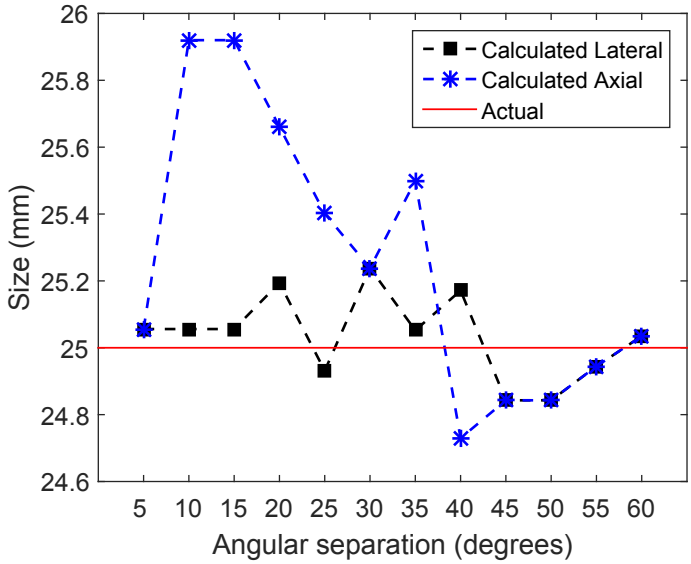

Figure 5.21: Calculated lateral and axial dimensions for a flat bottomed hole defect using different sets of three images. The image sets all include the straight down, centred defect image and two other images ranging from ±5° to ± 60° rotation from the central image. The flat bottomed hole has a real size of 25 mm in both dimensions.

The calculated defect thickness is shown in Figure 5.22, and in this case there is a significant dependence on angular separation. With small angle separations it is not possible to narrow down the defect thickness at all, and thus the result is at the maximum feasible value, close to the pipe wall thickness. It is only at high angular separations, from around 50°, that thickness estimates close to the real value are obtained. This implies that the best images to use for defect characterisation, in addition to the centred defect image, are those at the largest angular separation in which the defect is visible.

As stated in the previous section, it is expected that errors will be greater if the 0° straight down, centred defect image is not included in the set of three images. To test whether this is true, and if so how big the errors are, the defect characterisation method was run on sets of three images without the 0° image. The images were of the 25 mm flat bottomed hole defect, and the image sets all used the two images at ± 60° rotation. The third image

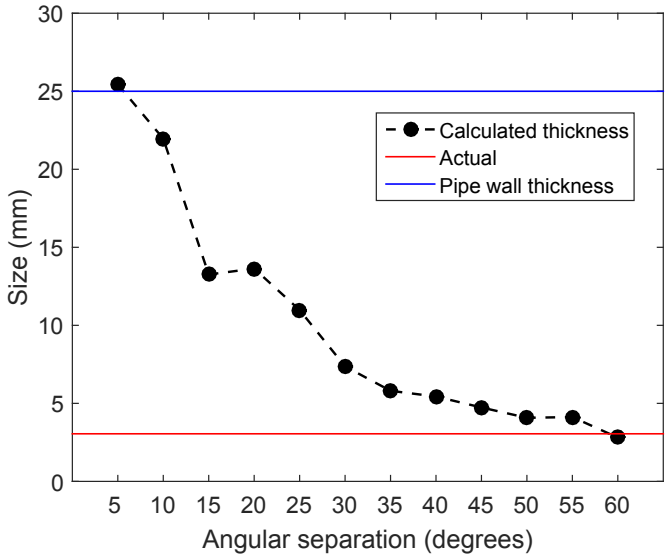

Figure 5.22: Calculated thickness for a flat bottomed hole using the same sets of images as in Fig 5.21. The pipe wall thickness, 25 mm, and true defect maximum thickness, 3.05 mm, are also shown.

ranged from the expected best case of 0° to a 30° rotation image, in steps of 5°. The calculated lateral and axial dimensions for each set of images are plotted in Figure 5.23. The error in axial size is fairly small for all cases. This is because all the images have the defect centred in the axial direction. The error in lateral size begins to increase after the 10° image, and becomes greater than 1 mm after 15°. The calculated maximum defect thickness for the same sets of images is shown in Figure 5.24. In this case errors increase much faster than for the lateral size, with the calculation overestimating by a factor of two at the 20° case. It was also observed that the defect thickness maps were much more variable in these results than when the 0° image was used. These figures demonstrate that results should always be more accurate if the 0° image is used. However, error is still fairly small with an image up to 10° rotation, meaning it is not crucial to get an image at exactly 0°.

Figs 5.23 and 5.24 also show why a minimum of three images is used for characterisation. Without a 0° or close to 0° image there would be much more error in lateral and depth dimensions. While from Figs 5.2 and 5.22 it can be seen that the two images at the largest rotation to either side of

the 0° image contain the most unique information and produce the most accurate characterisation. So although some characterisation could be made using only two images, errors would be significantly increased.

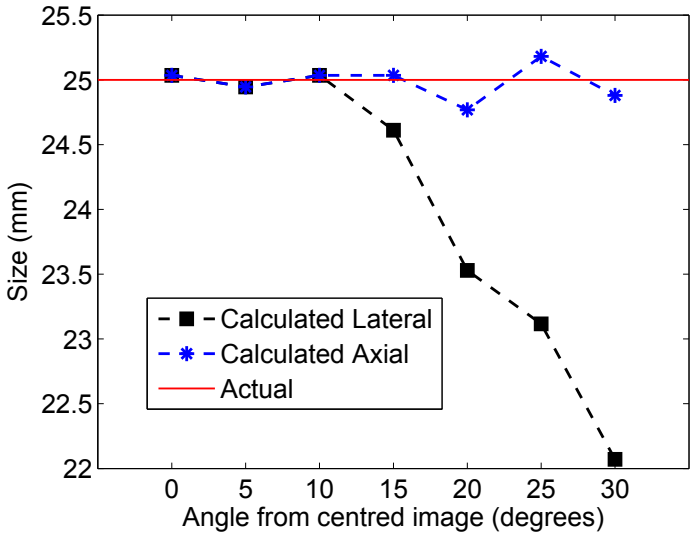

Figure 5.23: Calculated lateral and axial dimensions for a flat bottomed hole defect using different sets of three images, examining the error if the straight down, centred defect image is not included. The image sets all include the two images at ± 60° rotation. The third image ranges from the straight down, centred defect image to a 30° rotation image in steps of 5°. The flat bottomed hole has a real size of 25 mm in both dimensions.

The impact of using more than three images was also tested. Figure 5.25 shows the calculated lateral and axial sizes for a range of different sets of images. In this case each set included images at 5° intervals up to the maximum angle, with the maximum angle from ±5° to ± 60°. For example, the set of images with a maximum angle of 10° contained five images, that with a maximum of 15° contained seven images and so on. Fig 5.25 can be compared with Fig 5.21, which shows results for the same maximum angles but using only three images. The effect of including many more images is small, with a similar range of results. The calculated defect thickness for the same sets of images was also found not to have improved upon results using only three images, Fig 5.22, and the same maximum angles. Slight differences, of less than ±0.2 mm, were found making the results from many

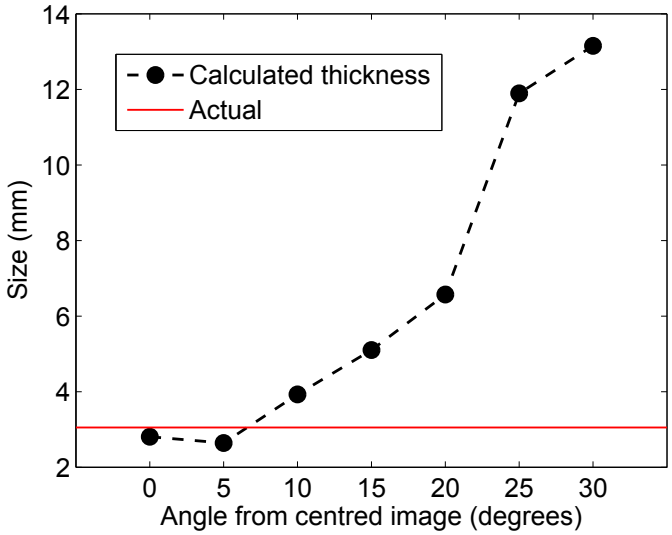

Figure 5.24: Calculated thickness for a flat bottomed hole using the same sets of images as in Fig 5.23. The true defect maximum thickness, 3.05 mm, is also shown.

more images barely distinguishable from those with three images. This demonstrates that, for a set of images with a given angular separation, there is no benefit to including additional images at angles in between those already used. The ideal set of images to use is three images; one centred at 0° and two at the maximum possible angles to either side.

To investigate whether defect diameter affects the accuracy of results the simulation, taking images every 5°, was run with three different diameter flat bottomed holes. The defect characterisation method was then run on each set of three images, again with angular separation from ± 5° to ± 60°. The actual hole depth was 5.5 mm in each case, and the hole diameters were 12.5 mm, 25 mm and 50 mm respectively. The difference between calculated and actual lateral and axial size was used to compare results. Both lateral and axial results were very similar so axial size is given as an example, shown in Figure 5.26. It can be seen that the error in the 50 mm diameter case is significant until at least a 15° separation, however from 15° all results are fairly good, within ± 2 mm of the actual size.

The defect thickness results for the same sets of images are shown in Figure 5.27. As found for the 3 mm defect, Fig 5.22, the accuracy of the results improves with angular separation. There are no significant differences

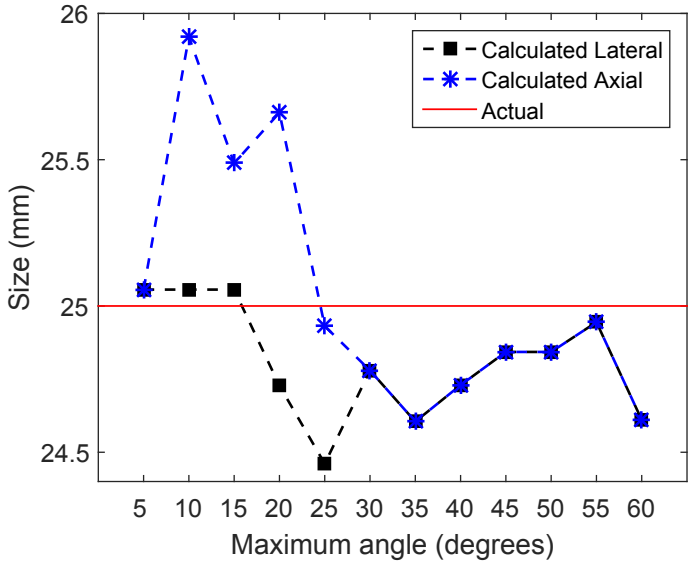

Figure 5.25: Calculated lateral and axial dimensions for a flat bottomed hole defect using different sets of images. The image sets all include the straight down, centred defect image and all other images at 5° intervals up to ± the maximum angle. The flat bottomed hole has a true size of 25 mm in both dimension.

seen between the different diameter holes, although the 50 mm result again behaves more erratically for small angular separations.

The effect of defect thickness on accuracy and required angular separation was also tested. The same simulations were run for three flat bottomed hole defects with a 25 mm diameter and different thicknesses of 5.5 mm, 10.5 mm and 15.5 mm respectively. Axial and lateral dimensions were again calculated fairly accurately from small angular separations. However, for defect thickness calculations higher errors were found. This is demonstrated in Figure 5.28 which shows the error in defect thickness for each of the defects for a range of angular separations. The smallest, 5.5 mm, defect is seen to give fairly good results from around 40° separation, while the 10.5 mm defect only gives a good result at 60° and the 15.5 mm defect calculated thickness never comes within ±5 mm of the actual value. This result demonstrates that the actual defect size can have a significant impact on the accuracy of the characterisation.

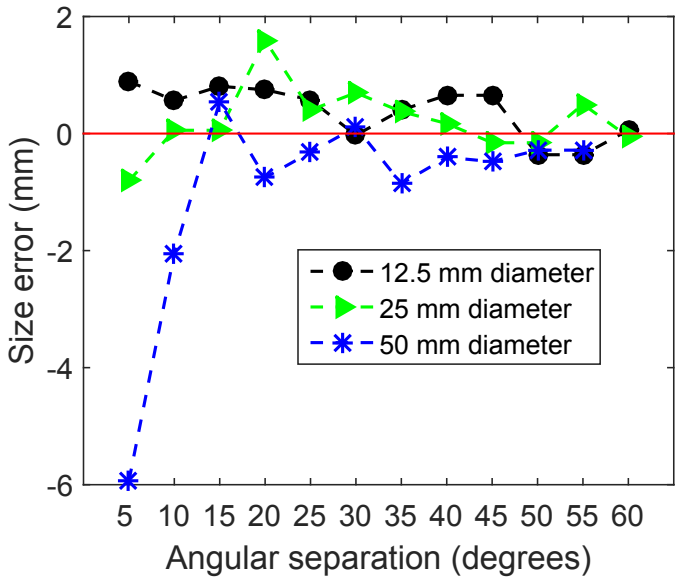

Figure 5.26: Error in axial size, defined as (calculated - actual) size, for flat bottomed holes with diameters of 12.5 mm, 25 mm and 50 mm. Results for sets of three images with angular separation ranging from ±5° to ±60° are shown. The 60° angular separation case for the 50 mm defect is not shown as the defect was partially out of the field of view at 60°.

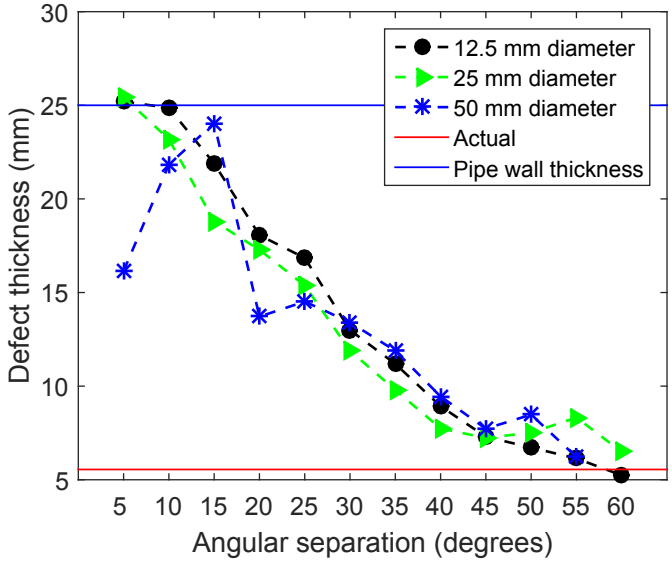

Figure 5.27: Calculated thickness for flat bottomed holes with diameters of 12.5 mm, 25 mm and 50 mm.

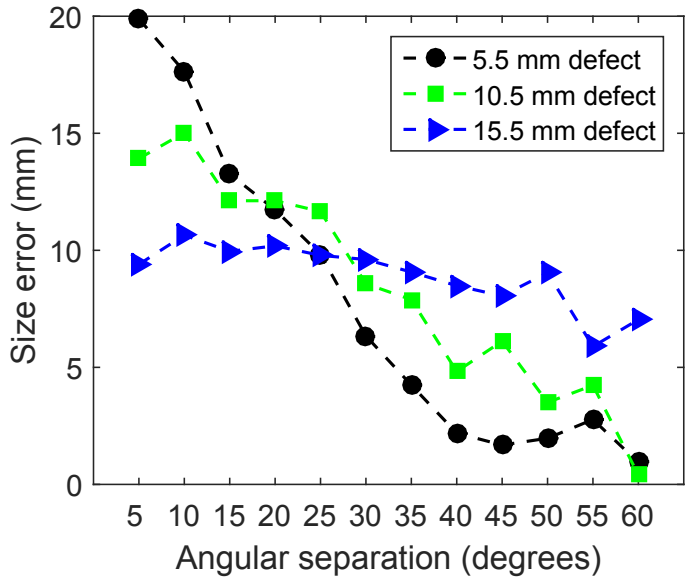

Figure 5.28: Thickness error for flat bottomed holes with 25 mm diameter and thicknesses of 5.5 mm, 10.5 mm and 15.5 mm. Results for sets of three images with angular separation ranging from ± 5° to ± 60° are shown. Error was taken as (calculated - actual) size.

Experimental Flat Bottomed Holes

The defect characterisation method was also tested on experimental data. The aim was to calculate the sizes of two sets of flat bottomed holes in the stepped pipe shown in Fig 4.1. The pipe wall thickness ranged from 8.5 mm to 25 mm and the sets of flat bottomed holes were of 20% and 50% wall thickness respectively. The diameter of each hole was equal to the wall thickness, giving a range of diameters from 8.5 mm to 25 mm. Three images were selected for each of the sets of holes. Images had to be chosen in which the defects did not overlap with other features, as this would obscure the defect and make background subtraction difficult. For both sets of holes the image was chosen in which the defects were, visually, close to the centre line of the image. For the 20% holes the other two images were taken as those at -45° and +60°, while for the 50% holes the images were at ±45° from the central image. The defect characterisation method was run on each hole individually. The difference between calculated and actual dimensions was used for comparison of accuracy. The results for the 20% holes are shown in Figure 5.29, while those for the 50% holes are shown in Figure 5.30.

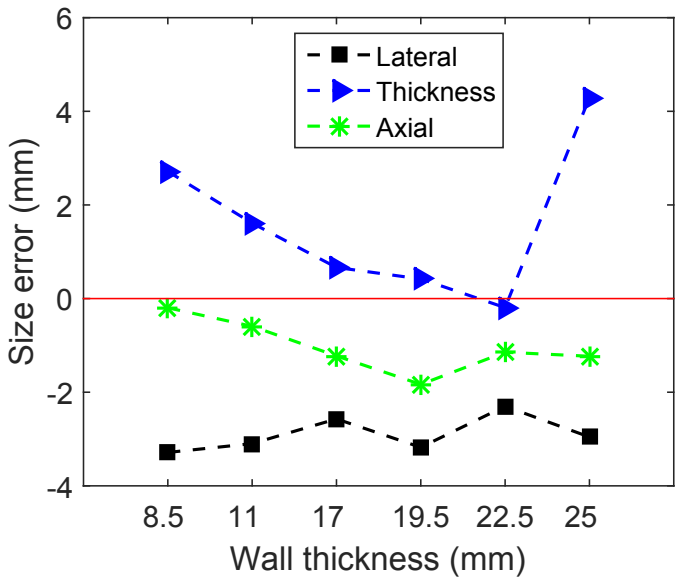

Figure 5.29: Error in dimensions of 20% wall thickness flat bottomed hole defects. Dimensions were calculated using a set of three experimental images. The images were used were at 0°, -45° and +60°. Error was taken as (calculated - actual) size.

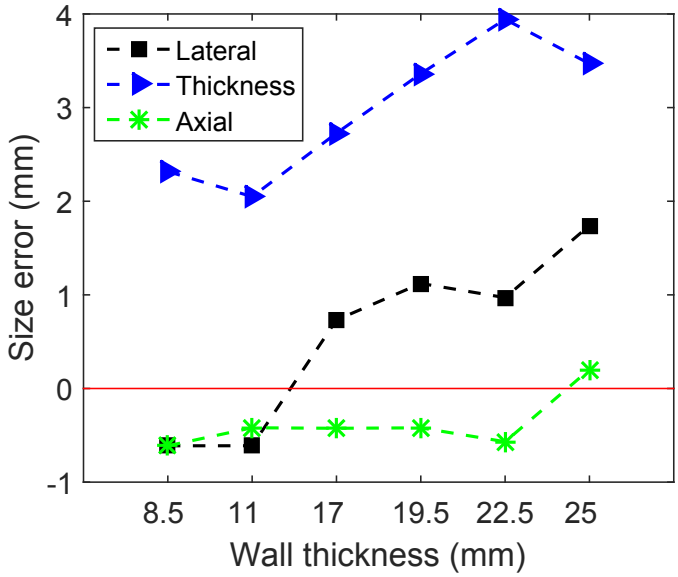

Figure 5.30: Error in dimensions of 50% wall thickness flat bottomed hole defects. Dimensions were calculated using a set of three experimental images. The images used were at 0° and ±45°. Error was taken as (calculated - actual) size.

Calculated and experimental dimensions in Figs 5.29 and 5.30 show good agreement, although a slightly higher error is seen compared to the results for simulated data. There are many additional causes of error introduced by the experimental data, for example errors in the setup dimensions such as source to detector distance and pipe centre position, the centre of rotation and finally no background images to calibrate the background subtraction. So for results to be within ±4 mm of the actual values and in most cases much closer is a positive sign, demonstrating the applicability of the method to experimental data.

Simulated Corrosion

The method was also tested on realistic corrosion defects. A CAD model of a real corrosion defect obtained from laser scan data was added to the aRTist setup to obtain simulated data. The aRTist setup used was the same as for the flat bottomed hole defects. A thickness map of the defect is shown in Figure 5.31.

A series of different sized real corrosion defects were obtained by scaling

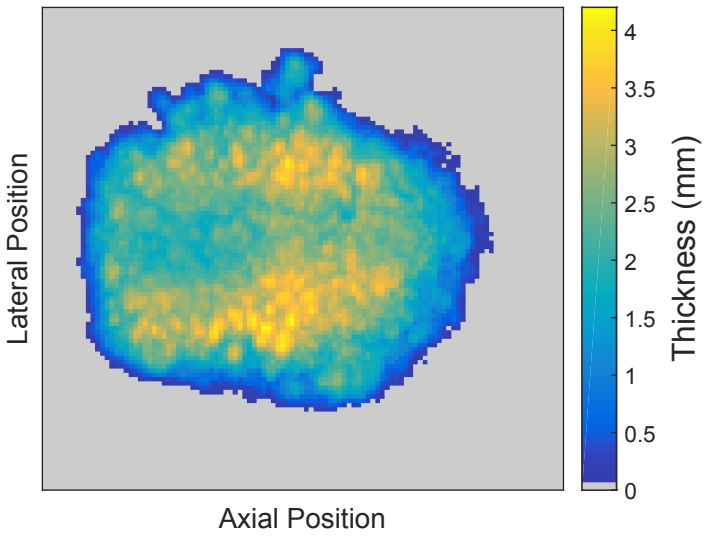

Figure 5.31: Thickness map of the real corrosion defect. The lateral and axial sizes are 20.8 mm and 21.1 mm respectively.

the original defect. For the first set of defects the depth was scaled by factors of two, three and four giving a maximum thickness of 7.9 mm, 11.7 mm and 15.9 mm respectively compared to the original maximum of 3.8 mm. The lateral and axial dimensions were kept constant at 20.8 mm and 21.1 mm respectively. The defect characterisation method was run for each defect using images taken at 0° and ±60°. The calculated thickness map of the original, unscaled defect is shown in Figure 5.32.

The results for all four defects, in terms of the difference between calculated and actual dimensions, are shown in Figure 5.33. All results are within ±2 mm of the actual dimensions. The underestimation of axial and lateral dimensions may be due to the feature extraction method missing some defect pixels around the edge of the defect where, from Fig 5.31, they are mostly low thickness and therefore more difficult to detect.

A second set of defects was produced by scaling the lateral and axial dimensions of the four different thickness defects to be 33.2 mm and 33.8 mm respectively. Therefore this set of defects had the same thicknesses as those in Fig 5.33 but larger lateral and axial sizes. The resulting difference between calculated and actual size is plotted in Figure 5.34. Errors are slightly higher for the larger diameter defects, although all results except

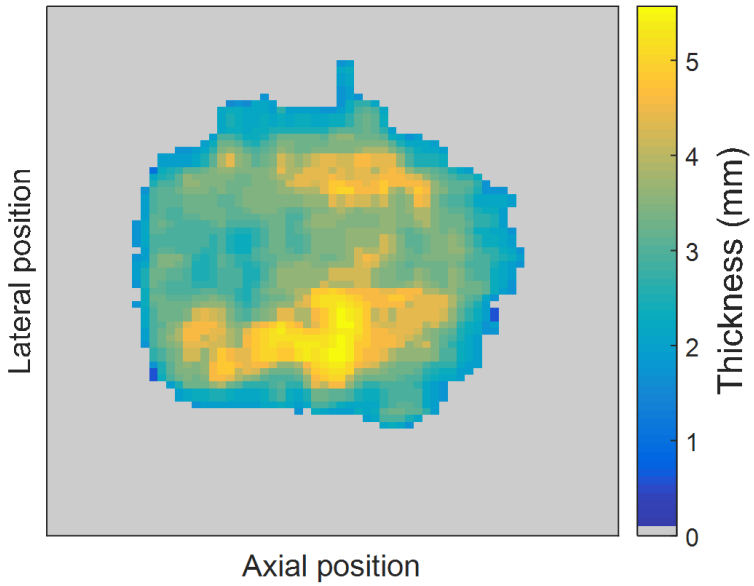

Figure 5.32: Calculated thickness map of the real corrosion defect. The calculated lateral and axial sizes are both 19.1 mm.

for one are within ±3 mm of the actual dimensions.

Finally, the impact of not knowing whether the defect is inner or outer wall was investigated. The method produces results for both cases, and the general effect is that the outer wall results are several millimetres higher than the inner wall results. This is because, due to lesser magnification, a defect on the outer wall must be larger than one on the inner wall to produce the same size image on the detector. Examples of potential outer wall defect dimensions for the smaller diameter corrosion defects are shown in Figure 5.35. As expected outer wall results are higher than those for the inner wall. In this case, since lateral and axial dimensions were underestimated in the inner wall case they are actually more accurate in the outer wall case. However, the potential thickness is significantly greater in the outer wall case. This demonstrates that it is very helpful, but not crucial, to know whether defects are most likely inner or outer wall.

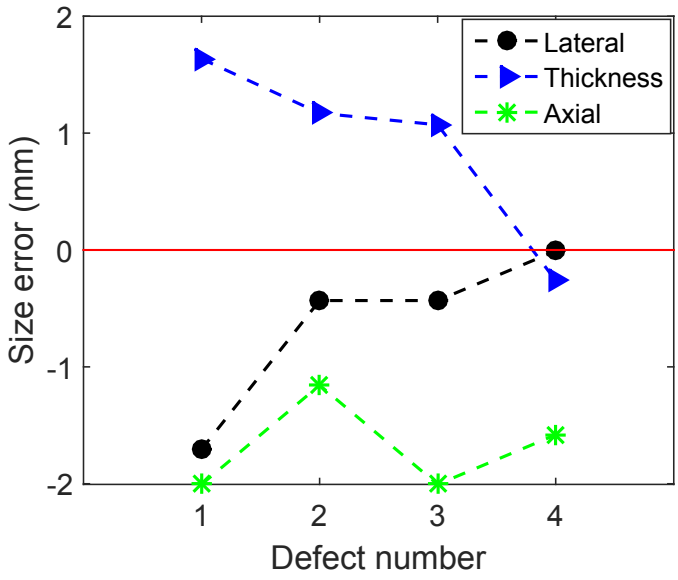

Figure 5.33: Error in calculated defect dimensions for real corrosion defects. Defect number 1 is the original defect, shown in Fig 5.31, while numbers 2, 3 and 4 have the same lateral and axial size but increased thickness by factors of 2, 3 and 4 respectively. Error was taken as (calculated - actual) size.

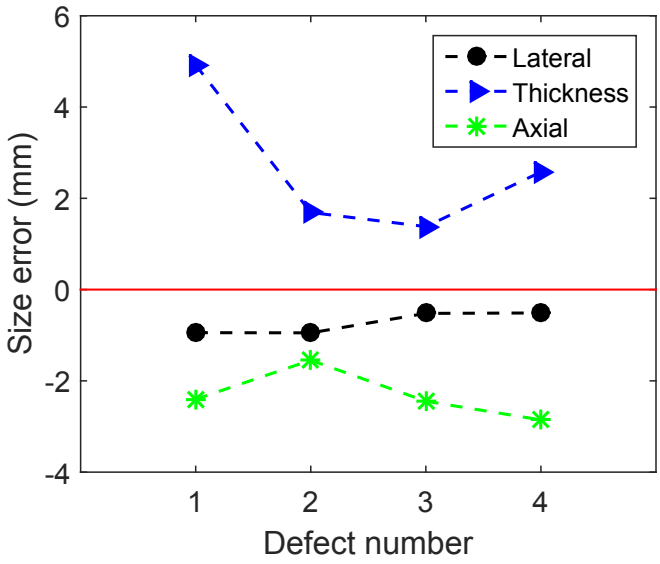

Figure 5.34: Error in calculated defect dimensions for larger diameter real corrosion defects. Defect number 1 has been scaled to have lateral and axial sizes of 33.2 mm and 33.8 mm respectively, while numbers 2, 3 and 4 have the same lateral and axial size but increased thickness by factors of 2, 3 and 4. Error was taken as (calculated - actual) size.

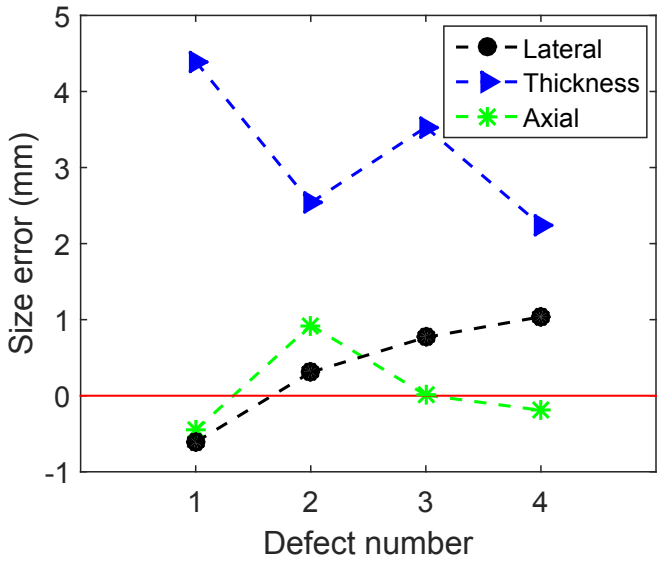

Figure 5.35: Results for the same defects as shown in Fig 5.33 but for the case that they are identified as outer wall defects by the model.

5.4 Discussion

Characterisation of pipeline defects with radiography traditionally relies on calibration objects such as a step wedge being included in the setup. However, including these objects in the correct location can be complex and time consuming, with the potential for significant error if not correctly placed. In addition, the measurement of wall thickness from intensity, even when calibrated with a step wedge, is an estimate and susceptible to errors, for example due to high levels of scattering [100]. This chapter has presented an alternative method of defect characterisation for which no changes to the setup or calibration items are needed. Instead, characterisation makes use of three images of the defect taken at different angles, combined with knowledge of the setup geometry. The model is resilient to minor errors in the input parameters, such as the angle between images or pipe position, and is able to check for and correct possible errors. The method is aimed at use in situations where access is difficult such as in subsea pipeline inspections. In these cases including calibration objects may be particularly difficult, and will add an additional layer of complexity to the inspection.

The defect characterisation method has been tested on simulated and experimental flat bottomed hole defects and on simulated corrosion patch defects. Results show an excellent lateral and axial sizing ability. The largest errors were seen for lateral sizing of the experimental 20% wall thickness holes, which were consistently underestimated by about 3 mm. The consistent underestimation could be due to the feature extraction method not identifying all defect pixels; there was no set of background images available for feature extraction in the experimental data, making errors more likely.

Defect thickness is more difficult to calculate and results show greater error, as expected. However, in most cases, particularly for smaller defects, the method still gave results to within ± 3 mm of the actual thickness. A key consideration on the defect thickness calculation is that, in cases where it is not accurate, it is an overestimate. The thickness was underestimated in only two of all the defects tested, and by less than 0.5 mm in these cases. Therefore the thickness result could be taken as an upper bound on the defect thickness rather than an actual defect thickness. While an actual thickness would be ideal, an upper bound on thickness would still prove useful in determining the severity of the defect.

The angle of separation between images was found to have a significant impact on the accuracy of thickness calculations. The most accurate results were found for sets of images with one at 0° and two others at the maximum angles possible while keeping the defect in view. These three images provide the most useful data for defect characterisation. Images at smaller angles of separation could be included, in addition to the ideal three images, however they do not add significant information and results are not much improved, if at all. The added time and expense of taking more images would far exceed any minor improvements in accuracy. Therefore the ideal three images should be used wherever possible. In cases where large angles of rotation are not available the method will still produce accurate axial and lateral sizing and place a limit on defect thickness.

So far the method has been tested on good quality, low noise data. The feature extraction method depends on there being significant differences between intensity through a defect and background intensity and could have trouble identifying a defect if the difference is masked by noise. However, the focus of this work has been on developing the ray tracing and application of constraints parts of the method. While feature extraction is required in order to get the pixel positions of the defect in each image, this could be performed manually if needed. Therefore, while the method may not be able to be fully automatic for low quality images it would still be applicable. Alternatively more advanced methods of feature extraction could be used.

5.5 Summary

This chapter has presented a pipeline defect characterisation method based on radiographic images taken at different angles around the pipe. The method consists of three main parts; feature extraction, ray tracing and application of constraints. In feature extraction a set of background images is used to identify defects in the images of interest. Ray tracing is then used to calculate the potential positions and sizes of the defect. By using ray tracing on sets of images of the same defect but at different angles, the range of defect size and position can be reduced. Constraints on pipe wall location, defect intensity-distance relationship and the effective attenuation coefficient are then applied. These constraints act to further narrow down the potential defect thickness. The method has been tested

on simulated and experimental inner wall flat bottomed hole defects and simulated inner wall corrosion patch defects. Results show good agreement, within ±3 mm, for lateral and axial dimensions, and in most cases similar accuracy in thickness calculations, but with some overestimation. Further work should address a realistic inspection context, for which the method could be tuned for maximum performance. It should also take into account the availability of the radiographs and setup geometry data required by the method and the performance targets of the inspection. The key point of the method is that it does not require additional objects such as a step wedge to be placed in the exposure setup. It is aimed at use in situations where access is difficult such as in subsea pipeline inspections.

6 Conclusion

6.1 Summary

In this thesis I have described three key aspects of my doctorate work: development of a radiographic simulation model, investigation of the accuracy of simulation models for subsea inspections and development of a method of pipeline defect characterisation. I began the thesis by explaining the motivation behind this research, which centres on the need in the oil and gas industry for accurate, reliable detection and characterisation of subsea pipeline defects. In Chapter 2 I covered useful background theory for the project, ranging from photon interactions in matter to a comparison of different detector types. I described the main project work in roughly chronological order in Chapters 3, 4 and 5. Each of these chapters is a self-contained segment of my work, revolving around investigating and improving external radiographic inspection of subsea pipelines.

In the first year of the project I developed a radiographic simulation model, PRIM. In Chapter 3 I detailed the method of radiographic simulation used in PRIM, which combines an analytical ray tracing calculation with a Monte Carlo scattering simulation. I also demonstrated a validation of PRIM results through comparison with commercial models CIVA and aRTist. The key appeal of PRIM is that it is optimised for pipeline imaging and is thus, for pipeline setups, usually faster than more generalised commercial models. It has proved to be useful as a simple, easily modifiable simulation model, able to provide data for development and testing in other areas of my project.

In Chapter 4 I described an experimental validation of aRTist for high energy underwater radiography. The aim was to compare simulated and experimental data and to develop a set of simulation parameters for matching simulated to experimental images. However, I found a significant unexpected difference between simulated and experimental data, particularly in

the image contrast. After some investigation I identified a potential cause of the differences: scattering from additional objects in the exposure bay which were not included in the simulation. Although some additional scattering in the experiment is to be expected, the difference found is surprisingly large, even in the absence of water around the pipe. This finding could have significant implications for the ability of simulations to predict experimental data in some circumstances. In particular it implies that it will be very difficult to completely match simulated to experimental data, as including all possible scattering objects in the model would be very complex. Improvement in simulation potential could be made by calibrating the model with experimental subsea data, which should help account for additional scattering. It may also be possible to reduce the impact of scattering by using filters and shielding in the experimental setup. However there would still be significant uncertainties, for example due to lack of knowledge of which objects may be adjacent to any given subsea setup. This means there would still be uncertainty in the ability of the simulation to accurately produce realistic intensity and contrast.

Finally, in Chapter 5 I detailed the development of a pipeline defect characterisation method. The aim was to develop an alternative to traditional methods of radiographic defect characterisation, which often rely on calibration objects placed in the setup. My method uses images taken at different angles around the pipe instead of calibration objects, with a stereographic type approach to combine the data from each image. The method is aimed at use in situations where access to the pipe is difficult, as in subsea inspections. I have tested it on a range of simulated and experimental data and found it to give good agreement of lateral and axial defect size, and reasonable estimates of defect thickness in most cases. The method has the potential to be fully automatic, requiring input of a set of images and setup geometry and from this calculating defect size without further manual intervention.

6.2 Future Work

My project has been a broad investigation of subsea pipeline radiography. As such, there are a couple of ways my work could be extended. One key research area is investigation of peripheral scattering in radiography.

In Chapter 4 I described initial results showing that peripheral scattering has a surprisingly large impact on the final radiograph. A first step in any further work would be to experimentally verify this finding. An example experiment would firstly take a set of radiographs in a fairly clear exposure bay, with few unnecessary scattering objects present. A second set of radiographs would then be taken, using the same setup parameters but with an additional – preferably highly scattering – object placed near the setup. Comparison of the two sets of radiographs should reveal the impact of peripheral scattering. When running the experiments it would also be useful to measure radiation around the exposure bay, in various locations. This could confirm the amount of radiation around scattering objects, and could be used to provide additional measurements for comparison with simulation.

As I explained in Chapter 4, it is likely that peripheral scattering varies significantly with the source energy spectrum. It would be interesting to investigate this variance; for example, through repeating the peripheral scattering experiment for a range of different source energies. This work would give insight into high energy radiography in general rather than just subsea. It would be particularly useful if an optimum source energy could be identified, where peripheral scattering has least impact.

Following on from experimental verification of peripheral scattering, the next stage would be fully validating radiographic simulation models, like aRTist, for high energy, underwater imaging. The method of validation could be a comparison between experimental and simulated results as described in my thesis, but with shielding to reduce experimental peripheral scattering. Alternatively the full exposure bay, including all objects, could be modelled in the simulation. Once the simulation model is validated, an analysis would be needed of how accurately the simulation could predict experimental subsea images, accounting for peripheral scattering. Differences between simulation and experiment may persevere, due to (for example) unknown location and impact of objects, such as the sea floor in some setups. At this point, calibration of simulated images with experimental data could be used to improve accuracy. However, the validity of this technique and potential improvements would need thorough examination. The final aim in this stream of work would be the ability to accurately simulate and compare different subsea radiographic setups, quantifying the impact of water and the limiting factors on image quality.

The other main area for further research is continuing my work on defect characterisation. In this thesis I have contributed the foundation for a new defect characterisation method. But significantly more testing and development would be needed before the method could be used within industry. On the testing side, the method needs to be run on a much wider range of data to verify where it works best, along with errors and limitations. In terms of development, some aspects of the method, particularly the feature extraction method, were not the focus of my work and hence could be improved. The idea that the method could be fully automated is also an interesting area to explore. For an automated method, testing and validation would be very important to ensure errors are picked up by the model alone, without a human operator.

The next stage in development would involve working with industry to deploy the method in practice. Methods of subsea pipeline radiography use systems which can rotate around the pipe as well as move along it – so obtaining three images of a defect at different angles should be possible with current equipment. However, it is likely that the pipeline imaging would be constrained by cost, meaning taking any additional images would need a strong motivation. A cost-benefit analysis of the defect characterisation method may demonstrate the benefits and permit quantitative comparisons against other methods, such as including a step wedge in the setup. In terms of use of the software, a user interface would need to be developed. However, as the method is mostly self-contained and just requires the input of relevant images and setup parameters, this could be kept fairly simple.

In summary, in this section I have described the two main areas of work following on from my project. The first, studying peripheral scattering and validating a simulation, is an academic topic which should prove useful for high energy radiography in general. The second, further development of my defect characterisation method, is more about software development and technology transfer to industry, but has the potential to greatly improve defect characterisation in subsea pipeline imaging.

6.3 List of Publications

- M. I. Haith, U. Ewert, S. Hohendorf, C. Bellon, A. Deresch, P. Huthwaite, M. J. Lowe, and U. Zscherpel, "Radiographic modelling for NDE of subsea pipelines," *NDT & E International*, vol. 86, pp. 113–122, 2017

- M. I. Haith, P. Huthwaite, and M. J. Lowe, "Defect characterisation from limited view pipeline radiography," *NDT & E International*, vol. 86, pp. 186–198, 2017

- M. I. Haith, U. Ewert, S. Hohendorf, C. Bellon, A. Deresch, P. Huthwaite, M. J. S. Lowe, and U. Zscherpel, "Modelling based radiography for NDE of subsea pipelines," in *review of Progress in Quantitative Nondestructive Evaluation.* eds. D. O. Thompson and D. E. Chimenti (American Institute of Physics 1706, Melville, NY), 110004 (2016).

- U. Ewert, M. Tschaikner, S. Hohendorf, C. Bellon, M. I. Haith, P. Huthwaite, and M. J. S. Lowe, "Corrosion monitoring with tangential radiography and limited view computed tomography," in *review of Progress in Quantitative Nondestructive Evaluation.* eds. D. O. Thompson and D. E. Chimenti (American Institute of Physics 1706, Melville, NY), 110003 (2016).

Bibliography

[1] R. Halmshaw, *Non-Destructive Testing*. Arnold, 1991. eds. R.W.K Honeycombe and P. Hancock.

[2] Y. Bai and Q. Bai, *Subsea Pipeline Integrity and Risk Management*. Gulf Professional Publishing, 2014.

[3] EN 16407-1 : 2014, "Non-destructive testing - Radiographic inspection of corrosion and deposits in pipes by X- and gamma rays - Part 1: Tangential radiographic inspection"

[4] EN 16407-2 : 2014, "Non-destructive testing - Radiographic inspection of corrosion and deposits in pipes by X- and gamma rays - Part 2: Double wall radiographic inspection"

[5] Royal Commission for the Exhibition of 1851, www.royalcommission1851.org.

[6] Bundesanstalt fur Materialforschung und -prufung (BAM), www.bam.de.

[7] M. I. Haith, U. Ewert, S. Hohendorf, C. Bellon, A. Deresch, P. Huthwaite, M. J. S. Lowe, and U. Zscherpel, "Modelling based radiography for NDE of subsea pipelines," in *review of Progress in Quantitative Nondestructive Evaluation*. eds. D. O. Thompson and D. E. Chimenti (American Institute of Physics 1706, Melville, NY), 110004 (2016).

[8] U. Ewert, M. Tschaikner, S. Hohendorf, C. Bellon, M. I. Haith, P. Huthwaite, and M. J. S. Lowe, "Corrosion monitoring with tangential radiography and limited view computed tomography," in *review of Progress in Quantitative Nondestructive Evaluation*. eds. D. O. Thompson and D. E. Chimenti (American Institute of Physics 1706, Melville, NY), 110003 (2016).

[9] M. I. Haith, U. Ewert, S. Hohendorf, C. Bellon, A. Deresch, P. Huthwaite, M. J. Lowe, and U. Zscherpel, "Radiographic modelling for NDE of subsea pipelines," *NDT & E International*, vol. 86, pp. 113–122, 2017.

[10] M. I. Haith, P. Huthwaite, and M. J. Lowe, "Defect characterisation from limited view pipeline radiography," *NDT & E International*, vol. 86, pp. 186–198, 2017.

[11] R. Halmshaw, *Industrial Radiography*. Agfa-Gevaert, 1991.

[12] M. Berger, J. Hubbell, S. Seltzer, J. Chang, J. Coursey, R. Sukumar, D. Zucker, and K. Olsen, "XCOM: Photon Cross Sections Database," 1998.

[13] F. Inanc, "Verification of deterministic scattering computations and some observations," in *Review of Progress in Quantitative Nondestructive Evaluation*, pp. 639–646, Springer, 1999.

[14] N. Freud, P. Duvauchelle, S. Pistrui-Maximean, J.-M. Létang, and D. Babot, "Deterministic simulation of first-order scattering in virtual x-ray imaging," *Nuclear Instruments and Methods in Physics Research Section B: Beam Interactions with Materials and Atoms*, vol. 222, no. 1, pp. 285–300, 2004.

[15] F. Inanc, "Scattering and its role in radiography simulations," *NDT & E International*, vol. 35, no. 8, pp. 581–593, 2002.

[16] www.nde-ed.org/EducationResources/CommunityCollege/Radiography/EquipmentMaterials/isotopesources.htm Accessed on 26/05/2016

[17] JME Betatrons, www.jme.co.uk, Accessed on 26/05/2016

[18] GE Inspection Technologies, Industrial Radiography - Image forming techniques, www.gemeasurement.com, Accessed on 26/05/2016

[19] www.nde-ed.org/EducationResources/CommunityCollege/Radiography/EquipmentMaterials/radiographicfilm.htm, Accessed on 28/06/2016

[20] http://pocketdentistry.com/4-digital-imaging, Accessed on 28/06/2016

[21] M. Hoheisel, M. Arques, J. Chabbal, C. Chaussat, T. Ducourant, G. Hahm, H. Horbaschek, R. Schulz, and M. Spahn, "Amorphous silicon x-ray detectors," *Journal of non-crystalline solids*, vol. 227, pp. 1300–1305, 1998.

[22] A. R. Cowen, S. M. Kengyelics, and A. G. Davies, "Solid-state, flat-panel, digital radiography detectors and their physical imaging characteristics," *Clinical Radiology*, vol. 63, no. 5, pp. 487–498, 2008.

[23] L. Lanca and A. Silva, "Digital radiography detectors a technical overview: Part 1," *Radiography*, vol. 15, no. 1, pp. 58–62, 2009.

[24] L. Lanca and A. Silva, "Digital radiography detectors a technical overview: Part 2," *Radiography*, vol. 15, no. 2, pp. 134–138, 2009.

[25] C. M. Shetty, A. Barthur, A. Kambadakone, and N. Narayanan, "Computed radiography image artifacts revisited," *American Journal of Roentgenology*, vol. 196, no. 1, pp. W37–W47, 2011.

[26] V. Nagarkar, J. Gordon, T. Gupta, S. Vasile, P. Gothoskar, and G. Entine, "CCD-based high resolution digital radiography system for nondestructive evaluation," in *Nuclear Science Symposium*, vol. 1, pp. 246–250, IEEE, 1996.

[27] U. Ewert, U. Zscherpel, and K. Bavendiek, "Replacement of film radiography by digital techniques and enhancement of image quality," in *Annual conference of Indian NDT society*, (Kalkutta), 2005.

[28] K. Bavendiek, U. Heike, W. Meade, U. Zscherpel, and U. Ewert, "New digital radiography procedure exceeds film sensitivity considerably in aerospace applications," *ECNDT, Berlin*, 2006.

[29] T. Kersting, N. Schnartz, L. Oesterlein, and A. Liessem, "High end inspection by filmless radiography on LSAW large diameter pipes," *NDT & E International*, vol. 43, no. 3, pp. 206–209, 2010.

[30] B. Ghose, V. Mall, B. Dhere, and D. Kankane, "Digital radiography of solid rocket propellant with 4-Mev linac x-ray using computer radiography (CR) system," in *National Seminar & Exhibition on Non-Destructive Evaluation*, 2011.

[31] E. Deprins, "Computed radiography in NDT applications," *Insight-Non-Destructive Testing and Condition Monitoring*, vol. 46, no. 10, pp. 590–593, 2004.

[32] U. Ewert, U. Zscherpel, and K. Bavendiek, "Strategies for film replacement in radiography - films and digital detectors in comparison," in *17th World Conference on Nondestructive Testing,*, (Shanghai, China), 2008.

[33] I. Sikakana and M. Thebe, "Evaluation of an x-ray digital radiography system," in *18th World Conference on Nondestructive Testing*, (Durban, South Africa), 2012.

[34] U. Zscherpel, U. Ewert, and M. Jechow, "Concepts for evaluation of image quality in digital radiology," in *Review of Progress in Quantitative Nondestructive Evaluation*, vol. 1430, (Burlington, VT), pp. 589–596, AIP, 2011.

[35] U. Zscherpel, U. Ewert, and C. Bellon, "Strategies for optimum calibration of detector arrays in digital industrial radiology," in *Review of Progress in Quantitative NDE*, (Baltimore), 2013.

[36] Oceaneering Subsea Digital Radiography Tool, www.youtube.com/oceaneering/videos.

[37] R. Halmshaw and T. Kowol, "Image quality indicators in industrial radiography," *IE-NDT LTD technical materials*, 2001.

[38] ASTM E2002 - 15 (Reapproved 2009, Revised 2015 - to be published), "Standard Practice for Determining Total Image Unsharpness and Basic Spatial Resolution in Radiography and Radioscopy"

[39] ASTM E2446 - 05 (Reapproved 2010, Revised 2015 - to be published), "Standard Practice for Manufacturing Characterization of Computed Radiography Systems"

[40] U. Ewert, U. Zscherpel, and K. Bavendiek, "Strategies for film replacement in radiography - a comparative study," in *PANNDT*, (Buenos Aires, Argentina), Oct 22-26 2007.

[41] A. Kak and M. Slaney, *Principles of Computerized Tomographic Imaging*. IEEE Press, 1988.

[42] L. Feldkamp, L. Davis, and J. Kress, "Practical cone-beam algorithm," *JOSA A*, vol. 1, no. 6, pp. 612–619, 1984.

[43] P.-E. Danielsson, "3D cone-beam tomography for non-destructive testing," in *IAPR Workshop on Machine Vision Applications*, (Kawasaki), 1994.

[44] A. Lange, A. Kupsch, M. Hentschel, I. Manke, N. Kardjilov, T. Arlt, and R. Grothausmann, "Reconstruction of limited computed tomography data of fuel cell components using direct iterative reconstruction of computed tomography trajectories," *Journal of Power Sources*, vol. 196, no. 12, pp. 5293–5298, 2011.

[45] R. Gordon, R. Bender, and G. T. Herman, "Algebraic reconstruction techniques (ART) for three-dimensional electron microscopy and X-ray photography," *Journal of theoretical Biology*, vol. 29, no. 3, pp. 471–481, 1970.

[46] A. Andersen and A. Kak, "Simultaneous algebraic reconstruction technique (SART): a superior implementation of the ART algorithm," *Ultrasonic imaging*, vol. 6, no. 1, pp. 81–94, 1984.

[47] K. Hanson, "Bayesian and related methods in image reconstruction from incomplete data," *Image Recovery: Theory and Application*, pp. 79–125, 1987.

[48] J. Tang, B. E. Nett, and G.-H. Chen, "Performance comparison between total variation (TV)-based compressed sensing and statistical iterative reconstruction algorithms," *Physics in medicine and biology*, vol. 54, no. 19, p. 5781, 2009.

[49] M. Li, H. Yang, and H. Kudo, "An accurate iterative reconstruction algorithm for sparse objects: application to 3D blood vessel reconstruction from a limited number of projections," *Physics in medicine and biology*, vol. 47, no. 15, p. 2599, 2002.

[50] E. Sidky and X. Pan, "Image reconstruction in circular cone-beam computed tomography by constrained, total-variation minimization," *Physics in medicine and biology*, vol. 53, no. 17, p. 4777, 2008.

[51] X. Jia, Y. Lou, R. Li, W. Y. Song, and S. B. Jiang, "GPU-based fast cone beam CT reconstruction from undersampled and noisy projection data via total variation," *Medical physics*, vol. 37, p. 1757, 2010.

[52] S. Osher, M. Burger, D. Goldfarb, J. Xu, and W. Yin, "An iterative regularization method for total variation-based image restoration," *Multiscale Modeling & Simulation*, vol. 4, no. 2, pp. 460–489, 2005.

[53] J. Velikina, S. Leng, and G.-H. Chen, "Limited view angle tomographic image reconstruction via total variation minimization," in *Medical Imaging*, pp. 651020–651020–12, International Society for Optics and Photonics, 2007.

[54] Y. Liu, J. Ma, Y. Fan, and Z. Liang, "Adaptive-weighted total variation minimization for sparse data toward low-dose x-ray computed tomography image reconstruction," *Physics in medicine and biology*, vol. 57, no. 23, p. 7923, 2012.

[55] G.-H. Chen, J. Tang, and S. Leng, "Prior image constrained compressed sensing (PICCS): a method to accurately reconstruct dynamic CT images from highly undersampled projection data sets," *Medical physics*, vol. 35, p. 660, 2008.

[56] V. Singh, L. Mukherjee, P. Dinu, J. Xu, and K. Hoffmann, "Limited view CT reconstruction and segmentation via constrained metric labeling," *Computer Vision and Image Understanding*, vol. 112, no. 1, pp. 67–80, 2008.

[57] H. Machida, T. Yuhara, T. Mori, E. Ueno, Y. Moribe, and J. M. Sabol, "Optimizing parameters for flat-panel detector digital tomosynthesis," *Radiographics*, vol. 30, no. 2, pp. 549–562, 2010.

[58] Y. Lu, H.-P. Chan, J. Wei, and L. M. Hadjiiski, "A diffusion-based truncated projection artifact reduction method for iterative digital breast tomosynthesis reconstruction," *Physics in Medicine and Biology*, vol. 58, no. 3, p. 569, 2013.

[59] F. Jian, L. Hongnian, L. Bing, Z. Lei, and S. Jingjing, "X-CT imaging method for large objects using double offset scan mode," *Nuclear Instruments and Methods in Physics Research Section A: Accelerators, Spectrometers, Detectors and Associated Equipment*, vol. 575, no. 3, pp. 519–523, 2007.

[60] I. Sechopoulos, "A review of breast tomosynthesis. Part I the image acquisition process," *Medical Physics*, vol. 40, no. 1, 2013.

[61] T. Nielsen, S. Hitziger, M. Grass, and A. Iske, "Filter calculation for x-ray tomosynthesis reconstruction," *Physics in Medicine and Biology*, vol. 57, no. 12, p. 3915, 2012.

[62] I. Sechopoulos, "A review of breast tomosynthesis. Part II image reconstruction, processing and analysis, and advanced applications," *Medical Physics*, vol. 40, no. 1, 2013.

[63] R. Fernandez, A. Schumm, J. Tabary, and P. Hugonnard, "Simulation studies of radiographic inspections with CIVA," *17th WCNDT, Shanghai*, 2008.

[64] A. Schumm, O. Bremnes, and B. Chassignole, "Numerical simulation of radiographic inspections: fast and realistic results even for thick components," in *Proceedings of the 16th world conference of Non-Destructive Testing, Montreal*, 2004.

[65] J. Tabary, P. Hugonnard, and F. Mathy, "SINDBAD: a realistic multi-purpose and scalable X-ray simulation tool for NDT applications," in *Int. Symp. on DIR and CT, Lyon*, 2007.

[66] J. Zou, Z. Hu, J. Gui, J. Rong, Y. Li, and H. Zheng, "Geant4-based Monte Carlo simulator for fan-and cone-beam x-ray CT," in *Bioinformatics and Biomedical Engineering (iCBBE), 2010 4th International Conference on*, pp. 1–4, IEEE, 2010.

[67] J. Tabary, R. Guillemaud, F. Mathy, A. Glire, and P. Hugonnard, "Combination of high resolution analytically computed uncollided flux images with low resolution Monte Carlo computed scattered flux images," *Nuclear Science, IEEE Transactions on*, vol. 51, no. 1, pp. 212–217, 2004.

[68] M. R. Ay, P. Ghafrain, and H. Zaidi, "A hybrid approach for fast simulation of x-ray computed tomography," in *Nuclear Science Symposium Conference Record, 2007. NSS'07. IEEE*, vol. 4, pp. 3155–3160, IEEE, 2007.

[69] CIVA, www-civa.cea.fr.

[70] R. Fernandez, L. Clement, D. Tisseur, R. Guillamet, M. Costin, C. Vienne, and V. Colombie, "RT Modelling for NDT Recent and Future Developments in the CIVA RT/CT Module," in *Proc. of 19th World Conference on Non-Destructive Testing*, (Munich, Germany), 2016.

[71] aRTist, www.artist.bam.de.

[72] CEA LIST, www-list.cea.fr/en.

[73] R. Siddon, "Fast calculation of the exact radiological path for a three-dimensional CT array," *Medical Physics*, vol. 12, no. 2, p. 252, 1985.

[74] F. Jacobs, E. Sundermann, B. De Sutter, M. Christiaens, and I. Lemahieu, "A fast algorithm to calculate the exact radiological path through a pixel or voxel space," *Journal of computing and information technology*, vol. 6, no. 1, pp. 89–94, 1998.

[75] https://www.nde-ed.org/EducationResources/CommunityCollege/RadiationSafety/theory/activity.htm Accessed on 29/01/2017

[76] F. Arqueros and G. Montesinos, "A simple algorithm for the transport of gamma rays in a medium," *American Journal of Physics*, vol. 71, p. 38, 2003.

[77] F. Salvat, J. M. Fernndez-Varea, and J. Sempau, "PENELOPE-2006: A code system for Monte Carlo simulation of electron and photon transport," in *Workshop Proceedings*, vol. 4, (Barcelona, Spain), p. 7, 2006.

[78] L. Wang, S. L. Jacques, and L. Zheng, "MCML Monte Carlo modeling of light transport in multi-layered tissues," *Computer methods and programs in biomedicine*, vol. 47, no. 2, pp. 131–146, 1995.

[79] D. Fulea, C. Cosma, and I. Pop, "Monte Carlo method for radiological X-ray examinations," *Romanian Journal in Physics*, vol. 54, no. 7-8, pp. 629–639, 2009.

[80] G.-R. Jaenisch, C. Bellon, U. Samadurau, M. Zhukovskiy, and S. Podoliako, "McRay - a Monte Carlo model coupled to CAD for radiation techniques," in *European Conf. NDT, Tu*, vol. 4, 2006.

[81] W. J. Veigele, P. T. Tracy, and E. M. Henry, "Compton effect and electron binding," *American Journal of Physics*, vol. 34, no. 12, pp. 1116–1121, 1966.

[82] H. Hirayama, Y. Namito, W. R. Nelson, A. F. Bielajew, S. J. Wilderman, and U. Michigan, "The EGS5 code system," tech. rep., United States. Department of Energy, 2005.

[83] M. Matsumoto and T. Nishimura, "Mersenne twister: a 623-dimensionally equidistributed uniform pseudo-random number generator," *ACM Transactions on Modeling and Computer Simulation (TOMACS)*, vol. 8, no. 1, pp. 3–30, 1998.

[84] Mersenne twister algorithm, www.umiacs.umd.edu/yangcj/mtrnd.html, Accessed 19/09/2013.

[85] E. M. Souza, S. C. A. Correa, A. X. Silva, R. T. Lopes, and D. F. Oliveira, "Methodology for digital radiography simulation using the Monte Carlo code MCNPX for industrial applications," *Applied Radiation and Isotopes*, vol. 66, no. 5, pp. 587–592, 2008.

[86] E. M. Souza, S. C. A. Correa, A. X. Silva, and R. T. Lopes, "Analyze of several ways to minimize the scatter contribution in radiographic digital images of offshore pipelines," in *Proc. of International Nuclear Atlantic Conference*, (Brazil), 2011.

[87] E. M. de Souza, S. C. A. Correa, J. P. R. Junior, A. X. Silva, and R. T. Lopes, "Analysis of the influence of liquid and of external coating material on the quality of the radiographic image of offshore pipes using computational modeling," in *Materials Science Forum*, vol. 775, pp. 197–202, Trans Tech Publ, 2014.

[88] S. C. A. Correa, E. M. Souza, D. F. Oliveira, A. X. Silva, R. T. Lopes, C. Marinho, and C. S. Camerini, "Assessment of weld thickness loss in offshore pipelines using computed radiography and computational modeling," *Applied Radiation and Isotopes*, vol. 67, no. 10, pp. 1824–1828, 2009.

[89] D. B. Pelowitz, "MCNPXTM users manual," *Los Alamos National Laboratory, Los Alamos*, 2005.

[90] MCNP, www.mcnp.lanl.gov.

[91] D. Tisseur, B. Rattoni, C. Vienne, R. Guillamet, G. Cattiaux, and T. Sollier, "First Validation of CIVA RT Module with a Linear Accelerator in a Nuclear Context," in *Proc. of 19th World Conference on Non-Destructive Testing*, (Munich, Germany), 2016.

[92] S. Kolkoori, G.-R. Jaenisch, and A. Deresch, "Influence of scattered radiation on the efficiency of dual high-energy x-ray imaging for material characterization," in *Proc. of 19th World Conference on Non-Destructive Testing*, (Munich, Germany), 2016.

[93] JME Portable 7.5 MeV X-ray Betatron for Radiographic Non-Destructive Testing, User Manual, Issue 1, 2006.

[94] XRD 1621 Detector Series, Basic Specifications and Potential Applications of Digital Flat Panel Detectors, www.perkinelmer.com

[95] C. Bellon, A. Deresch, C. Gollwitzer, and G.-R. Jaenisch, "Radiographic Simulator aRTist: Version 2," in *Proc. of 18th World Conference on Nondestructive Testing*, (Durban, South Africa), 2012. www.ndt.net/article/wcndt2012/papers/333_wcndtfinal00333.pdf.

[96] G. R. Jaenisch, A. Deresch, C. Bellon, U. Ewert, and W. Przybilla, "Measurement and modeling of scatter ratios at high energies," in *review of Progress in Quantitative Nondestructive Evaluation.* eds. D. O. Thompson and D. E. Chimenti (American Institute of Physics 1335, Melville, NY) **30**, 517-524 (2011).

[97] A. Deresch, M. Jechow, and C. Gollwitzer, "Spectral characterization of storage phosphor imaging plates," in *review of Progress in*

Quantitative Nondestructive Evaluation. eds. D. O. Thompson and D. E. Chimenti (American Institute of Physics 1581, Melville, NY) **33**, 1786-1792 (2014).

[98] A. Deresch, G. R. Jaenisch, C. Bellon, and A. Warrikhoff, "Simulation and Experimental Verification of X-Ray Spectra," in *review of Progress in Quantitative Nondestructive Evaluation*. eds. D. O. Thompson and D. E. Chimenti (American Institute of Physics 1211, Melville, NY) **29**, 535-540 (2010).

[99] U. Zscherpel, K. Osterloh, U. Ewert, and B. Berlin, "Unsharpness characteristics of digital detectors for industrial radiographic imaging," *Journal of Nondestructive Testing*, vol. 9, no. 5, pp. 1–8, 2004.

[100] S. Burch, "Recommended practice for the in-service inspection of wall loss in pipes by computed radiography," *HOIS report RP1 Issue 2*, 2012.

[101] E. R. Doering, *Three-dimensional flaw reconstruction using a real-time X-ray imaging system*. PhD thesis, Iowa State University, 1992.

[102] E. Lindgren, "Detection, 3-D positioning, and sizing of small pore defects using digital radiography and tracking," *EURASIP Journal on Advances in Signal Processing*, vol. 2014, no. 1, pp. 1–17, 2014.

[103] E. Lindgren, "Detection and 3-D positioning of small defects using 3-D point reconstruction, tracking, and the radiographic magnification technique," *NDT & E International*, vol. 76, pp. 1–8, 2015.

[104] E. Lindgren, "Detectability limitations with 3-D point reconstruction algorithms using digital radiography," in *review of Progress in Quantitative Nondestructive Evaluation*. eds. D. O. Thompson and D. E. Chimenti (American Institute of Physics 1650, Melville, NY) **34**, 599-604 (2015).

[105] M. Carrasco and D. Mery, "Automatic multiple view inspection using geometrical tracking and feature analysis in aluminum wheels," *Machine Vision and Applications*, vol. 22, no. 1, pp. 157–170, 2011.

[106] D. Mery, "Inspection of complex objects using multiple-x-ray views," *IEEE/ASME Transactions on Mechatronics*, vol. 20, no. 1, pp. 338–347, 2015.

[107] J. Amanatides, A. Woo, *et al.*, "A fast voxel traversal algorithm for ray tracing," in *Eurographics*, vol. 87, p. 10, 1987.